The Drift Tube Spectrometer for the Measurement of the Muon Flux and Spectrum Emerging from a Proton Beam Dump at the SPS for the SHiP Experiment

Das Drifttröhren-Spektrometer für die Messung des Myonflusses- und Spektrums aus einem Protonen Beam Dump am SPS für das SHiP Experiment

Dissertation
zur Erlangung des Doktorgrades
an der Fakultät für Mathematik, Informatik und Naturwissenschaften
Fachbereich Physik
an der Universität Hamburg

vorgelegt von
Stefan Bieschke

Hamburg
2020

Gutachter/innen der Dissertation:	Prof. Dr. Caren Hagner Dr. Daniel Bick
Zusammensetzung der Prüfungskommission:	Prof. Dr. Peter Schmelcher Prof. Dr. Caren Hagner Prof. Dr. Sven-Olaf Moch Prof. Dr. Johannes Haller Dr. Daniel Bick
Vorsitzende/r der Prüfungskommission:	Prof. Dr. Peter Schmelcher
Datum der Disputation:	09.12.2020
Vorsitzender Fach-Promotionsausschuss PHYSIK:	Prof. Dr. Wolfgang Hansen
Leiter des Fachbereichs PHYSIK:	Prof. Dr. Günter H. W. Sigl
Dekan der Fakultät MIN:	Prof. Dr. Heinrich Graener

Abstract

The SHiP experiment, which stands for the ***S**earch for **Hi**dden **P**articles*, is a proposed beam dump experiment dedicated to the search for yet undetected particles, utilizing the 400 GeV proton beam of CERN's Super Proton Synchrotron (SPS). SHiP will examine a region of the hidden sector, where particles are light enough to be accessible to existing accelerators but very weakly interacting. Due to their low interaction probability, these new particles might have evaded their detection due to too small detectors or too small beam intensity. The discovery of these particles requires a low and well known background. Being a beam dump experiment however, a huge flux of muons through the detector's acceptance is expected, prohibiting the detection of very rare decays in a detector, largely occupied by residual muons. To counter the detector's occupation by residual muons, the muon flux needs to be diverted from the acceptance. For this task, a magnetic shield was designed that diverts the muon flux to run past the detector's acceptance. For its optimization, a simulation was used to compute the flux and spectrum of muons emerging from the SHiP target. Because of the tight requirements to background for the SHiP experiment, an experimental validation of the simulation was considered necessary. Therefore, in summer 2018, an experiment was conducted in which a replica of the SHiP proton target was irradiated with $2.81 \cdot 10^{11}$ p.o.t. The spectrum of muons emerging from the target was examined using a drift tube spectrometer and RPC muon tagger.

In the context of this thesis, the drift tube spectrometer used for this measurement has been assembled, commissioned and operated in experiment conditions. Additionally, the tracking performance of the drift tube detector has been examined and methods have been developed, to allow for a track-based alignment of such a detector. This included the implementation of the GBL track fitting algorithm, which was successfully verified with straight tracks. Using a track simulation, the applicability of a track-based alignment has been demonstrated. Additionally, the requirements for an alignment with tracks, reconstructed from real, data have been examined.

Zusammenfassung

Das SHiP Experiment ist ein Beam Dump Experiment, das vorgeschlagen wurde, um sich der Suche nach bisher unbekannten Teilchen, der *Search for Hidden Particles* zu widmen. Dabei soll es den 400 GeV Protonenstrahl des Super Proton Synchrotron Beschleunigers am CERN nutzen. SHiP wird einen Bereich des sog. Hidden Sectors untersuchen, in dem die enthaltenen Teilchen leicht genug sind, um mit heutigen Beschleunigeranlagen zugänglich zu sein, aber so schwach mit bekannten Teilchen wechselwirken, dass sie ihrer Entdeckung bisher wegen zu geringer Strahlintensität oder zu kleiner Detektoren entgangen sind. Die Entdeckung solcher schwach wechselwirkenden Teilchen erfordert eine sehr geringe und gut bekannte Rate an Untergrund-Ereignissen. An einem Beam Dump Experiment wird allerdings eine enorme Zahl an Myonen produziert, die in den Akzeptanzbereich des Detektors eindringen, was die Entdeckung sehr seltener Zerfälle unmöglich machen würde. Daher wurde ein magnetisches Schild entwickelt, das den Fluss der Myonen am Akzeptanzbereich des Detektors vorbei führen soll. Zu dessen Optimierung wurde eine Simulation verwendet, die Auskunft über das zu erwartende Spektrum der Myonen gibt. Auf Grund der starken Anforderungen an den Untergrund für das SHiP Experiment war es nötig, die Daten aus der Simulation experimentell zu bestätigen. Zu diesem Zweck wurde im Sommer 2018 ein Experiment durchgeführt, in dem eine Nachbildung des SHiP Protontargets mit Protonen aus dem SPS mit $2.81 \cdot 10^{11}$ p.o.t bestrahlt wurde. Das Spektrum der Myonen, die dabei das Target verlassen, wurde von einem Driftröhren-Spektrometer in Kombination mit einer Myonen-Identifikation durch einen RPC-Detektor vermessen.

Im Rahmen der vorliegenden Arbeit wurden Teile des Detektors gefertigt, sowie das Spektrometer aufgebaut, in Betrieb genommen und während des Experiments betrieben. Die Qualität der, mit dem Detektor rekonstruierten, Teilchenspuren wurde untersucht und dabei wurde ein neuer Algorithmus zur Spurrekonstruktion implementiert, der eine nachträgliche Ausrichtung des Detektors anhand der mit ihm gemessenen Spuren erlaubt. Die Leistungsfähigkeit sowohl der Spurrekonstruktion, als auch der nachträglichen Korrektur der Detektorausrichtung wurden mittels einer Simulation demonstriert. Zuletzt wurden die Bedingungen dafür untersucht, die Korrektur der Detektorausrichtung anhand realer Daten vorzunehmen.

Contents

1 Introduction

In elementary particle physics, the model describing the particles and their interactions, the Standard Model of Particle Physics (SM in short) is amongst the most successful theories in physics. However, with progress in the fields of particle physics itself but also in astrophysics and cosmology, it became clear that several phenomena cannot be explained by the SM and hence, the SM is at least not a complete theory.

Several models and theories exist, trying to explain the observations diverging from the SM and many experimental efforts are undertaken in order to test these models. Among these experiments is the proposed SHiP[1] experiment. Being a *beam dump* experiment at the *Super Proton Synchrotron (SPS)* accelerator at CERN[2], it is exploring physics *beyond the SM (BSM)* at the intensity frontier. When stopping a high intensity proton beam from the SPS in a massive target, a large number of muons is created alongside the yet unknown particles, which, when entering a tracking detector would imply such a high occupancy that any detection would be rendered impossible. Therefore, a magnetic muon shield was designed for the SHiP experiment. This, however requires knowledge of the muon flux and spectrum emerging the target in order to be optimized. This was performed using numerical simulations. It appeared necessary, to perform an experimental validation of the models used for the simulations, hence a measurement was performed, in which a target SHiP target replica was irradiated using 400 GeV protons from the SPS in four weeks of beam time in summer of 2018. A muon spectrometer was placed behind the target replica enabling the measurement of the flux and spectrum of muons created in processes resulting in the proton interactions.

For this thesis, the spectrometer tracker, set up from drift tubes, was planned, assembled, setup and successfully operated in the before mentioned experiment. This includes the development of a software for detector readout and sending the acquired data to a central *event builder* via a network connection.

Additionally, a new algorithm was implemented for a fit of straight tracks which allows for a track-based alignment using the tracks fitted this way. Its application using the detector setup for measuring the muon flux and spectrum was shown using a Monte-Carlo simulation. Furthermore, challenges when applied to real experimental data are described. This tracking algorithm is very general and can relatively easy be adopted for the SHiP experiment's tracker.

[1] Search for Hidden Particles

[2] Conseil européen pour la recherche nucléaire (*fr*) - European Organization for Nuclear Research

This thesis is structured as follows: A short overview of the SM, especially its shortcomings and some attempts to shed light on those shortcomings is presented in chapter 2. Thereafter, the SHiP experiment is introduced in chapter 3, followed by an introduction to the working principle of drift tube detectors in chapter 4. These chapters constitute the first part of this thesis. The second part addresses the experimental part described here. First, an overview of the experimental aims and layout is given in chapter 5, followed by a detailed description of both the hard- and software of the drift tube spectrometer in chapter 6.

A third part deals with the newly implemented trackfit algorithm and the detector alignment. Here, a mathematical description of the track based alignment as well as the fitting algorithm is presented in chapter 7. Its application to MC tracks is shown in chapter 8 and the analysis of its application to real data is presented in chapter 9. Finally, a conclusion is presented alongside an outlook to future opportunities for the SHiP experiment.

Part I

Theory

2 The Standard Model and Dark Matter

The Standard Model of Particle Physics (short *SM*) is one of the most successful and best examined theories in physics for the past decades. One of the biggest achievements and experimental confirmations of the SM is the discovery of the *Higgs Boson* by the ATLAS [1] and CMS [2] experiments at CERN's LHC. After the Higgs Boson discovery, the standard model is complete. All the particles it predicted have been discovered. However, the SM fails to explain several phenomena in particle physics and cosmology. This shows that the Standard Model cannot explain the composition and even existence of all the matter in our universe. The successes and shortcomings of the standard model will be briefly introduced in this chapter.

2.1 Introduction

The topic of elementary particle physics is a rather young topic in physics research fields. Following the discovery that the electron is a particle much smaller than atoms, in fact a elementary particle, by J.J. Thomson in 1897 [3], a field exploring the contents of atoms quickly evolved. Shortly thereafter, E. Rutherford discovered that atoms have a massive, positively charged nucleus [4] in 1911 and in 1919 that the nucleus of Hydrogen is present in other atoms as well, which is today referred to as the discovery of the proton [5]. After the discovery of the neutron by J. Chadwick in 1932 [6] the constitution of atomic nuclei and especially the existence of isotopes could be explained.

When in the 1950s particle accelerators became available, atomic nuclei were examined with higher energy *projectiles* which led to a series of discoveries of subatomic particles, which is not described in detail in this thesis.

By studying radioactivity, especially the β-decay, it was discovered that the electron escaping a nucleus after its decay has a continuous energy spectrum. This led to W. Pauli's proposal of a very light, neutral particle, which is today referred to as the *neutrino* [7]. According to Pauli's proposal, the neutrino would not, or only very rarely, interact with matter, which is why it was not yet observed in β-decays. The neutrino was later discovered in 1956 by C. L. Cowan, F. Reines et al. [8], when the first high power nuclear reactors were available, producing large numbers of neutrinos, enabling its discovery despite its very low interaction probability.

Theoretically, the elementary particles and their interactions are described by the SM. It predicted a number of fermions, which are the constituents of condensed matter and gauge bosons, which mediate the interactions between fermions. With technological progress, especially in particle accelerators and nuclear reactors, the *zoo* of elementary particles predicted by the SM was discovered over time. This culminated in the discovery of the Higgs Boson [1, 2] in 2012, by which the last particle predicted by the SM was discovered.

2.2 Shortcomings

Despite the great successes and confirmations of its predictions, it became apparent that the SM fails to describe some phenomena that were observed, especially in astrophysics, astroparticle-physics and cosmology. Three very intriguing phenomena are briefly presented in the following.

Baryon Asymmetry of the Universe (BAU) The *Dirac equation*, being the back-bone of particle physics calculations, predicts antiparticles along particles as a solution and so far, for all particles that have been examined, antiparticles have been observed for their corresponding particle.

In the Big Bang, an equal amount of baryonic matter and anti(-baryonic)matter should have been created. However, today we observe a universe which is dominated by matter. The absence of antibaryonic matter cannot be explained by the SM. This asymmetry is called the *Baryon asymmetry of the universe (BAU)*. However, extensions to the SM exist, which can explain the BAU, these require three conditions, which are known as the Sakharov conditions [9]:

1. violation of baryon number,
2. C- and CP violation,
3. deviation from thermal equilibrium.

The violation of the baryon number is required a number of Grand Unification Theories (GUTs) and can be motivated. The baryon number conservation was introduced to explain the stability of matter [10]. The proton, being the lightest baryon with an non-zero baryon number, must be stable if the baryon number was exactly conserved. For electrons, the stability can be explained with charge conservation which is based on a local gauge invariance in quantum electrodynamics. The baryon number conservation, on the other hand, is only a global gauge invariance without an associated mediator [11]. Hence, the observation of a proton decay would be an indicator for the violation of baryon number conservation. By the time of writing this thesis, the proton decay has not been observed. The future *Hyper-Kamiokande* experiment [12], which is planned to begin data acquisition in 2025 will greatly improve the sensitivity over earlier experiments. Currently,

a lower limit on the proton lifetime is set by the Super-Kamiokande experiment with $\tau_p > 7.7 \times 10^{33}$ years [13].

The CP violation is known for the electroweak sector. However, the electroweak CP-violation alone cannot explain the BAU [14]. Hence, extensions to the SM are introduced which do not result in predictions contradictory to experimental observations. One of those extensions is the minimal supersymmetric standard model (MSSM) [14].

The third Sakharov condition, while well motivated theoretically, is not yet supported by experimental evidence [14]. A possible explanation to the BAU is a baryon asymmetry generation from a lepton asymmetry, in a process called leptogenesis [15, 16]. This process can be explained with an extension to the SM in the neutrino sector, called the *Neutrino Minimal Standard Model* (νMSM), which is presented in chapter 2.4.2

Neutrino masses The observation of neutrino oscillations subsequently resulted in the idea that neutrinos must have masses different from zero. A neutrino flavor state is, following the model underlying neutrino oscillations [17, 18], a superposition of mass-eigenstates with masses different from zero. Due to their mass differences, they evolve differently with time resulting in oscillating probabilities, to measure a neutrino as one flavor, while it was emitted as neutrino of a different flavor. The SM, however, predicts neutrinos with masses equal to zero, which was shown to be not the case.

Dark Matter Astrophysical and cosmological observations, for example of galaxies [19] or galaxy clusters, show that their gravitational interaction cannot be explained by the mass of the visible matter they consist of. This observation led to the idea that there must be matter in galaxies which interacts through gravitation but otherwise does not couple to standard model particles.

From the standard cosmological model ΛCDM [20], the abundance of dark matter in the universe can be estimated to about 25.8% of the total energy content of the universe [21, 22].

While the whole topic of dark matter cannot be covered in the context of this thesis, more detail on some candidates for dark matter are given in chapter 2.3. One exception is the neutrinos' role in the dark matter puzzle, which is described in chapter 2.4.

2.3 Dark Sector and Dark Matter

The failing of the standard model to explain several observations shows that the SM is at least an incomplete theory. It became apparent that new, yet undiscovered particles and interactions needed to be introduced to explain astrophysical and cosmological observations. This, yet unexplored part of particle physics can be called the *dark sector or hidden sector*. Dark Matter (DM), on the other hand, describes yet unknown particles with properties able to explain cosmological observations. Hence, not all of the particles

in the dark sector are necessarily dark matter. They might either be massless or short lived, thus they cannot explain the mass excess in galaxies and galaxy clusters in the universe.

2.3.1 Overview

Dark Matter is categorized into *thermal* and *non-thermal* dark matter. For thermal DM it is assumed that it was created at the Big Bang in thermal equilibrium with baryonic matter. Dark matter particles that are relativistic today are called *hot dark matter (HDM)*, those that are non-relativistic are called *cold dark matter (CDM)*. As it is known today that neutrinos do have masses, they could contribute to HDM. However, HDM alone is not able to solve the whole puzzle of dark matter as HDM excesses the escape velocity of galaxies, hence HDM would not cluster on the scale of galaxies but rather on the scale of galaxy clusters. Cosmological observations, however, showed that galaxies formed first and then the galaxies themselves clustered [23].

CDM on the other hand could explain the observed structure of the universe but here, no particles were observed so far that could be a part of CDM.

In between, *warm* DM can be defined with high velocities but low enough to not conflict with cosmological observations.

For non-thermal dark matter, creation at thermal equilibrium is no longer considered but rather different creation mechanisms. Axionic dark matter is an example for a non-thermal DM, which is described in chapter 2.3.2.

2.3.2 Axions and Axion-Like Particles

While CP violation for the *electroweak interaction* can be observed at a number of phenomena, such as the decay of Kaons [24], or recently charmed D^0 mesons by the LHCb experiment [25], it has not yet been observed for the strong interaction. A broken CP symmetry in QCD would for example imply a non-vanishing electric dipole moment for the neutron. However, precision measurements of its dipole moment yield upper limits many orders of magnitude smaller than the smallest predictions under the assumption of CP violation [26]. So far, it seems like the strong interaction is invariant under CP transformations, even though the underlying theory would allow it to be break invariance, as shown by *G. t' Hooft* [27, 28].

A conservation of CP symmetry in strong interactions, however can have two reasons. Either at least one of the quarks has a vanishing mass or the *vacuum angle* θ introduced by t' Hooft must have a value very close to zero. The experimental results, however, are consistent with non-zero masses of all quark types, thus it is assumed that the value of θ is close to zero. As there is no good reason for the strong interaction to conserve CP symmetry, explanations were searched for this *strong CP problem*.

As a possible explanation to why such small values of θ are realized, a new, spontaneously broken symmetry was proposed [29] which would require the introduction of a new, *pseudoscalar* particle which got known as the *axion* [30, 31]. This first, so called *QCD axion* has a mass tightly bound to the scale f_A of the newly introduced symmetry [32]. Modifications to the theory arose with less strict mass bounds, resulting in particles behaving similar to the axion but possible masses in a wide range [33, 34], which got known as a group of *axion-like particles (ALPs)*.

For the axion and ALPs, an interaction Lagrangian can be defined as [34]:

$$\mathcal{L}_{\text{axion}} = \mathcal{L}_{\text{SM}} + \mathcal{L}_{\text{DS}} + \underbrace{\frac{a}{4f_\gamma} F_{\mu\nu}\tilde{F}_{\mu\nu}}_{\text{di-photon coupling}} + \underbrace{\frac{a}{4g_G} \text{Tr} G_{\mu\nu}\tilde{G}_{\mu\nu}}_{\text{di-gluon coupling}} + \underbrace{\frac{\partial_\mu a}{f_l} \sum_\alpha \bar{l}_\alpha \gamma_\mu \gamma_5 l_\alpha + \frac{\partial_\mu a}{f_q} \sum_\beta \bar{q}_\beta \gamma_\mu \gamma_5 q_\beta}_{\text{fermion coupling}} \tag{2.1}$$

Here, the dark sector Lagrangian may contain new states providing a UV completion [34]. It contains terms describing an interaction with photons, with gluons, leptons or quarks. For simplification, a single ALP state a is considered with *one* of the couplings defined in equation (2.1) dominant.

Of special interest are two cases because they are possibly accessible to experimental examination. These are in particular:

1. coupling to massless particles (photons, gluons)

2. coupling to light mediators (dark photon, dark scalar, ...)

For ALPs coupling to massless photons or gluons, the mass scale for a from the sub-eV range up to the GeV mass range [34]. Coupling to light mediators, on the other hand, would result in ALP masses in the MeV to GeV range.

Among axions and ALPs there are candidates for cold dark matter [35, 36], hence they are many experiments looking for them in several regions, mostly focusing on their *conversion* to photons in magnetic fields and detecting these photons.

A possible production method for ALPs is the fusion of two photons to one ALP, the so-called *Primakoff mechanism* [37]. Production via the Primakoff mechanism can, for example, happen in the sun [38] and campaigns were started using magnetized, optically closed, helioscopes to detect solar axions. These experiments exploit the solar flux of axions and convert them in strong magnetic fields to SM photons. One of these experiments is *CERN axion solar telescope (CAST)* [39, 40], which uses a prototype dipole magnet from the *Large Hadron Collider (LHC)* as telescope tube. This magnet provides a magnetic field of $\sim 9\,\text{T}$ over a distance of $9.3\,\text{m}$ [39]. A successor experiment, the *International AXion Observatory (IAXO)*, exploiting the same detection mechanism is planned [41], which covers a much improved parameter space for axion and ALP detection compared to CAST.

The production of ALPs via the *Primakoff* process, however is also accessible to accelerators at fixed targets, for example in coherent scattering of protons on nucleons, which is sketched in figure 2.1. This is particularly interesting because the Primakoff production

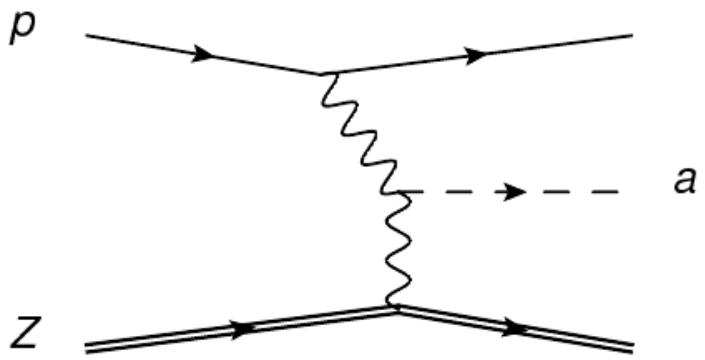

Figure 2.1: Production of an ALP through the Primakoff process, where two photons fuse to one ALP a. These photons might for example mediate the scattering of a proton p on a nucleus Z in a fixed target at accelerator experiments [42].

at beam dumps produces ALPs with small transverse momenta [42]. Therefore, a relatively small detector at a great distance can still have a good acceptance. This enables for example the SHiP experiment to explore ALPs with long decay lengths. The SHiP experiment's sensitivity to ALPs is covered in section 3.4.3.

2.4 Neutrinos Beyond the Standard Model

In the Standard Model, neutrinos are considered massless. Since the discovery of neutrino oscillations following the observation of a deficit on the solar neutrino flux in the *Homestake* experiment [43], it is known that in order to explain their oscillation, they must have masses different from zero. This shows that the Standard Model is at least an incomplete model and the question arises, through what process, neutrinos are given their mass. Furthermore, the scale of the neutrino masses, compared to other fundamental particles, is remarkably small. The question, why the neutrino masses are orders of magnitude smaller than those of any other lepton is still unanswered.

2.4.1 The See-Saw Mechanism

Based on the *Dirac equation*, which is the relativistic wave equation for fermions, it can be derived that neutrinos, which in the standard model do only appear in *left-handed* projections, must have a *Dirac-mass* m_D equal to zero. This section follows [44], where a more complete derivation is presented.

In the following text, ψ^c denotes the *charge conjugation* of ψ, hence the spinor for the anti-particle of ψ.

When the *Euler-Lagrange* equation is applied to the *Lagrangian* $\mathcal{L}$, which is shown in equation (2.2), the Dirac equation can be deduced.

$$\mathcal{L} = \bar{\psi}\left(i\gamma_\mu \frac{\partial}{\partial x_\mu} - m_D\right)\psi \tag{2.2}$$

This Lagrangian contains the so-called Dirac mass term

$$\mathcal{L}_m = m_D \psi \bar{\psi}. \tag{2.3}$$

Requiring the Lagrangian to be Hermitian implies that the Dirac mass m_D from equation (2.3) needs to be real.

Using the *chiral projections* of the Dirac spinors, the Dirac mass term can be written using the *Weyl notation*, as

$$\mathcal{L}_m = m_D\left(\bar{\psi}_L\psi_R + \bar{\psi}_R\psi_L\right). \tag{2.4}$$

When equation (2.4) is applied to neutrinos, both chiralities of neutrinos must have a Dirac mass term as shown above. The SM, however, only allows left-handed neutrinos, thus they cannot have a non-vanishing Dirac mass.

By introducing a complex *Majorana mass* m_M, another hermitian mass term, the so called *Majorana mass term* can be formulated as

$$\mathcal{L}_M = \frac{1}{2}(m_M\bar{\psi}\psi^c + m_M^*\bar{\psi}^c\psi). \tag{2.5}$$

By again applying the chiral projection operators, Majorana mass terms for left- and right-handed neutrino fields can be written as follows:

$$\mathcal{L}^L = \frac{1}{2}m_L(\bar{\psi}_L\psi_R^c + \bar{\psi}_R^c\psi_L) \tag{2.6}$$

$$\mathcal{L}^R = \frac{1}{2}m_R(\bar{\psi}_L^c\psi_R + \bar{\psi}_R\psi_L^c) \tag{2.7}$$

Here, m_L and m_R are real Majorana masses since the mass term is required to be hermitian.

The most general mass term that can be written now, is the *Dirac-Majorana mass term*, which is the combination of the Dirac- and the Majorana mass term:

$$2\mathcal{L} = \bar{\Psi}_L M \Psi_R^c + \bar{\Psi}_R^c M \Psi_L \tag{2.8}$$

In equation (2.8), M denotes the matrix

$$M = \begin{pmatrix} m_L & m_D \\ m_D & m_R \end{pmatrix}, \tag{2.9}$$

and the fields $\Psi_{L,R}$ are:

$$\Psi_L = \begin{pmatrix} \psi_L \\ \psi_L^c \end{pmatrix} = \begin{pmatrix} \psi_L \\ (\psi_R)^c \end{pmatrix}$$
$$(\Psi_L)^c = \begin{pmatrix} (\psi_L)^c \\ \psi_R \end{pmatrix} = \begin{pmatrix} \psi_R^c \\ \psi_R \end{pmatrix} = \Psi_R^c$$

If CP conservation is required, all elements of M must be real. It comes as an experimental fact, that for interactions of real neutrinos, only the fields ψ_L and ψ_R^c are in effect. Those are often referred to as *active neutrinos*. The fields ψ_R and ψ_L^c do not interact and are called *sterile neutrinos*. In the following text, the active neutrinos will be denoted by the letter ν, the sterile neutrinos with an N. Following this, we get:

$$\psi_L = \nu_L$$
$$\psi_L^c = N_L$$
$$\psi_R = N_R$$
$$\psi_R^c = \nu_R$$

The mass eigenstates, using the naming convention introduced above, are:

$$\psi_{1L} = \cos\theta\psi_L - \sin\theta\psi_L^c \qquad \psi_{1R}^c = \cos\theta\psi_R^c - \sin\theta\psi_R$$
$$\psi_{2L} = \sin\theta\psi_L + \cos\theta\psi_L^c \qquad \psi_{2R}^c = \sin\theta\psi_R^c + \cos\theta\psi_R$$

The mixing angle θ is given by:

$$\tan(2\theta) = \frac{2m_D}{m_R - m_L} \tag{2.10}$$

The mass eigenvalues are

$$m_{1,2} = \frac{1}{2}\left((m_L + m_R) \pm \sqrt{(m_L - m_R)^2 + 4m_D^2}\right). \tag{2.11}$$

A special case of the mass eigenvalues follows from the assumption $m_R \gg m_D$ and $m_L = 0$ as the left handed, sterile neutrino shall not participate in the weak interaction. This corresponds to $\theta \ll 1$. Then, the mass eigenstates can be written as [44]

$$m_\nu \equiv m_1 = \frac{m_D^2}{m_R}, \qquad m_N \equiv m_2 = m_R\left(1 + \frac{m_D^2}{m_R^2}\right) \approx m_R. \tag{2.12}$$

In equation (2.12), the subscript ν denotes the mass eigenstate of an active neutrino, N of a sterile neutrino.

This way, the large mass difference between active neutrinos and all the other fermions can be explained. A smaller Dirac mass in this model would result in larger Majorana mass and vice versa. This is why this model is referred to as the *see-saw mechanism* [45, 46, 47, 48, 49].

2.4.2 νMSM

As shown above, neutrinos with both a Dirac- and a Majorana mass would result in light active neutrinos and *at least* one heavy, right-handed neutrino. An extension to the SM, referred to as the neutrino minimal standard model (νMSM), adds three heavy, right handed neutrinos to the standard model particles, as illustrated in figure 2.2. The

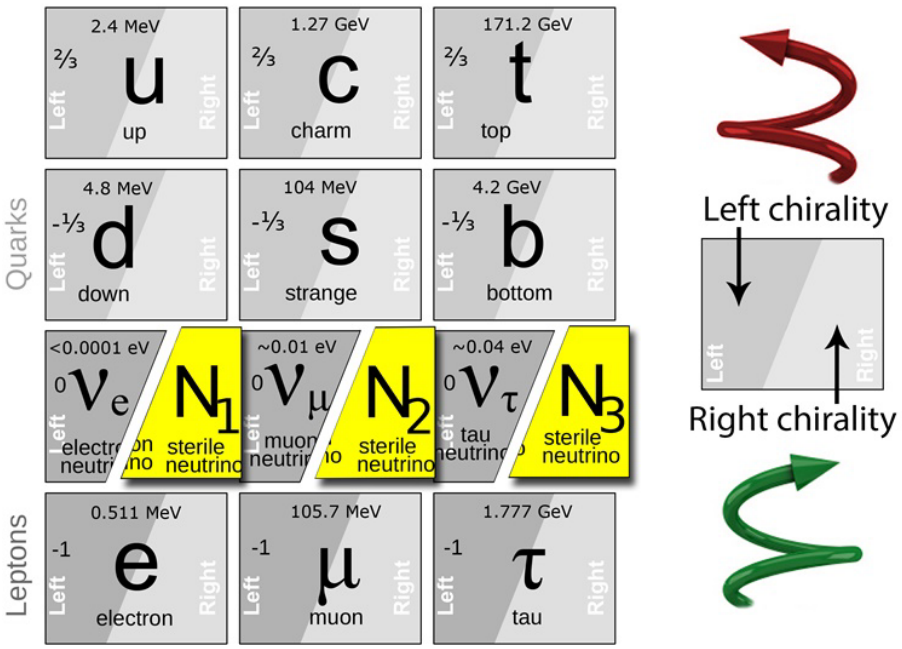

Figure 2.2: The SM fermions with additional right handed neutrino states N_1, N_2, N_3 that don't participate in SM interactions, thus are called *sterile* [50].

state N_1 has a mass of $\mathcal{O}(10\,\text{keV})$ and is considered stable. This would be a candidate for warm dark matter [51]. The states N_2 and N_3 are heavy with masses $\mathcal{O}(1\,\text{GeV})$ and would explain the small masses of the active neutrinos through the see-saw mechanism and could explain the BAU via leptogensis [52].

In the following chapters, the right handed neutrino states are referred to as *Heavy Neutral Leptons (HNL)*. They are among the benchmark models for the SHiP experiment, which is outlined in chapter 3.

2.5 Portal models

In the context of this thesis, only such models are considered that can be described as a quantum field theory (QFT). If extensions to the SM can be described as QFT, these imply new Lagrangian terms. In order to be able to detect new particles using standard particle physics techniques, it is required that they have some sort of interaction with SM particles, even if it is very small. The Lagrangian of an extended SM could then be written as shown in equation (2.13).

$$\mathcal{L} = \mathcal{L}_{SM} + \mathcal{L}_{portal} + \mathcal{L}_{DS} \tag{2.13}$$

It consists of the SM Lagrangian $\mathcal{L}_{SM}$ and a *dark sector* Lagrangian $\mathcal{L}_{DS}$. Additionally, it contains a term $\mathcal{L}_{portal}$ which describes the coupling between new particles and SM particles. Requiring a gauge invariance of the Lagrangian, it can be constrained to a few types of portal terms which are shortly outlined in the following.

A special case is the interaction of ALPs with SM particles, which is already outlined in chapter 2.3.2.

2.5.1 Vector Portal

By requiring gauge invariance under a new $U(1)$ transformation, in analogy to standard Quantum Electrodynamics (QED), a new vector potential A' is introduced with a field strength tensor F'. Thereby, a new vector boson is introduced, which, in analogy to QED, is called *dark photon*. Hence, this portal is called the *vector portal*.

A portal, connecting SM and DS could be kinematic mixing between SM photons and hidden photons via a term

$$-\frac{1}{2}\epsilon F_{\mu\nu}A'^{\mu\nu}$$

where ϵ is the coupling strength to the SM [53, 54]. Following this model, dark photons could be created through *high energy* photons, which can originate in a number of processes. As dark photons are mixed with standard photons through their field strength tensors, dark photons share the photon interactions with SM particles, suppressed by ϵ. Hence, they can decay, if kinematically allowed, via pair-production. This could either be visible SM fermions or invisible to dark sector particles χ. This is possible due to their dark sector Lagrangian as shown in equation (2.14) [34].

$$\mathcal{L}_{\mathrm{DS}} = -\frac{1}{4}\left(F'_{\mu\nu}\right)^2 + \frac{1}{2}m^2_{A'}\left(A'_{\mu}\right)^2 + \left|\left(\partial_\mu + ig_D A'_\mu\right)\chi\right|^2 + \dots \tag{2.14}$$

Through its dark sector Lagrangian, the dark photon could also serve as a mediator for dark matter, especially light dark matter.

2.5.2 Scalar Portal

After the discovery of the Higgs Boson, nature's realization of scalar bosons is experimentally validated. A simple extension of the SM could involve a coupling of a new singlett field S to the SM Higgs doublett H via

$$\mathcal{L}_{\text{scalar}} = \mathcal{L}_{\text{SM}} + \mathcal{L}_{\text{DS}} - (\mu S + \lambda S^2)(H^\dagger H) \tag{2.15}$$

In eq. (2.15), two new couplings μ and λ are introduced. Non-zero values of μ lead to coupling of the new field S to the SM Higgs field h, while non-zero values of λ imply a coupling to a pair of S.

2.5.3 Neutrino Portal

The νMSM[1] proposes the addition of three heavy, right handed neutrinos N to the SM that have the potential to explain a number of shortcomings of the SM. These *Heavy Neutral Leptons (HNL)* couple to the SM via the neutrino portal as shown in equation (2.16) [34].

$$\mathcal{L}_{\text{neutrino}} = \mathcal{L}_{\text{SM}} + \mathcal{L}_{\text{DS}} + \sum_{\alpha,I} F_{\alpha I}(\bar{L}_\alpha H) N_I \tag{2.16}$$

Here, α denotes the flavor of the lepton doublets L_α and I the generation of the HNL. The couplings $F_{\alpha I}$ are the corresponding Yukawa couplings [34].

This term mixes the HNL with active neutrinos when kinemetically possible via a new mixing matrix U.

[1] See chapter 2.4.2.

3 The SHiP experiment

SHiP is an acronym and stands for Search for Hidden Particles. This chapter will first give an overview of the planned detector, followed by the physics goals of the SHiP experiment both for the detection of hidden particles as well as for the studies of some properties of neutrinos, for which SHiP also offers unique opportunities. After that, the parts of the SHiP detector will be explained in more detail. This work is mainly based on [50, 34] for the physics side and [55, 56, 57] concerning the detector layout and technical details.

3.1 Detector Overview

SHiP is a *beam dump experiment*. A proton beam is extracted from the SPS accelerator and stopped in a massive target. Among the many particles created by the proton interactions in the target might be new, yet undiscovered particles, which SHiP aims to find. In particular, SHiP looks for neutral particles with decay lengths at the scale of $\sim 50\,\mathrm{m}$ and final states containing SM particles[1].

For this task, a detector is proposed with a total length of $\sim 120\,\mathrm{m}$. First, the protons impact on the proton target, where a whole *spill*[2] of protons is absorbed. Alongside the unknown, *hidden particles*, a huge number of muons is produced in the proton target. In order to be able to detect the hidden particles, which are expected to interact very weakly, these muons need to be diverted away. Therefore, a magnetic muon shield is planned, after which the *Scattering and Neutrino Detector* (SND) is situated. In addition to a rich program of neutrino physics, this has the ability to perform *light dark matter* (LDM) searches through scattering. Further downstream of the SND, a conical shaped, evacuated decay vessel for the neutral, hidden particles is located. At its downstream end, a spectrometer tracker is placed, using straw tubes as tracking component. This *spectrometer straw tracker* (SST) fulfills the tasks of reconstructing the decay vertex of hidden sector particles in the decay vessel as well as measuring the momenta of their decay daughters. It is followed by a timing detector, providing global time stamps for the events recorded at SHiP with a high resolution. Downstream the timing detector, an electromagnetic calorimeter is placed, followed by a muon identification system. The last two provide particle identification. A sketch of the whole SHiP detector is shown in figure 3.1. All the detector parts are outlined in section 3.3.

[1] See section 3.2 for more details.

[2] An extraction unit containing 4×10^{13} p.o.t, see section 3.3.1 for details.

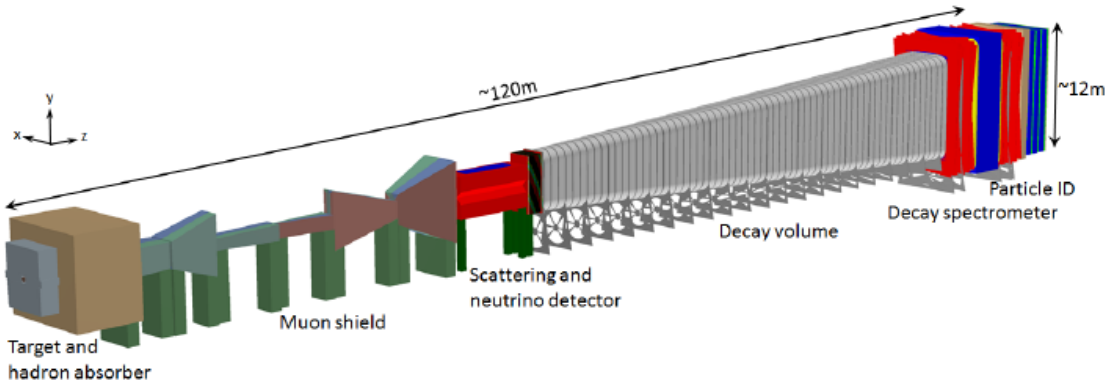

Figure 3.1: Schematic overview of the SHiP experimental setup [56].

3.2 Goals

The SHiP experiment, as its name suggests, is mainly aimed at exploring a large parameter space for the detection of yet unknown particles. Here, SHiP allows the exploration of a number of models, with an overview given in [50]. On the other hand, SHiP also offers opportunities to explore some properties of neutrinos, for which it contains a dedicated sub-detector. The physics goals will be outlined in some more detail in the following.

3.2.1 Hidden Particle Searches

Hidden particles are particles that have evaded detection so far, which can be the case due to one of the following reasons:

1. They have masses so high that their creation is inaccessible with current day accelerators and colliders

2. Their coupling to standard model interactions is so small that they are not observed in a statistically relevant frequency.

This implies the possibility to explore the *hidden sector* (HS) in two ways. The first option is to look for their signatures in using accelerators providing higher energies. This way is called the *energy frontier*. Alternatively, one could use a very high intensity beam of an accelerator that is already present and maximize the production of possible particles in a mass range in reach of this beam energy. This second regime is called the *intensity frontier*. These options are sketched in figure 3.2. SHiP is a proposed experiment aimed at exploring the *intensity frontier*. It will be situated at CERN's SPS, using its high intensity, 400 GeV proton beam and dumping entire *spills* of protons into a massive target. Hence, SHiP is categorized among the group of *Beam Dump Experiments*. SHiP can perform a model independent search for HS particles through its capability to fully reconstruct events, including particle identification, and explore the parameter space for a number of models

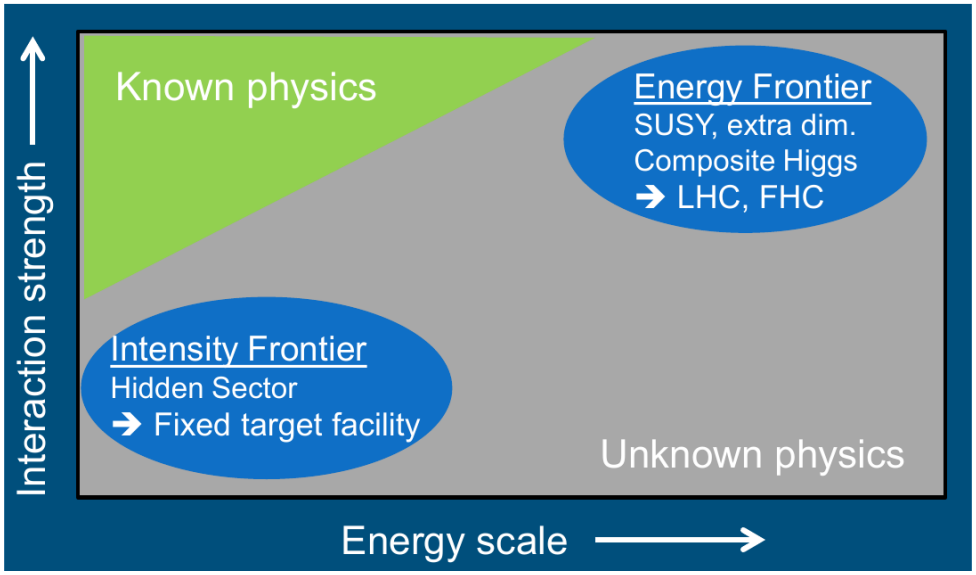

Figure 3.2: Sketch illustrating the possibility to search for new particles at either the intensity frontier or the energy frontier. Intensity frontier searches assume very weak couplings of yet undiscovered particles to SM interactions, hence long lifetimes. Energy frontier searches, on the other hand, assume masses of new particles so high that earlier accelerators were unable to overcome the energy threshold for their creation [50].

about hidden particles. One of the benchmark searches for SHiP is the search for Heavy Neutral Leptons, which are right-handed, sterile neutrinos as described in chapter 2.4.2. Additionally, SHiP can explore the couplings for a number of portal models (introduced in section 2.5) and be sensitive through these portals to dark photons, ALPs or dark scalar particles. The sensitivities to these particles will be outlined in section 3.4. For a more complete overview of SHiP's physical reach, see [50]. For the HNL search, SHiP offers the opportunity to utilize an unprecedentedly high beam intensity provided by the SPS with a large decay volume and geometrical detector acceptance. Some properties of experiments searching for HNLs are listed for comparison in table 3.1.

Table 3.1: Experiments dedicated to search for HNLs in comparison [55]

Experiment	PS191[58, 59, 60]	NuTeV[61]	CHARM[62]	SHiP
Proton energy (GeV)	19.2	800	400	400
Protons on target ($\cdot 10^{19}$)	8.86	0.25	0.24	20
Decay volume (m^3)	360	1100	315	1780
Decay volume pressure (bar)	1 (He)	1 (He)	1 (air)	10^{-6} (air)
Distance to target (m)	128	1400	480	80-90
Off beam axis (mrad)	40	0	0	0

3.2.2 Neutrino Physics

In addition to the exploration of the hidden sector, SHiP can also deepen knowledge in the neutrino sector. Amongst many other opportunities, SHiP will be able to provide the first ever *direct observation* of the anti-tau-neutrino $\bar{\nu}_\tau$.

The production of tau neutrinos happens in the proton target. The SHiP proton target[3] is optimized for the production of heavy, charmed mesons, in particular $D_s^\pm$ mesons. This is due to these mesons' comparably high rate of (purely) leptonic decays via a tau lepton, accompanied by an associated neutrino. An overview of the leptonic decay channels of the D_s mesons is shown in table 3.2, for a full overview see [21]. The D_s meson can

Table 3.2: Branching ratios for purely leptonic decays of D_s mesons. The values shown in the table are for the D_s^-, they are also true for its charge conjugate [21].

channel	branching ratio
$D_s^- \to \tau^- \bar{\nu}_\tau$	$(5.48 \pm 0.23)\%$
$D_s^- \to \mu^- \bar{\nu}_\mu$	$(5.50 \pm 0.23) \cdot 10^{-3}$
$D_s^- \to e^- \bar{\nu}_e$	$< 8.3 \cdot 10^{-5}$

decay in a number of additional channels. Here, only the main contributions producing neutrinos are listed as these can escape the proton target, where they are produced, and pass through the muon shield. Note that the leptonic decay channels of D_s meson are dominated by the decay to the τ flavor. Hence, due to the target optimization in order to produce these mesons, the yield of $\bar{\nu}_\tau$ is maximized.

While tau neutrinos are already produced in the decay of D_s mesons as shown above, another source is the subsequent decay of τ leptons. The dominant branching ratios are summarized in table 3.3. Example Feynman diagrams showing the production of τ

Table 3.3: Branching ratios for the decay of τ^- leptons [55, 21]. Here, h denotes a charged hadron, in this case limited to pions and kaons. It can be seen that the decay of τ leptons is dominated by channels with at least one hadron in the final state. The decay modes for τ^+ are the charge conjugate.

channel	branching ratio
$\tau^- \to h^- \nu_\tau (+n\pi^0)$	49.5%
$\tau^- \to h^- h^- h^- \nu_\tau (+n\pi^0)$	15.0%
$\tau^- \to \mu^- \bar{\nu}_\mu \nu_\tau$	17.7%
$\tau^- \to e^- \bar{\nu}_e \nu_\tau$	17.8%

neutrinos at SHiP are presented in figure 3.3. The expected spectra of the ν_τ both from the D_s meson and the τ lepton decays are shown in figure 3.4.

[3] For more information on the target see chapter 3.3.2.

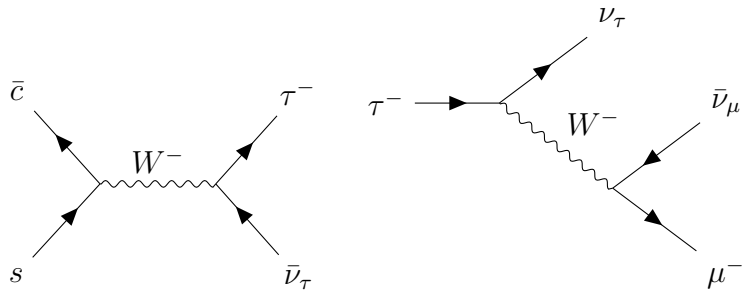

(a) D_s^- decay (b) τ decay

Figure 3.3: Production processes of ν_τ in decays of D_s mesons (left) and τ leptons (right). Production of $\bar{\nu}_\tau$ is the same with all particles changed to their anti particles. For the decay of the tau lepton, for simplicity, only the muonic decay channel is shown. A list of the most dominant decay channels of the tau lepton is given in table 3.3.

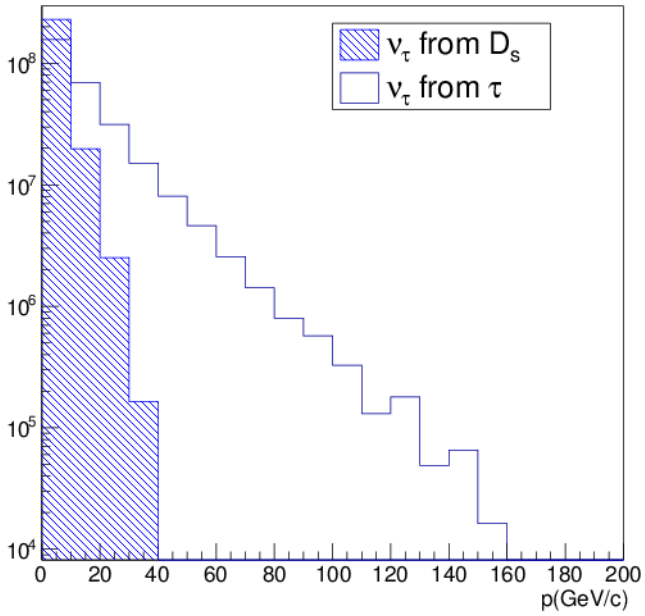

Figure 3.4: Expected spectrum of τ-neutrinos produced at SHiP from different decays. The ν_τ produced in decays of D_s mesons are shown as shaded area. Also shown are the neutrinos produced in decays of the τ lepton [55].

Additionally, thanks to the high intensity proton beam dumped in a massive target, a high flux of neutrinos is produced in decays of secondary particles, which enables SHiP to perform high statistics neutrino physics. The expected spectra of neutrinos produced in the target, as well as detected in the dedicated neutrino detector are shown in figure 3.5. An overview of the estimated number of neutrinos, detected via CC deep-inelastic scattering (DIS) interactions is shown in table 3.4.

The flux of τ flavored neutrinos establishes the SHiP experiment's ability to study the

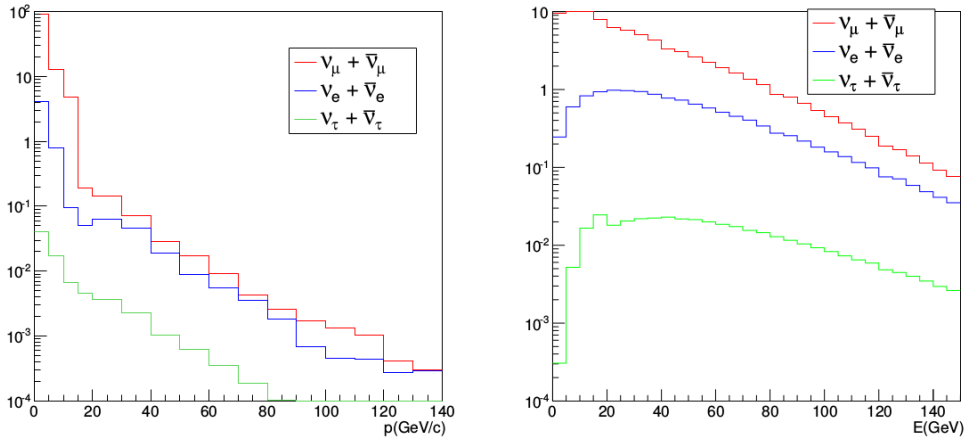

Figure 3.5: Expected spectra of produced (left) and detected (right) neutrinos at SHiP. The total number of neutrinos is normalized to 100. In addition, an energy cut at 0.5 GeV was applied for electron and muon neutrinos [55].

Table 3.4: Expected number of neutrinos and their mean energies $\langle E \rangle$ undergoing CC DIS interactions at the SHiP neutrino sub-detector for $2 \cdot 10^{20}$ protons on target [55].

flavor	$\langle E \rangle$ [GeV]	number of interactions
ν_e	46	$2.5 \cdot 10^5$
ν_μ	29	$1.7 \cdot 10^6$
ν_τ	59	$6.7 \cdot 10^3$
$\bar{\nu}_e$	46	$9.0 \cdot 10^4$
$\bar{\nu}_\mu$	28	$6.7 \cdot 10^5$
$\bar{\nu}_\tau$	58	$3.4 \cdot 10^3$

differential cross section for neutrinos' deep inelastic scattering via CC interactions. For a neutrino with a given flavor ℓ, the differential cross section $\frac{d^2\sigma^{\nu(\bar{\nu})}}{dxdy}$ is given by

$$\begin{aligned}\frac{d^2\sigma^{\nu(\bar{\nu})}}{dxdy} = \frac{G_F^2 M E_\nu}{\pi(1+Q^2/M_W^2)} \Bigg(\left(y^2 x + \frac{m_\ell^2 y}{2E_\nu M}\right) F_1 + \left(\left(1 - \frac{m_\ell^2}{4E_\nu M}\right) - \left(1 + \frac{Mx}{2E_\nu}\right)\right) F_2 \\ \pm \left(xy\left(1 - \frac{y}{2}\right) - \frac{m_\ell^2 y}{4E_\nu M}\right) F_3 + \frac{m_\ell^2 (m_\ell^2 + Q^2)}{4E_\nu^2 M^2 x} F_4 - \frac{m_\ell^2}{E_\nu M} F_5 \Bigg)\end{aligned} \tag{3.1}$$

This contains the so-called *structure-functions* F_1 through F_5. In equation (3.1), M denotes the mass of the nucleus a neutrino scatters on, Q the momentum transfer and m_ℓ the mass of the charged lepton corresponding to the interacting neutrino. For electron- and muon neutrinos, the terms proportional to the structure-functions F_4 and F_5 can be neglected [63]. For τ neutrinos, due to the high mass of the charged lepton, SHiP can test the hypothesis $F_4 = F_5 = 0$ in five years of data acquisition [55].

3.3 Experimental Site and Layout

The SHiP experiment consists of many subdetectors which will be briefly presented in this section. Being a beam dump experiment, all the subsystems follow downstream the primary proton target. A schematic overview of the SHiP experiment is shown in figure 3.1.

All subsystems will be presented in the order they are located in the experiment beginning at beam delivery to the most downstream detector parts. However, since being the most important parts within the context of this thesis, a focus will be on the proton target (section 3.3.2) and the muon shield (section 3.3.3).

3.3.1 Beam Dump Facility and Beam Transfer

As part of work carried out by CERN's *Physics Beyond Colliders* (PBC) working group [34], the concept of the *Beam Dump Facility* (BDF) was developed, with a dedicated subgroup of the PBC working on it. It describes a dedicated experimental area with SHiP as prominent user of the newly constructed SPS beam lines supplying protons. It is foreseen to be constructed close to the existing North Area experimental area. A sketch of the integration of the BDF beam transfer to the existing North Area beam lines is shown in figure 3.6. Special sets of beam optics able to perform efficient beam splitting between

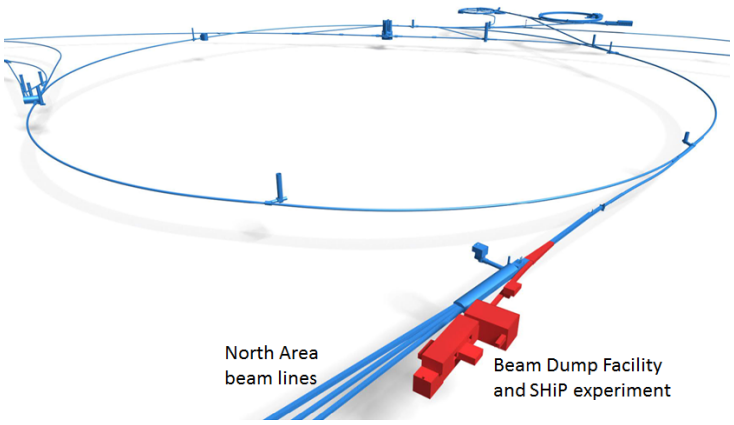

Figure 3.6: Overview of the existing beam injector sysmtes (blue) at CERN with the new system needed for SHiP highlighted in red. SHiP is planned with minimal required work on beam transfer lines and injection system in mind [56].

the BDF and the North Area have already been developed and tested [56]. The protons are supplied using the ability of the SPS to perform a *slow extraction*. It provides 400 GeV protons in *spills* of 4×10^{13} protons on target (p.o.t) extracted over a time span of one second. This sums up to an annual proton yield of 4×10^{19} p.o.t [56]. This proton yield enables SHiP to reach the proposed 2×10^{20} p.o.t [55] within five years of data taking.

3.3.2 Proton target

The SHiP proton target must fulfill the task of stopping the primary proton beam from the SPS as well as being optimized with respect to the production of charmed mesons, namely D_s. Alongside these, the interactions of the protons stopped in a massive target create a number of pions and kaons, which when decaying subsequently produce a large flux of muons and associated neutrinos. This flux, on the other hand, should be minimized by the target design. This can be achieved by using a *long* and dense target, efficiently stopping the pions and kaons before they can decay. Thus, the target must be made from a material with high atomic mass and charge.

The target design was optimized [64] using a simulation of the hadronic interactions in the target material using the event generator FLUKA [65, 66]. The current design foresees a cylindrical target with longitudinally segmented blocks of target material. Its diameter is 250 mm in order to maximize the ability to stop hadrons with high transverse momenta in the target as efficient as possible.

The upstream part of the target consists of 13 molybdenum cylinders with a total length of 58 cm. In particular, due to its better resistance to thermal and mechanical stress compared to pure molybdenum, an alloy of titanium, zirconium and molybdenum (TZM) was chosen [64]. Downstream the TZM cylinders, an additional five cylinders of pure tungsten are placed with a total length of 78 cm [64]. In total the TZM- and tungsten cylinders equal to $\sim$ 12 hadronic interaction lengths λ. The target blocks are housed in a vessel made from stainless steel. A sketch of the proton target design is shown in figure 3.7.

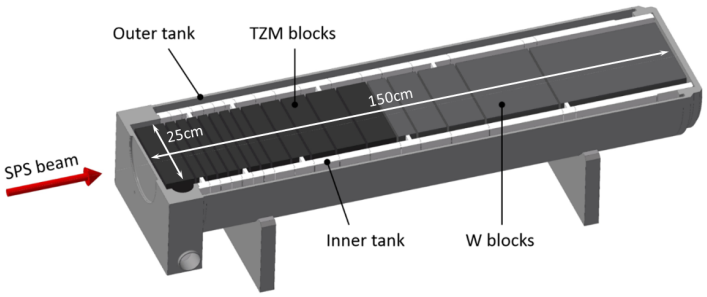

Figure 3.7: Preliminary target assembly layout. The TZM and tungsten blocks are housed in the inner vessel made of stainless steel, which embodies the target's water cooling [56].

The SPS provides a high intensity proton beam with an average beam power of 350 kW. It is delivered in *spills* with a peak power of 2.56 MW, hence active water cooling of the target will be required. Therefore, the target material cylinders are interleaved with 5 mm slids used for water cooling. In order to prevent damage to the target material through corrosion induced by the cooling water, each material cylinder is cladded with a tantalum-tungsten alloy [64]. The *hybrid* target design using TZM in the first part, which

has a lower atomic charge and density, compared to tungsten is chosen in order to better distribute the power dissipated in the target. The estimated density of energy deposited in the target as a function of its length is shown in figure 3.8.

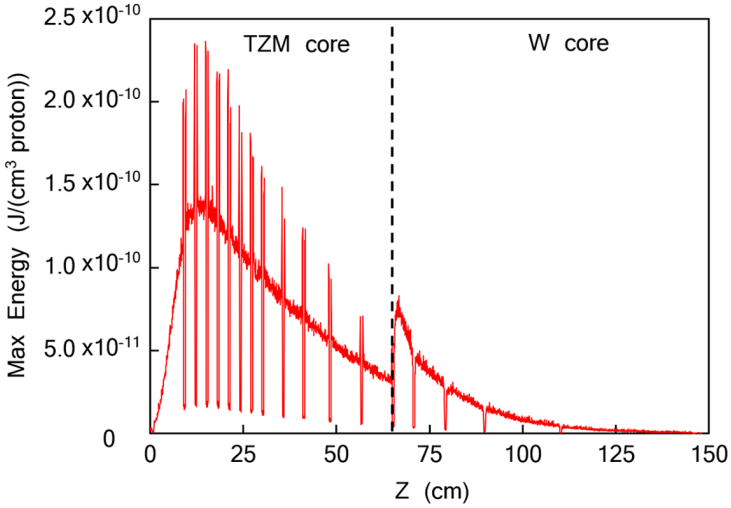

Figure 3.8: Energy deposited in the target per proton as a function of the depth z within the target along the beam axis. The drops of the energy deposition in the slids for water cooling can clearly be seen. In the first part of the target, peaks at both ends of each target material block can be seen. These are due to the cladding material, which has a higher density compared to the TZM material. Image taken from [64].

3.3.3 Muon Shield

Per spill of protons stopped in the target, a total of $\sim 5{\cdot}10^{19}$ muons are produced alongside the particles of interest for the SHiP experiment [55]. These must be diverted away from the SHiP detector acceptance as they would otherwise be a background rendering the physics program of SHiP impossible. Therefore, a two step process is foreseen. First, a separation of opposite charged muons is performed as close to the proton target as possible. While the magnetization of the proton target itself is not practically possible [56], the 5 m long, iron hadron stopper downstream the proton target can be magnetized utilizing a coil situated above it. The hadron stopper as well as the coil used for magnetizing it are shown in figure 3.9. The now charge separated muons then enter a free-standing, magnetic muon shield, of which a layout is shown in figure 3.10. Its working principle is sketched in figure 3.11. Briefly summarized, by alternating field orientations and repeating, conical shapes, muons bent back into the detector acceptance by the return field of one magnet element are then diverted away again by the, now opposite sign, return field of the next magnet segment.

The optimization of the muon shield, reported in reference [67], requires knowledge of the flux and spectrum of muons it needs to divert away. Therefore, a simulation

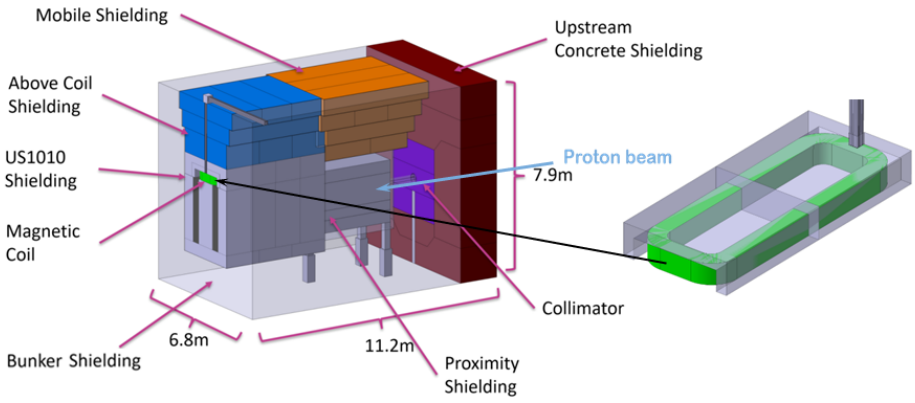

Figure 3.9: Hadron stopper with the coil for its magnetization within the target bunker [57].

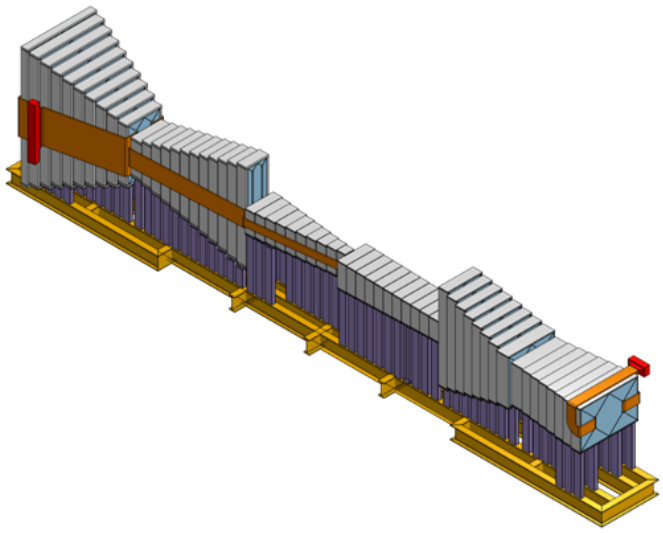

Figure 3.10: Sketch of the free-standing muon shield magnet. In this view, the beam direction is from bottom right to top left. Figure taken from reference [57].

was performed [67] after which the optimization was conducted. The muon momentum distribution estimated from the simulation is shown in figure 3.12. Due to the extremely low-background requirements of the SHiP experiment [50, 55], it was considered necessary to validate the simulation results in an experiment. For this purpose, the measurement of the muon flux and spectrum reported on in this thesis was performed.

3.3.4 Scattering and Neutrino Detector

Directly downstream the magnetic muon shield, the scattering neutrino detector (SND) is situated. The SND includes a heavy target, required to maximize the rate of CC neutrino interactions, and a high resolution target tracker. The neutrino target itself is located inside the SND magnet.

One of its main requirements is the distinction between ν_τ and $\bar{\nu}_\tau$. Since this aim de-

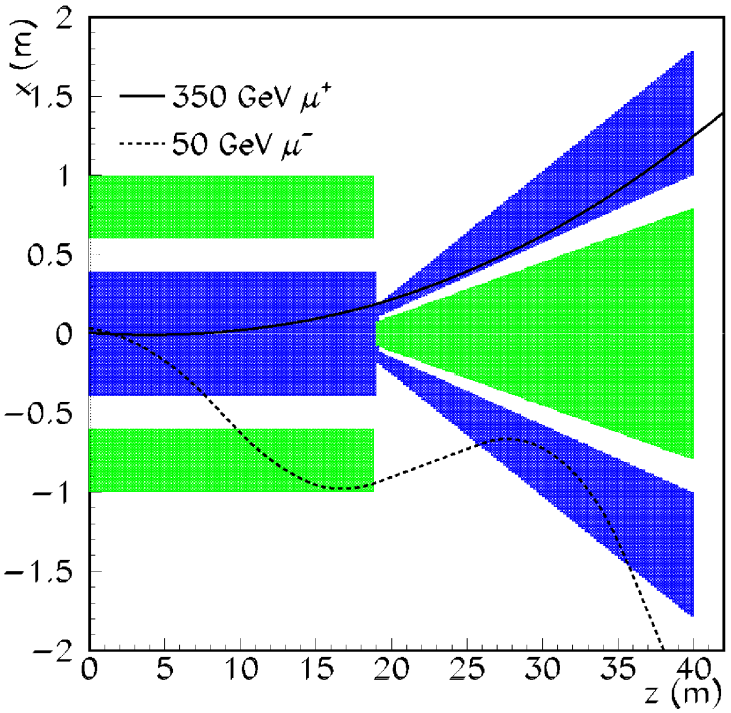

Figure 3.11: Sketch of the working principle of the SHiP active muon shield. This shows a cross section at $y = 0$ with the magnetic field along the y-axis. The blue and green areas show the magnetic field's polarity within the shield's iron yokes. The trajectories of two muons with momenta within the SPS energy range are shown as black lines [67].

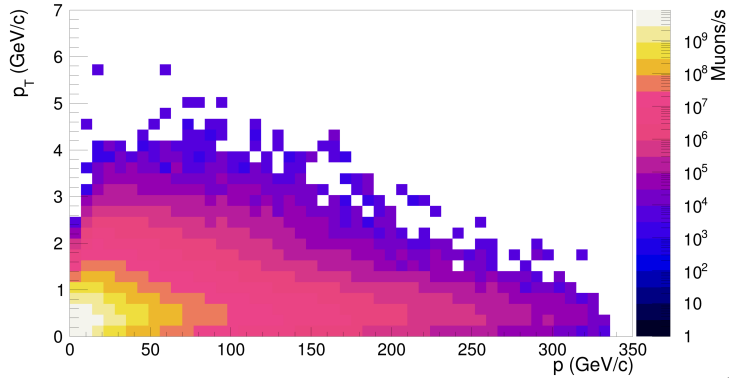

Figure 3.12: Muon flux simulated via Pythia [68, 69] for SHiP. It is shown as the rate of muons per second per bin of transverse momentum p_T (vertical axis) and total momentum p (horizontal axis). This flux is used as a basis for the optimization of the active muon shield [67].

pends on the distinction between the charge signs of the resulting τ leptons, produced in *charged current* (CC) interactions, they must be charge separated in a magnetic field. The decay length of the τ lepton is very short, hence this typically means that it is necessary to determine the charge of its decay daughters. In many cases, the τ decays

hadronic[4], making charge measurement difficult. It requires a spatial resolution allowing the detection of both the production- and the decay-vertex of the τ lepton and an independent charge measurement, of its decay daughters, even if they are hadrons. Due to the short lifetime τ_τ of the τ lepton of $\tau_\tau = (290.3 \pm 0.5) \cdot 10^{-15}\,\mathrm{s}$ corresponding to a decay length of $c\tau = 87.03\,\mu\mathrm{m}$ [21], a very high spatial resolution is required. Additionally, this implies that high density target material and active tracking material need to be placed in a *sandwich*-structure. This way, the short lived τ leptons can be detected while providing enough high density material for neutrinos to interact in. For the high resolution tracking, an emulsion film detector is foreseen, the so-called *Emulsion Cloud Chamber* (ECC). It is based on experience from the OPERA experiment [70], for which the ability to detect production and decay vertices of the tau lepton [71] was shown. To achieve the ability to perform a charge measurement, the target and tracker are situated inside a magnetic field. The tracks curvature is measured in a second type of emulsion detector, the *Compact Emulsion Spectrometer* (CES).

The SND is a hybrid detector consisting of both the ECC and CES, as well as an electronic detector providing timestamps for the events collected in the integrating emulsion films. The ECC and the CES are built from so-called *bricks* with a transverse size of $40 \times 40\,\mathrm{cm}^2$. The ECC bricks consist of 57 planes of emulsion film interleaved by lead plates of 1 mm thickness [56][5]. This equals a material thickness of $\sim 10X_0$. These bricks have a weight of $\sim 100\,\mathrm{kg}$ and a total length of $\sim 8\,\mathrm{cm}$. The target material and emulsion films of an ECC brick are housed inside a metallic box.

A brick of the CES consists of three layers of emulsion film interleaved with a low-density material, an option using air gaps in between the emulsion films is being investigated [56].

From these bricks, a total of 19 walls with transverse sizes of $(80 \times 80)\,\mathrm{cm}^2$ are built of 2×2 bricks of ECC, downstream followed by 2×2 bricks of CES. The composition of one wall is sketched in figure 3.13. Due to the integrating nature of emulsion films and the

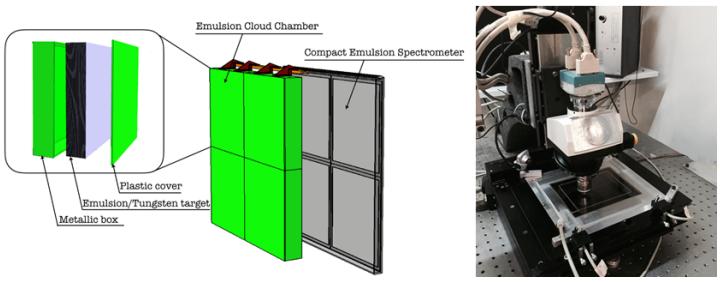

Figure 3.13: ECC brick layout with scanning of nuclear emulsion [57]

fact that many of the decay products of τ leptons cannot escape the SND, timestamps for the events to disentangle them cannot be provided by external detectors. Hence, the walls are interleaved with an electronic detector, able to provide fast timestamps and a tracking

[4]See table 3.3, page 28, for an incomplete list of decay modes.
[5]An option using tungsten instead of lead is also being investigated.

ability. Additional four planes of these electronic detectors will be placed downstream the 19 walls of bricks and target tracker as *downstream tracker.* These measure the charge and momentum of muons escaping the SND target, extending the detectable momentum range of the CES [56]. Figure 3.14 shows a sketch of the all active components of the SND. For the target- and downstream trackers, two technologies are foreseen. These are

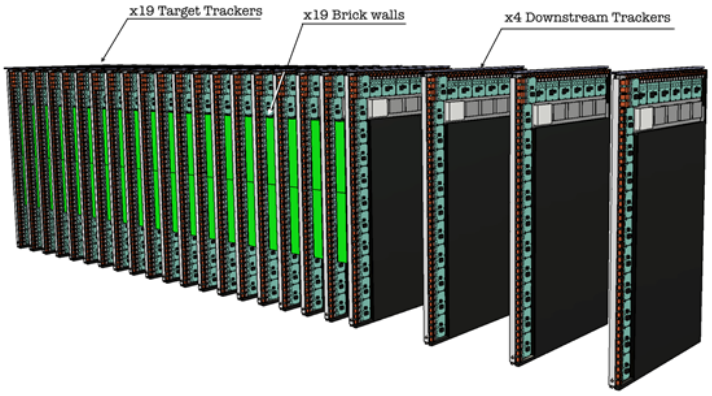

Figure 3.14: SND target tracker [57]

either so-called μ-RWELL, a type of *Micro-Pattern-Gaseous-Detectors* [72] or scintillating fibres (SciFi), developed for the LHCb experiment [56]. Both of these options can provide timestamps with a time resolution of less then 10 ns, efficiency $> 99\,\%$ and a spatial resolution in two dimensions of $\sim 100\,\mu\text{m}$ [56]. The total detector mass sums up to ~ 8 tonnes.

Due to the expected high rate of interactions in the SND, the integrating emulsion films need to be exchanged several times during the SHiP experiment runtime. This requirement and the close proximity to the muon shield, and thus the flux of deflected muons, implies constraints on the construction of the SND, especially the SND magnet, which the target described above is situated in.

Due to the close proximity to the muon flux deflected by the muon shield, its dimensions are strictly limited in order not to reach into the flux of muons. An estimation of the muon flux right behind the muon shield is shown in figure 3.15. In order to maximize the yield of CC interactions of neutrinos in the SND, however, it is optimized in size to fit into the clearance of muons downstream the shield. It must be designed in a way such that it has a negligible stray field reaching into the muon flux outside of the magnet to prevent muons from being bent back into the SHiP detector acceptance. Additionally, it must be able to quickly *open* the magnet, which is needed to exchange the emulsion bricks. The magnet provides a field of $\sim 1.2\,\text{T}$, enabling the charge determination of τ lepton decay products. A sketch of the SND target located inside the magnet is shown in figure 3.16. Downstream of the SND magnet with target and tracker, a muon identification system, consisting of *Resistive Plate Chamber* (RPC) detectors is placed. It is built from 13 iron filters, each 10 cm thick interleaved with 12 active RPC planes. The active planes'

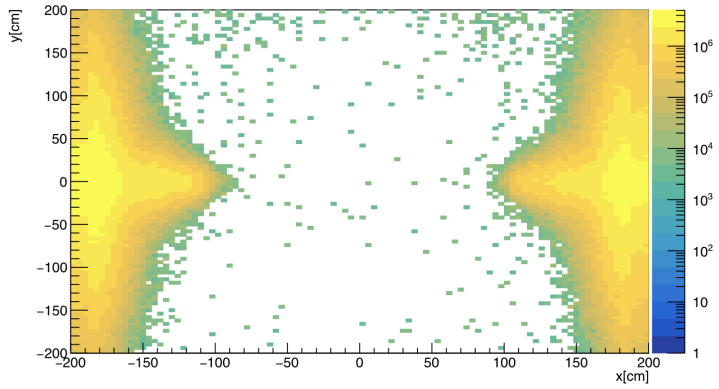

Figure 3.15: Flux of muons right downstream of the muon shield where the SND is starting. The projection is in beam direction, x and y are transverse the beam respectively [56].

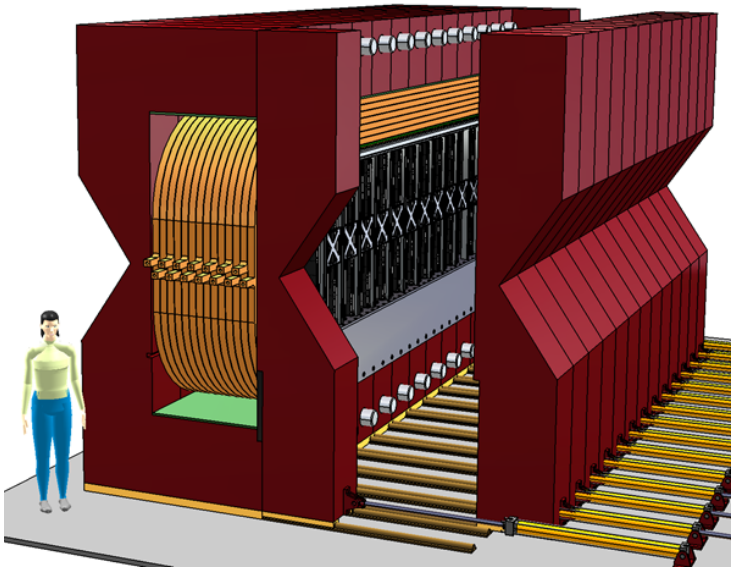

Figure 3.16: Scattering Neutrino Detector (SND). It consists of walls of a heavy target with emulsion tracking, interleaved with electronic trackers. These are situated inside a magnet, which is shaped to fit inside the muon gap downstream the muon shield and maximize the space available for target and tracker material. In this view, the beam direction is from the left foreground to the right background. Figure taken from [57].

transverse dimensions are $(2.5 \times 5)\,\mathrm{m}^2$. The last two planes of RPC detectors will be larger in their transverse dimensions in order to fit the opening window of the SHiP decay vessel. They then also serve to tag muons entering the SHiP decay vessel, which therein are considered background, as some final states, SHiP is looking for have a muon in the final state[6] [56]. A sketch of the muon identification detector is shown in figure 3.17.

[6]See section 3.4 for a brief overview of detection modes of SHiP.

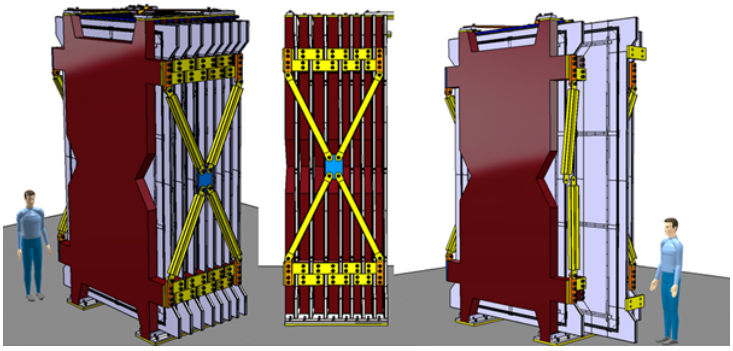

Figure 3.17: RPC muon identification of the SND [57]

3.3.5 Hidden Sector Decay Vessel

The hidden sector decay vessel is a conical shaped steel vessel with a total length of 50 m. A sketch of the decay vessel is shown in figure 3.18. Its shape is dictated by the sur-

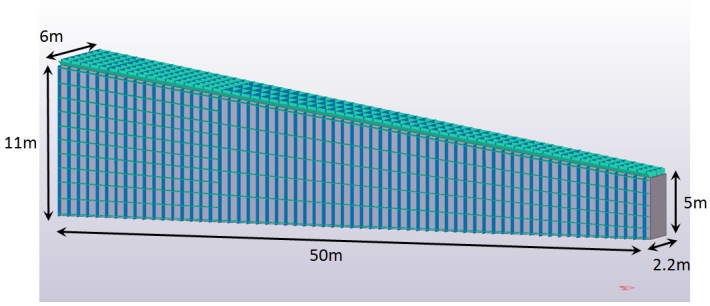

Figure 3.18: Sketch of the hidden sector decay vessel. This steel vessel will be evacuated to minimize background through neutrino CC interactions inside the vessel. The steel vessel will be surrounded by a background tagger from liquid scintillator, which is not shown here. The image was taken from [56].

rounding muon flux which must not hit the steel structure of the decay vessel, potentially bending tracks into the SHiP detector acceptance, hence introducing background[7]. The decay vessel is evacuated in order to prevent background induced by CC neutrino interactions inside the vacuum vessel. However, neutrinos can undergo interactions in the steel structure of the vacuum frame. Therefore, the vessel structure is optimized to be as small in lateral dimensions with as little material budget as possible, while still withstanding the stresses induced by the vacuum inside.

In order to detect particles, mainly muons, either created through neutrino interactions with the vessel material, or entering the vessel from outside, the decay vessel is designed to house a *surrounding background tagger* (SBT). For the SBT, the current baseline option is to surround the decay vessel with a liquid scintillator detector[56].

In its downstream section, the decay vessel houses the subdetectors of the *Hidden Sector*

[7]See section 3.4 for details.

Detector, outlined in the following section. This introduces new challenges since openings for service or detector assembly to the steel vessel will be required, which needs to be considered for the vessel's ability to withstand mechanical stress.

3.3.6 Hidden Sector Detector

The hidden sector detector consists of four major parts: A spectrometer, an electromagnetic calorimeter, a timing detector and a muon identification system[8].

Spectrometer Straw Tracker The spectrometer for the hidden sector detector is planned to be built from four stations of straw tubes, with two stations upstream- and two stations downstream of the spectrometer magnet. Within each station, the straw tubes are oriented with a stereo angle in order to allow three dimensional track reconstruction. This *Spectrometer Straw Tracker* (SST) needs to fulfill two tasks. First it's the measurement of momenta of charged particles originating from HS particle decays to SM particles, second it's the precise reconstruction of their vertices. Here it is a crucial ability to be able to find a vertex within the HS decay volume and momenta pointing back to the proton target. The SST covers the whole cross section area of the HS decay volume close to its end, which equals to an area of approximately $10 \times 5\,\mathrm{m}^2$. Determined by the lateral size of the decay vessel, for momentum reconstruction the magnetic field of the spectrometer magnet needs to be oriented such that the particle trajectories are bent within the $z-y-$plane[9]. This implies the need to have horizontally oriented straw tubes of $\sim 5\,\mathrm{m}$ length, which is yet unprecedented. Due to the fragile nature of straw tubes and tensioning needed to overcome gravitational sagging, this implies major mechanical challenges. Several mechanical solutions have been proposed, however, it is not yet decided which one will be implemented. Among these are a system for mechanical re-tensioning [73], an option to suspend a set of straw tubes with a stiff fiber [74] and the possibility to glue straw tubes together, resulting in a self-stiffening effect when the straws are pressurized as shown for the straw tracker of the $\bar{\mathrm{P}}$ANDA experiment [75].

Timing Detector The first detector component following the vacuum vessel downstream is the Timing Detector (TD). It covers an area of $5 \times 10\,\mathrm{m}^2$, thus the complete aperture of the vacuum vessel and is located directly downstream the closing wall of the vacuum vessel. Two options for the detector technology are investigated. The current baseline option is a setup from plastic scintillator bars, read out by arrays of *Silicon photomultipliers* (SiPM) on both ends of each bar [57]. Another option is the use of a *time measuring resistive plate chamber* (tRPC) [57].

[8] Here, the SBT is left out as it was already mentioned with the decay vessel. However, the SBT can be defined part of the hidden sector detector as well.

[9] Reference figure 3.1, which includes a depiction of the coordinate system used here.

The TD serves two main purposes; first it provides an unambiguous time stamp for events that also provides a reference time for the drift time measurement of the straw tubes in the SST. Secondly, with a required time resolution of 100 ps, it enables the reduction of background through random coincidences of muons entering the HS detector acceptance[10] [57].

Electromagnetic Calorimeter The energy measurement for the SHiP experiment is performed only by an electromagnetic calorimeter, the SplitCal [76]. It consists of alternating planes of lead absorber material and scintillator material. Each lead plane has a depth of $0.5\,X_0$ which corresponds to a thickness of 0.28 cm [76]. The coarsely segmented scintillator planes consist of 1 cm wide strips [57]. In order to measure the shower profile, three additional high precision layers are foreseen. These high precision layers will be placed after the first $3\,X_0$ and two additional layers at the shower maximum. On layer will be at the expected depth of low energy showers, another one at the maximum for high energy showers. For their exact placement, studies are currently performed. The high precision shower profile measurement at two different depths provides pointing capability of the SplitCal.

After the first three X_0, the SplitCal has a mechanical gap of $\sim$ 1 m followed by the remaining calorimeter depth. This increases the calorimeters pointing ability through an increased lever arm. Additionally, it can improve the ability to distinguish between electrons and hadrons [57]. A sketch showing a longitudinal cut of the SplitCal's downstream segment is shown in figure 3.19. For the high precision layers it is foreseen to use the Mi-

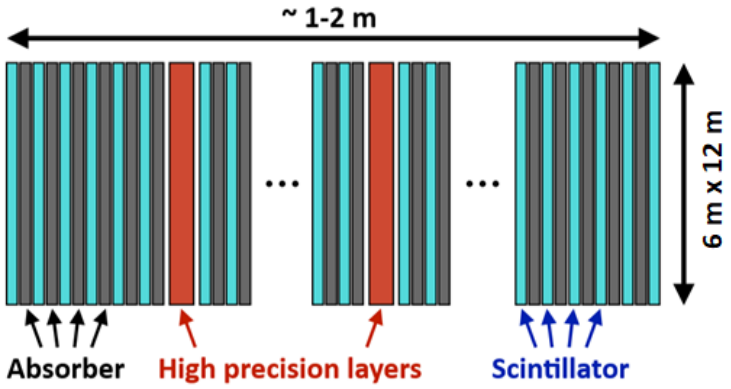

Figure 3.19: Sketch of the electromagnetic calorimeter SplitCal layout. Alternating layers of lead and organic scintillator with a total cross-section of $12 \times 6\,m^2$ and a total depth of $\sim$ $20\,X_0$ [57]. The calorimeter will be longitudinally segmented with $\sim$ 1 m space in between for better pointing accuracy. At the beginning and the expected shower maximum in the SplitCal, additional high precision layers with MicroMegas technology are placed to measure the transverse shower profile. Figure taken from [57].

[10] More info on backgrounds in section 3.4.

croMegas technology, similar to the chambers developed for the upgraded muon system of the ATLAS detector [77] but smaller in size with a cross-section of $80 \times 80\,\mathrm{cm}^2$ [57].

Using the SplitCal's ability to measure the direction of photon showers, the invariant mass of ALPs can be measured, when they decay into two photons [76].

Muon Identification The most downstream part of the SHiP HS detector is the muon identification system. It must be able to identify muons with an efficiency $> 95\%$ in a momentum range from 5 to 100 GeV/c [56]. Furthermore, due to the lack of a hadronic calorimeter, it helps in particle identification through distinguishing between muons and hadrons. The muon system consists of four active stations interleaved with three iron muon filters, each of 60 cm length. This filter material corresponds to $6.7\,\lambda_I$. For the active material, scintillating tiles read out by SiPMs are foreseen. Using this technology, a time resolution below one nanosecond can be achieved [56]. Hence, the background due to random muon coincidences can be reduced by requiring stringent coincidence constraints for two muons.

3.4 Detection Modes and Sensitivities

3.4.1 Heavy Neutral Leptons

As shown in chapter 2.5.3, HNL can mix with standard model neutrinos via a mixing matrix U. This matrix contains elements describing the mixing of HNL state N_i with an active neutrino of flavor α, effectively containing the Yukawa couplings $F_{\alpha I}$ from equation (2.16) [34]. The HNL interactions are suppressed compared to the active neutrinos by the mixing angles $U_\alpha \ll 1$ for $\alpha = (e, \mu, \tau)$ [56].

Through their mixing with active neutrinos, they can be produced instead of an active neutrino suppressed by some amount compared to the active one. Examples of the production and decay of an HNL N are shown as Feynman diagrams in figure 3.20. While in principle, any ratio between the matrix elements of the HNL's mixing matrix U can be assumed, here only a model with the assumption of a dominating mixing to muon neutrinos is presented, thus $U_e^2 : U_\mu^2 : U_\tau^2 = 0 : 1 : 0$ [56].

Even though an HNL has several decay modes which are expressed in more detail in [78], a few channels are dominant. Their branching ratios are shown in figure 3.21. Using the branching ratios of the HNL now SHiP's sensitivity to the HNL according to the model described above can be calculated. A sensitivity plot is shown in figure 3.22. For a more complete overview, including different assumptions about the ratio of the mixing matrix parameters, see e.g [56].

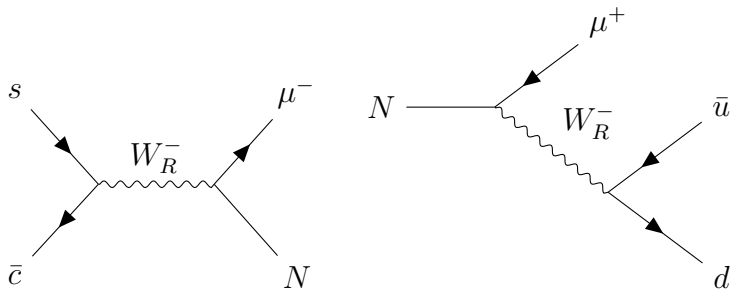

(a) production (b) decay

Figure 3.20: Example of production (3.20(a)) and decay (3.20(b)) of HNLs at the SHiP experiment. The final state can contain a pion and a muon as an example. Diagrams recreated from [55].

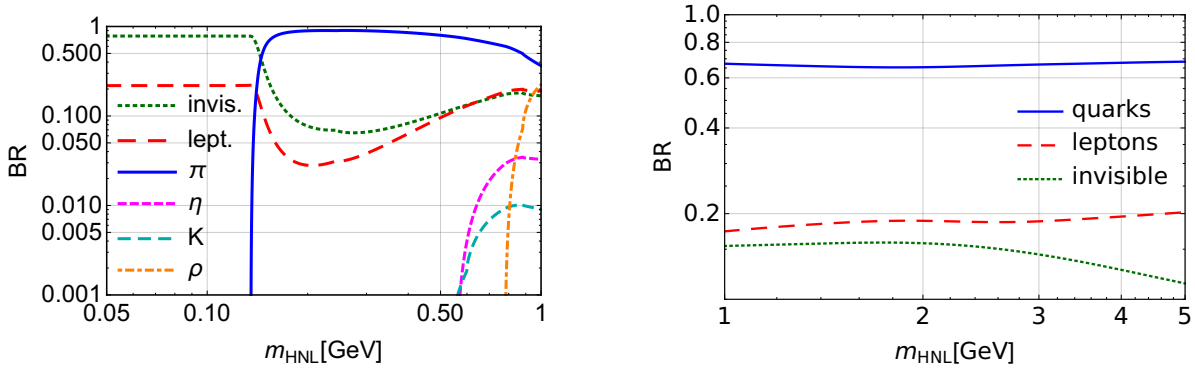

(a) HNL mass below 1 GeV/c^2 (b) HNL mass above 1 GeV/c^2

Figure 3.21: Branching ratios of HNL decays for the most dominant channels. Figure from [78].

3.4.2 Dark Photon

Dark photons can mix with SM photons through the vector portal (see section 2.5). Therefore, they can decay through a coupling either to neutral mesons or a lepton-pair. Using a numerical simulation explained in [56], the branching ratios of the dark photons' decay channels have been calculated. These are shown in figure 3.23. In case of a decay into a lepton pair, the signature is an isolated vertex within the decay volume, with two, opposite charged lepton tracks emerging from it, pointing back to the target. For higher masses of the dark photon, its decay daughters might escape the kinematic acceptance of the detector, limiting the sensitivity to the dark photon. On the other hand, the coupling ϵ between the dark photon and the SM photon[11] affects the sensitivity. A sensitivity plot taking this into account is shown in figure 3.24.

[11] See section 2.5.

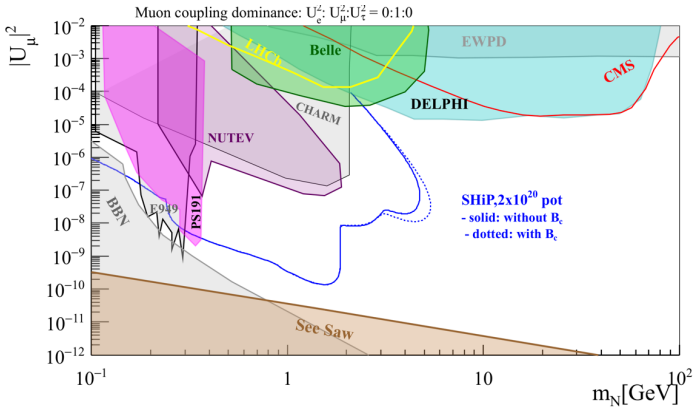

Figure 3.22: SHiP sensitivity to HNLs considering dominance of the coupling to the second generation leptons with a ratio of the matrix elements $U_e^2 : U_\mu^2 : U_\tau^2 = 0 : 1 : 0$. This is the benchmark model for SHiP. The solid and dotted assume either the same fraction of B_c mesons among all beauty mesons as in LHC experiments (dotted) or no contribution by B_c mesons (solid). Their contribution is described in more detail in [56], image is also taken from there.

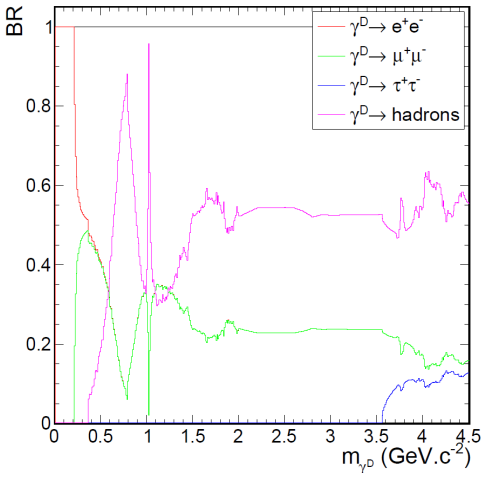

Figure 3.23: Branching ratios of decay channels of the dark photon [56].

3.4.3 Axion Like Particles

ALPs can couple to SM particles via an axion portal described in section 2.3.2. There it was shown that axions and ALPs can couple to photons, fermions or gluons. For SHiP, the benchmark channel is an exclusive coupling to two photons ALP $\to \gamma\gamma$ where it has a unique sensitivity for ALP masses from 200 MeV/c^2 and 1 GeV/c^2 [56]. This sensitivity is achieved through the pointing ability of the SplitCal calorimeter that can reconstruct the invariant mass of the two photons. It is limited through the SplitCals angular resolution [76]. In addition, SHiP's sensitivity for ALPs in case of their coupling to two fermions expands the parameter space in reach compared to earlier experiments [56]. Exclusion plots are shown in figure 3.25. The sensitivity is limited by the SHiP detector's geometrical

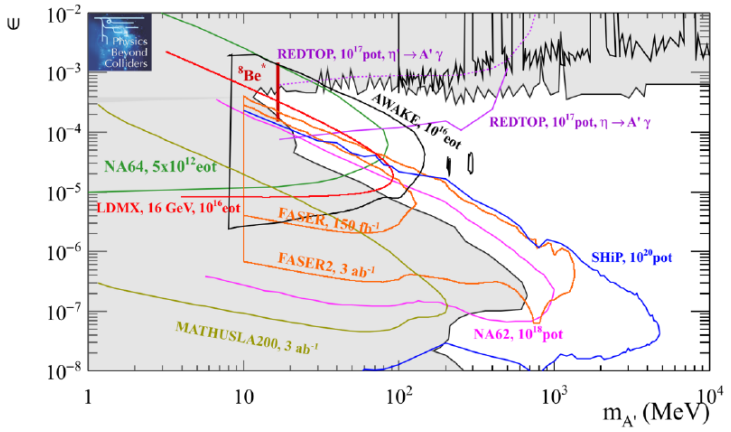

Figure 3.24: SHiP sensitivity to dark photon [34]

acceptance as well as its ability to distinguish two photons from each other in the SplitCal. This is important as the angle between the two photons that the ALP decays to depends on the ALP mass. Therefore, small angles between the photons result in small distances of the two photons to each other when they reach the calorimeter.

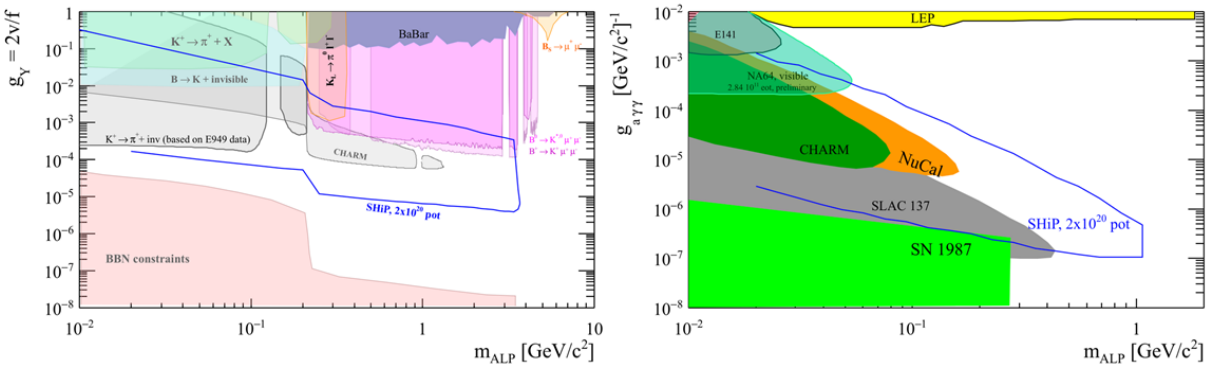

Figure 3.25: SHiP sensitivity to ALP considering their coupling to fermions (left) and photons (right) [57].

3.4.4 Dark Scalar

Dark Scalars can couple to SM particles via the scalar portal (see section 2.5). The coupling of a dark scalar S to the SM Higgs doublet $H^\dagger H$ in equation (2.15) gives rise to Higgs-like interaction of the dark scalar suppressed by a small mixing parameter θ which is [56]

$$\theta = \frac{\mu v}{m_H} \ll 1. \tag{3.2}$$

Here, μ is the coupling constant in equation (2.15), v the Higgs vacuum expectation value and m_H the Higgs mass. Therefore, dark scalars can couple to all massive particles.

Dark scalars can be produced from kaons and B-mesons in flavor-changing transitions

in loops [56, 34]. Considering their production rates in primary proton interactions as well the absorption of kaons in the hadron absorber downstream of the proton target, the sensitivity of SHiP to dark scalars can be calculated. A sensitivity plot in comparison to other experiments is shown in figure 3.26.

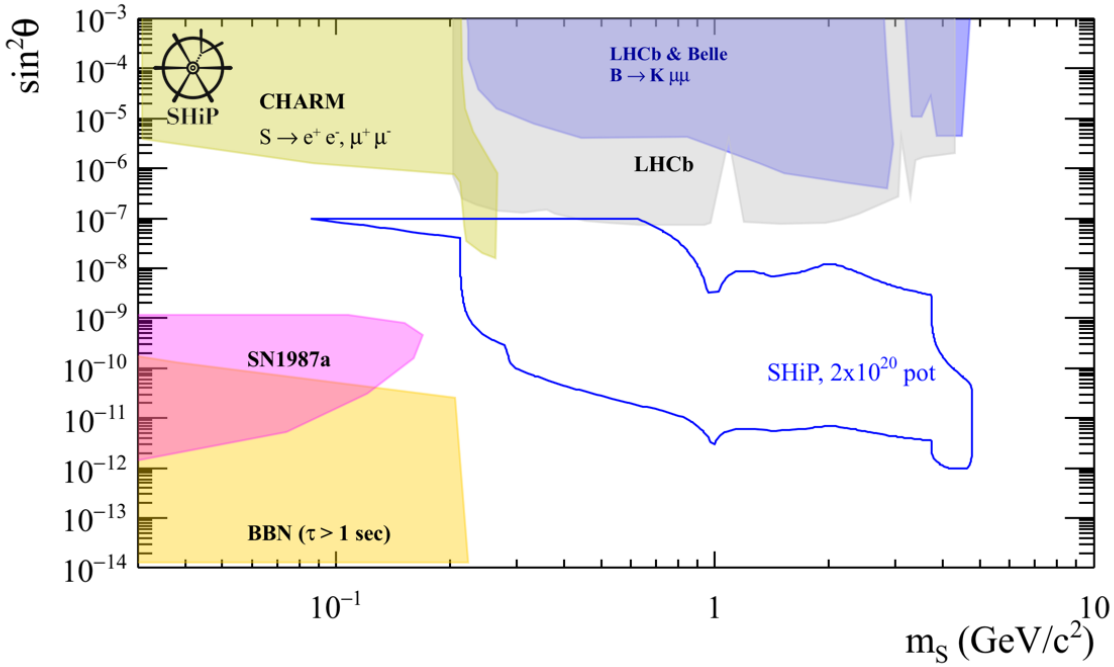

Figure 3.26: SHiP sensitivity to dark scalars. The coupling $\sin^2\theta$ contains the mixing parameter given in equation (3.2). Figure taken from [56].

3.4.5 Background

The SHiP hidden particle searches involve the detection of final states with at least two charged particles and no invisible particles in the final state. Here, the particle tracks are required to originate in a common vertex within the decay volume and their summed momenta should point back to the target. If a reconstructed event fulfills these requirements, it is classified as *fully reconstructed.* In addition, *partially reconstructed* events can be defined, where the final state contains at least one invisible particle [57]. Examples for events that can be fully reconstructed are HNL $\to \mu^\pm\pi^\mp$ or HNL $\to \mu^\pm\rho^\mp(\to \pi^\mp\pi^0(\to \gamma\gamma))$, partially reconstructed events may contain neutrinos in the final state such as HNL $\to \mu^\pm\mu^\mp\nu$ [57]. Note that the $\pi^\pm$ mesons have a decay length of $c\tau \approx 7.8\,\mathrm{m}$ [21]. Considering the relativistic time dilatation, they can reach the spectrometer for pion momenta above $\sim 650\,\mathrm{MeV/c}$ from any position in the decay vessel.

A set of criteria can be defined to select events fulfilling the above mentioned detection signatures. These criteria are shown in table 3.5. The huge muon flux emerging the proton target as well as the large number of neutrinos created alongside them is the main

Table 3.5: Event selection criteria, called *pre-selection*. These cuts select only events with a signature hinting towards a HS particle decay [57].

Requirement	Value
track momentum	$> 1.0\,\mathrm{GeV/c}$
track pair distance of closest approach	$< 1\,\mathrm{cm}$
track pair vertex position	$> 5\,\mathrm{cm}$ from inner wall
impact parameter w.r.t target (fully reconstructed)	$< 10\,\mathrm{cm}$
impact parameter w.r.t target (partially reconstructed)	$< 250\,\mathrm{cm}$

source for background. The background can be grouped into three categories, which are summarized here from [57].

Random muon combinatorial Muons that do not originate in HS decays but in interactions in the primary proton interactions might either survive the muon shield or be scattered elastically back into the decay vessel from the cavern walls. Two of these coinciding within a certain time frame can mimic partially reconstructed events for example. This background can be suppressed by requiring a rather short time frame for a coincidence of 340 ps, which corresponds to > 2.5 times the time resolution of the timing detector. It can be further reduced by using veto information from the background tagger. Another benefit can be gained here through the ability of the SPS accelerator to perform *slow extraction*, delivering a spill of particles over the time of one second, effectively reducing the rate of muons and thus the chance for a random coincidence within a fixed time frame.

Muon inelastic scattering Upstream of the decay vessel, muons might undergo inelastic scattering in the walls and floor of the detector cavern or in detector material. These interactions can create invisible particles entering the decay vessel and mimicking HS decays. These background events can be rejected by applying loose cuts for the event selection shown in table 3.5 and veto information from the background tagger.

Neutrino deep inelastic scattering The dominant contribution to background events are neutrinos undergoing DIS in either in the material of the decay vessel or gas molecules within the decay vessel. To eliminate the latter contribution, a vacuum level below 10^{-2} bar is necessary. Neutrino DIS interactions in the cavern walls and floor have been studied and were found to be negligible. By applying the pre-selection cuts, shown in table 3.5, together with the same timing cut as for the muon combinatorial background as well as veto information, this background can be reduced to < 0.1 events for 2×10^{20} p.o.t. The particles originating in neutrino DIS interactions can also mimic partially reconstructed events. Here an additional cut on the invariant mass can be applied to eliminate this background as well.

Expected background events The number of background events expected after performing a simulation including fully and partially reconstructed events are summarized in table 3.6. It shows that over the whole period of data taking the number of background events from all contributions outlined above is smaller than one, enabling the detection of particles very weakly coupled to SM particles.

Table 3.6: Expected number of background events mimicking HS particle decays for 2×10^{20} p.o.t at 90% CL. These numbers are calculated after applying cuts for background rejection based on event-selection, timing, veto and invariant mass [57].

Background Source	Expected events
Neutrino Background	< 0.1 (fully) / < 0.3 (partially)
Muon inelastic	$< 6 \times 10^{-4}$
Muon combinatorial	4.2×10^{-2}

4 Drift Tube Detectors

Drift tube detectors are gaseous detectors for ionizing radiation. Drift tubes (and drift chambers in general) are a common part of larger integrated particle detectors. They are versatile and well suited to instrument large areas due to their relatively low cost per instrumented volume. Their working principle is presented in this chapter.

4.1 Working Principle

A drift tube is a gas filled, conductive tube with a sense wire spun in its center. Between wire and tube wall, a high voltage is applied such that the wire serves as anode and the tube's wall as cathode.

When a charged particle passes the tube, it ionizes the gas' atoms and molecules along its path. The electron and ion pairs then begin to *drift* along the electric field that originates in the high voltage applied between anode and cathode. For a calculation of the electric field see section 4.1.2. The electrons drift towards the anode, the ions towards the cathode. The electrons, due to their low mass when compared to the ions, are comparatively rapidly accelerated towards the sense wire. There, the electric field is large enough to provide sufficient energy to the electrons so that they can introduce secondary ionization. This leads to an avalanche developing near the sense wire which can be measured as an electric signal. The time the electrons need to drift to the sense wire depends on the distance to the sense wire, they are created at. The electrons produced closest to the sense wire reach it first. The time they need to drift that shortest distance is called the *drift time*. This time is the same from any point on a circle with the same radius, which is called the *drift circle*.

When the time at which the particle passes the tube is known from an external detector *(trigger)*, the time difference to the first electric signal from the drift tube can be measured. From that, the radius within the tube, at which the track has passed the tube can be calculated (see section 4.3). From a time measurement of a single drift tube, only the drift circle can be calculated. Tracking is only possible by combining multiple time measurements from several drift tubes. By fitting algorithms, a track can be found that minimizes the difference between shortest distance to all the sense wires that produced electric signals and the drift circles. Figure 4.1 shows a sketch of the working principle of a single drift tube. An electronically amplified waveform of a drift tube, similar to those used within this thesis, is shown in figure 4.2. Since a drift tube is able to pick up all

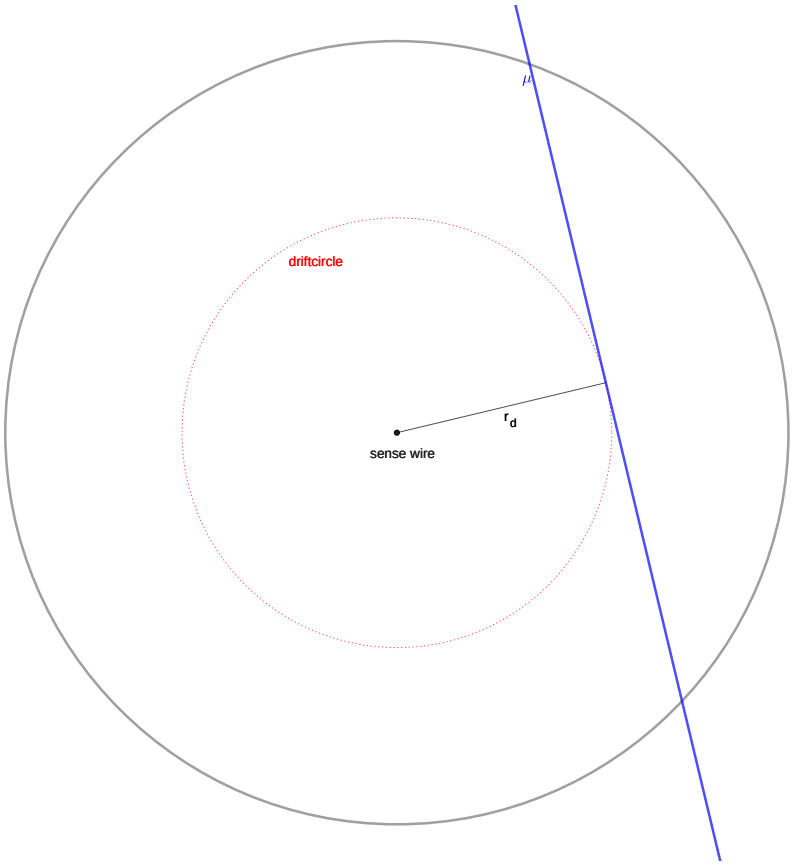

Figure 4.1: Sketch of a single drift tube with a muon track (blue) passing it. Electron and ion pairs are created statistically along the track. The electrons created in ionization processes closest to the signal wire arrive first at the signal wire. The time they need to drift along the drift radius r_d is called the drift time. When the time t_0 at which the muon passes the tube is known from an external detector, by measuring the time difference between t_0 and the first electric signal from within the tube one can calculate the radius from the sense wire at which the track passed the tube.

kinds of electromagnetic noise, it typically produces electric signals with comparatively low amplitude at a high frequency which can be seen in figure 4.2. By introducing a threshold voltage in the signal processing, this noise can be rejected unseen. Ionizing particles passing the tube usually result in electric signals with higher amplitude, hence are not rejected if a suitable threshold voltage was chosen. By utilizing an appropriate set of readout electronics, such as a *time to digital converter (TDC)* for signal readout, it is possible to only store the time difference between trigger (t_0) and the first signal surpassing the threshold voltage, which is then the drift time. Note that by introducing a threshold voltage, either *small* signals corresponding to particles passing the tube might be rejected or larger voltage pulses corresponding to noise might be misinterpreted as signal, resulting in wrong drift time measurements. Both these errors can be minimized by setting an appropriate threshold, the process of finding this, however, is not presented within the context of this thesis.

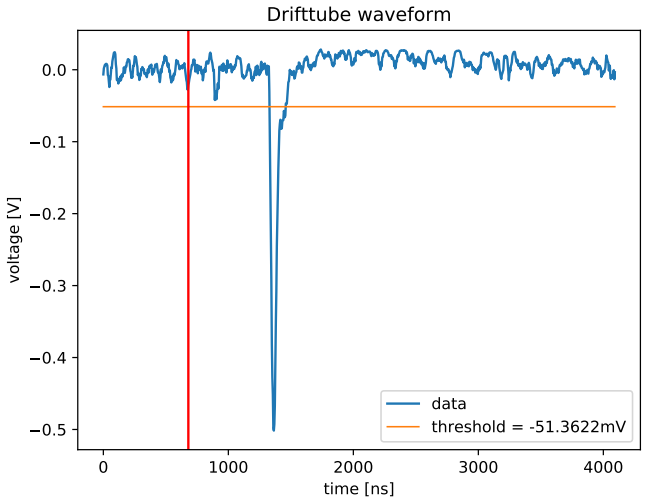

Figure 4.2: Example of a waveform from a drift tube recorded with a FADC. The waveform is recorded using a drift tube, similar to those used for this thesis. It is electronically amplified using the same amplifier as for the spectrometer described later. The vertical, red line represents the time at which the trigger was recorded, the horizontal line shows the *threshold* voltage, which a signal needs to exceed in order not to be rejected as noise.

4.1.1 Ionization and Drift Gases

A charged particle that transverses a material suffers a loss of energe dE per unit length dx. That energy loss is described by the *Bethe-Bloch formula* [79, 80], which is shown in equation (4.1).

$$-\frac{dE}{dx} = \frac{4\pi r_e^2 m_e c^2 N_A Z \rho z^2}{A\beta^2}\left[\ln\left(\frac{2m_e c^2\beta^2}{I(1-\beta^2)}\right) - \beta^2 - \frac{\delta(\beta)}{2}\right] \tag{4.1}$$

In equation (4.1), we use:

$$\begin{aligned}
r_e &\hat{=} \text{ classical electron radius } r_e = 2,8 \cdot 10^{-15} m \\
N_A &\hat{=} \text{ Avogadro number} \\
Z &\hat{=} \text{ Proton number in absorber's nuclei} \\
m_e &\hat{=} \text{ electron mass} \\
\rho &\hat{=} \text{ absorber's density} \\
\beta &\hat{=} \text{ relativistic velocity } \beta = \tfrac{v}{c} \\
A &\hat{=} \text{ absorbers mass number} \\
z &\hat{=} \text{ charge of the ionizing particle} \\
I &\hat{=} \text{ absorber's mean ionization energy [eV]} \\
\delta(\beta) &\hat{=} \text{ density effect shielding the nuclear potential}
\end{aligned}$$

Figure 4.3 shows the energy losses for different particles in air calculated using equation (4.1). Note that the energy loss shows a minimum for all particles except electrons

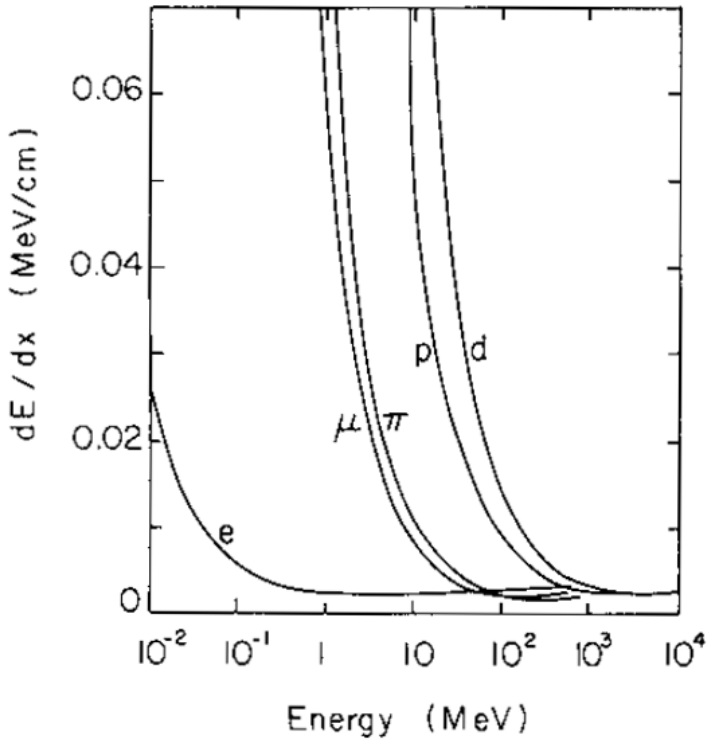

Figure 4.3: Energy loss dE per unit length dx plotted for different particles versus their energy E. The values were computed using equation (4.1) traversing air. At particle momenta above 1 GeV/c, all particles deposit about the same energy per unit length, leading to the so called *minimal ionizing plateau*. Due to the much lower mass of the electrons in comparison to the other shown particles, their energy loss differs as bremsstrahlung has a larger contribution for eletrons [81].

and positrons, where the energy loss per unit length happens to be roughly the same for each particle type. Particles with energies at which their differential energy loss is minimal are called *Minimal Ionizing Particles (MIP)*. The energy at which a particle is minimal ionizing depends on their mass. However, when their energy is expressed in terms of $\beta\gamma = \frac{p}{mc}$, the minimum is at $\beta\gamma \approx 3$ for all particles except electrons. The behaviour of electrons differs from all other particles due to their low mass. For electrons, bremsstrahlung is major contributor to their energy loss.

The detection of particles in drift tube detectors due to the ionization of drift gas atoms and molecules introduces some requirements on the drift gas mixture. Often, drift tubes are used to detect muons, which, on a wide energy range, can be approximated as MIPs. Hence, a requirement on drift gases is a high density of primary ionizations. This can be achieved using a drift gas with a high nuclear charge Z, which can be seen in (4.1). On the other hand, high energy photon interactions are dominated by pair production, whose cross section is proportional to Z^2. Hence, in order to reduce the occupancy when a large

photon flux is expected, lower Z gases are preferable again. Additionally, monoatomic, inert gases have two advantages over other gases. First they offer the maximum number of valence electrons, reducing the mean, effective ionization energy. Second, they have a low cross section for atomic excitations which deexcite via photons instead of being ionized. A common choice here is Argon which offers a suitable compromise between cost and properties as drift gas.

However, if in a drift gas mixture, a state emitting photons is excited, these photons can release electrons from the cathode wall via the photoelectric effect. These electrons then drift to the anode wire again and produces a *late* signal, called afterpulse. The avalanche, however, created by afterpulse electrons can again release photons, repeating this process. Therefore, the admixture of molecular gases is needed that have high cross sections for photon absorption exciting states that deexcite nonradiative in molecular rotation or vibration. These gas additions are called *quenching gases*. A commonly used quencher is CO_2. All measurements presented in the following are performed using a drift gas mixture of Ar:CO_2 in a mixing ratio of 80% to 20%.

4.1.2 $\vec{E}$ field inside the tube

The electric field $\vec{E}$ inside a drift tube can be calculated using Maxwell's equations, in particular Gauss's law, which is shown in its differential form in (4.2). By applying Gauss's theorem, this can be expressed in its integral form as shown in (4.3).

$$\vec{\nabla} \cdot \vec{E} = \frac{1}{\varepsilon\varepsilon_0}\rho \tag{4.2}$$

$$\int_V \left(\vec{\nabla} \cdot \vec{E}\right) dV = \oint_{\partial V} \vec{E} \cdot d\vec{A} \tag{4.3}$$

Here, ρ denotes the space charge density and $\varepsilon_0, \varepsilon$ the permittivity of free space and the material the field expands in. For a cylindrical tube with length z, the surface integral in (4.3) can easily be solved by a coordinate transformation to cylindrical coordinates. Then, the integral can be written as:

$$\oint_{\partial V} \vec{E} \cdot d\vec{A} = \int_0^z \int_0^{2\pi} E(r) r d\varphi dz' = 2\pi E(r) r z \tag{4.4}$$

In (4.4) it was used that the tube's conductive cathode wall is an equipotential surface. Then the condition

$$\vec{E} \parallel d\vec{A}$$

is fulfilled and the scalar product can simply be written as

$$\vec{E}(\vec{r}) \cdot d\vec{A} = E(r) dA = E(r) r d\varphi dz'.$$

On the other hand, the differential form of Gauss's law (4.2) can be solved as:

$$\int_V \left(\vec{\nabla} \cdot \vec{E}\right) dV = \frac{1}{\varepsilon\varepsilon_0} \int_V \rho dV = \frac{q}{\varepsilon\varepsilon_0} \tag{4.5}$$

Thus, by equating the right hand sides of (4.4) and (4.5), one can write:

$$2\pi E(r) r z = \frac{q}{\varepsilon\varepsilon_0} \tag{4.6}$$

Since on a conductive wire, there is a homogeneous charge distribution, we can write:

$$\frac{q}{z} = \frac{dq}{dz} = const$$

By solving (4.6) for $E(r)$ and substituting this, we achieve (4.7).

$$E(r) = \frac{1}{2\pi r \varepsilon\varepsilon_0} \frac{dq}{dz} \tag{4.7}$$

The electric field is a conservative field and originates in a potential difference U_{HV} between the sense wire and the tube's wall. Let a be the outer radius of the sense wire and b the inner radius of the tube, then:

$$U_{\mathrm{HV}} = -\int_a^b \vec{\nabla} U(\vec{r}) d\vec{r} = \int_a^b E(r) dr \tag{4.8}$$

Solving the right hand side of (4.8) results in (4.9).

$$\int_a^b E(r) dr = \int_a^b \frac{1}{2\pi r \varepsilon\varepsilon_0} \frac{dq}{dz} = \frac{1}{2\pi\varepsilon\varepsilon_0} \ln\left(\frac{b}{a}\right) \frac{dq}{dz} \tag{4.9}$$

Now, the right hand side of (4.9) can be equated with the left hand side of (4.8) and then solved for $\frac{dq}{dz}$:

$$\frac{dq}{dz} = \frac{2\pi\varepsilon\varepsilon_0 U_{\mathrm{HV}}}{\ln\left(\frac{b}{a}\right)}.$$

Finally, by substituting this in (4.9), the electric field in the tube turns out to be as shown in (4.10).

$$E(r) = \frac{U_{\mathrm{HV}}}{r \ln\left(\frac{b}{a}\right)} \tag{4.10}$$

4.1.3 Signal Development

The drift of free charge carriers in the electric field within the drift tube leads to an electric signal that can be measured on the anode wire. The signal development can be

explained with a charge q drifting in an electric field $\vec{E}(\vec{r})$ from any point $\vec{r}_1$ to $\vec{r}_2$. On its path it gains an energy $\Delta\varepsilon$ of

$$\Delta\varepsilon = q \int_{r_1}^{r_2} \vec{E}(\vec{r}) d\vec{r} = q(\Phi_2 - \Phi_1) \tag{4.11}$$

where Φ_1 and Φ_2 are the electric potentials at points $\vec{r}_1$ and $\vec{r}_2$ respectively. This energy is taken from the electric field in the drift tube. Since at the anode wire, a constant high voltage is provided, a current flows when charges drift in the electric field,in order to rebuild the electric field. The current can then be measured as an electric signal. Note that the taken energy only depends on the potential difference between the points r_1 and r_2 and only the distance of these points to the anode wire is important due to the conservative nature of electric fields.

In each ionization process, either primary or secondary ionization, both a positive ion and an electron are created and begin to drift along the field in opposite directions. Looking at a pair of electron and ion created at a radius r' within the drift tube, the change of field energy u^- due to an electron and accordingly u^+ due to an ion can be written, using (4.10), as:

$$u^- = -(-e)\alpha \int_{a+r'}^{a} \frac{1}{r} dr = -e\alpha \ln\left(\frac{a+r'}{a}\right) \tag{4.12}$$

$$u^+ = -e\alpha \int_{a+r'}^{b} \frac{1}{r} dr = -e\alpha \ln\left(\frac{b}{a+r'}\right) \tag{4.13}$$

$$u = u^+ + u^- \tag{4.14}$$

with

$$\alpha = \frac{U_{\mathrm{HV}}}{\ln\left(\frac{b}{a}\right)}$$

The total change of electric field energy for a single pair of electron and ion is given by the sum of the contributions from electrons and ions as shown in (4.14).

Note that for cylindrical drift tubes, an avalanche forms near the anode wire. Here, the change of electric field energy is dominated by the drifting ions as shown in (4.13), as they transverse a higher potential difference compared to the electrons [82].

4.1.4 Gas Amplification

The charge carrier avalanche developing in the electric field near the anode wire increases the electric signal[1] as more charge carriers are accelerated using energy from the electric field. This is called the *gas amplification* (or *gas gain*) G, which can be understood

[1] See section 4.1.3.

as a multiplier to the electric signal for the avalanche compared to the original charge, produced in the primary ionization.

The relative change of free electrons $\frac{dN}{N}$ per unit length dr can be described using the *first Townsend coefficient* $\alpha_T(\frac{E}{\rho}, \rho)$ [83]. Note that, for a non-homogeneous electric field, this is a function of the reduced field strength $\frac{E}{\rho}$ and the gas density ρ.

Now, the change of the number of free electrons can is given by equation (4.15).

$$\frac{dN}{N} = \alpha_T \left(\frac{E}{\rho}, \rho \right) dr \tag{4.15}$$

It can be seen that a negative Townsend coefficient would result in a decreasing number of electrons, which prevents an avalanche from developing. This could be the case, if electronegative molecules, such as O_2, are present in the gas mixture in a large enough fraction. These have the ability to bind free electrons in their surrounding. Hence, it must be taken special care to prevent electronegative gases to enter a drift tube.

Using (4.15), the gas gain G can be computed by integrating the relative change of the electron count $\frac{dN}{N}$ along the path of the avalanche:

$$G = \frac{N_f}{N_0} = \exp\left(\int_{r_{\min}}^{a} \alpha_T(r) dr \right) = \exp\left(\int_{E(r_{\min})}^{E(a)} \frac{\alpha_T(E)}{dE/dr} dE \right) \tag{4.16}$$

Here, N_f is the number of free electrons reaching the anode wire, N_0 the number of free electrons originating in the primary ionization, a is the radius of the sense wire and $r_{\min}$ the radius within the tube, where the avalanche begins to develop.

Using the electric field in a cylindrical drift tube from (4.10), the integral can be written as shown in (4.17)

$$G = \exp\left(\frac{U_{\mathrm{HV}}}{\ln(\frac{b}{a})} \int_{E(r_{\min})}^{E(a)} \frac{\alpha_T(E)}{E^2} dE \right) \tag{4.17}$$

The Townsend coefficient is not analytically derivable, hence needs to be measured for any gas and electric field. In 1956, *Diethorn* proposed a parametrization of the Townsend coefficient [84], which assumes a linear dependence of $\alpha_T(E)$. Using this, the path integral can be solved:

$$\ln(G) = \frac{\Delta\Phi}{\Delta V} \ln(2) = \frac{\ln(2)}{\Delta V} \frac{U_{\mathrm{HV}}}{\ln(b/a)} \ln\left(\frac{E(a)}{E(r_{\min})} \right) \tag{4.18}$$

Here, $\Delta\Phi$ is the potential difference, the avalanche passes through from the point of its development to the sense wire and ΔV is the potential difference, a single electron needs to be accelerated with before being able to introduce a secondary ionization itself. The factor $\ln(2)$ originates in the assumption that after the avalanche passes a potential difference ΔV, the number of electrons doubles. Thus, the number of free electrons N_f

reaching the anode wire is:

$$N_f = N_0 \cdot 2^n, n = \frac{\Delta\Phi}{\Delta V}$$

4.2 Drift Time Spectrum

The time that an electron, created in a primary ionization, needs to drift from the place of its creation to the anode wire cannot be derived analytically. It depends on many factors such as the drift gas' pressure and temperature, the accelerating high voltage or slight displacements of the sense wire from the drift tube's center. Hence, a drift tube detector needs to be calibrated before being used as a tracking device.

This calibration could be done using a beam of charged particles that is aimed at certain radii of a drift tube and for each drift radius, the time between the particle passing and the arriving of the electric signal is analyzed. Another method is the use of the so called *drift time spectrum*. Here, a homogeneous irradiation of each drift tube is assumed and for a number of particles, passing the tube, the drift times are recorded. Within the context of this thesis, the latter method is used.

When the drift times for a number of particle tracks passing a drift tube are measured and gathered in a histogram, this is called the *drift time spectrum*. It contains the number dN of drift times that were measured in the time intervals $[t, t + dt]$. The drift time spectrum differs in shape with different drift gas mixtures and drift tube geometries. For a given set of parameters[2], a drift tube is operated with, the drift time spectrum shows a distinct shape. In case of a homogeneous distribution of particle tracks passing the tube, hence $\frac{dN}{dr} = const$, the relation between measured drift time and radius of the drift circle, the rt-relation can be calculated, as shown in section 4.3. Since the drift time for a certain radius depends on many parameters, a large number of drift time measurements is needed in order to achieve a reasonable accuracy of the calibration. For high rate experiments, a sufficiently large particle flux can be present to allow a regular calibration of individual drift tubes. For lower rate experiments, the drift time measurements for a set of drift tubes can be combined and a shared drift time spectrum for this set can be acquired. If the operating parameters of a drift tube detector, such as gas pressure or high voltage change, a new drift time spectrum needs to be created. An example of a drift time spectrum, which is characteristic for the drift gas mixture used at the measurement described in this thesis, is shown in figure 4.4.

4.3 rt-relation

The relation between the drift radius r and the drift time t is called the rt-relation. The function $r(t)$, which computes the drift radius for a given drift time measurement, can be

[2]Such as gas mixture, pressure, ambient temperature, high voltage, ...

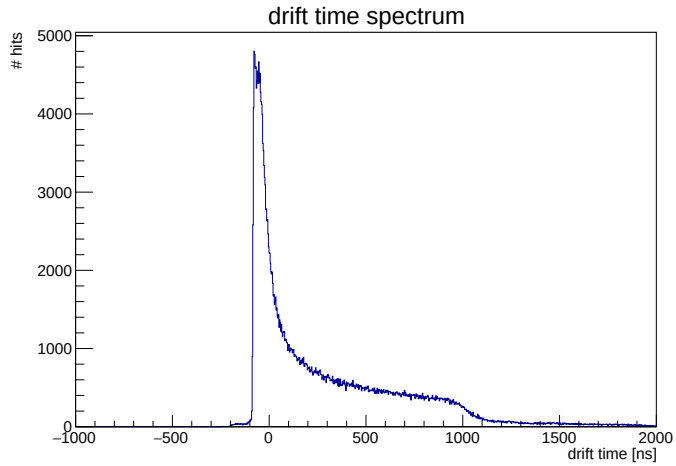

Figure 4.4: Example plot of a drift time spectrum. This drift time spectrum was recorded with the setup used at the muon flux measurement at the SPS described in this thesis. The spectrum shown is a combined spectrum for all drift tubes in the spectrometer for one *spill* of protons on target. Note that the shown drift time spectrum has entries with times < 0. The shortest possible drift time, however, is 0. The systematic shift in the shown spectrum is due to delays of the trigger signal, for example originating in signal propagation time in cables. This shift can be corrected offline. The shape of this drift time spectrum is characteristic for the drift gas mixture of Argon and CO_2 in the mixing ratio 80%:20%, as used here.

obtained by integrating the drift velocity $\frac{dr}{dt}$:

$$r(t) = \int_0^t \frac{dr}{dt'} dt' \tag{4.19}$$

The drift velocity is proportional to the drift time spectrum as shown in (4.20):

$$\frac{dN}{dt} = \frac{dN}{dr} \cdot \frac{dr}{dt} = const \cdot v_d \tag{4.20}$$

Here, the condition of a homogeneous flux of tracks through the drift tube $\frac{dN}{dr} = const$ must be fulfilled. Now, (4.19) can be written as:

$$r(t) = const \int_0^t \frac{dN}{dt'} dt' \tag{4.21}$$

The value of the constant can be calculated using the boundary condition

$$r(t_{\max}) = r_{\text{tube}}$$

Hence, if the drift time spectrum contains N events that were recorded up to a maximum drift time $t_{\max}$ the rt-relation can finally be calculated using equation (4.22).

$$r(t) = \frac{r_{\text{tube}}}{N} \int_0^t \frac{dN}{dt'} dt' \tag{4.22}$$

Note that this method of calculating the rt-relation needs the assumption of a homogeneous detection efficiency of a drift tube along its radius to be made. For a real tube, this is typically not true and they have a lower detection efficiency near the cathode wall since there, the electric field is lower which allows for example a recombination of electrons and ions after the primary ionization. An itererative calculation of a more realistic rt-relation can be performed. The process of *calibrating* the rt-relation as used throughout this thesis is described in [85]. An example plot of a rt-relation is shown in figure 4.5.

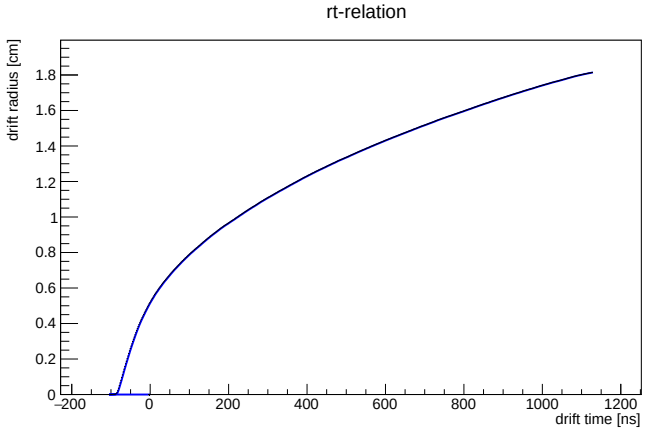

Figure 4.5: Example plot of a rt-relation. Note that it assigns only positive drift radii but (here) starts at negative drift times. The rt-relation is calculated by integrating the drift time spectrum, which is shown in figure 4.4. Due to cable lengths and electronic delays, the drift time might be offset by a constant value. This can be corrected by considering the offset in the rt-relation as shown here. This way, no further correction of the drift time measurement itself is required.

4.4 Spatial Resolution

To determine the spatial resolution of a drift tube detector, a track fitted to several drift tube hits is needed. The track fit finds an optimum track that is a tangent to all the drift circles of the tubes that were hit by this track. An example algorithm for a track fit is presented in chapter 7, hence no further details are given here. After a track fit is performed, the spatial resolution of a drift tube detector can be analyzed. The definition of the spatial resolution used throughout the context of this thesis is the following.

From a fitted track, for each tube that was hit, the shortest distance d between the track and the anode wire of each tube can be calculated. This can be understood as the expected value for a distance measurement of the tube that can be calculated from the measured drift tube using the rt-relation, shown in section 4.3. Now, a *residual* δ can be calculated[3] as

$$\delta = d - r. \tag{4.23}$$

The residuals are distributed Gaussian and centered around zero, assuming the statistical error dominates over the systematic error. Figure 4.6 shows a distribution of the residuals for 10^5 simulated tracks without any systematic errors in the simulation. The distribution can be fitted with a Gaussian probability density function, which is shown in (4.24).

$$\frac{dN}{dr} = a \cdot \exp\left(-\frac{(r-\mu)^2}{2\sigma^2}\right) \tag{4.24}$$

The fit, as well as the fitted parameters, is shown in figure 4.6. The spatial resolution is

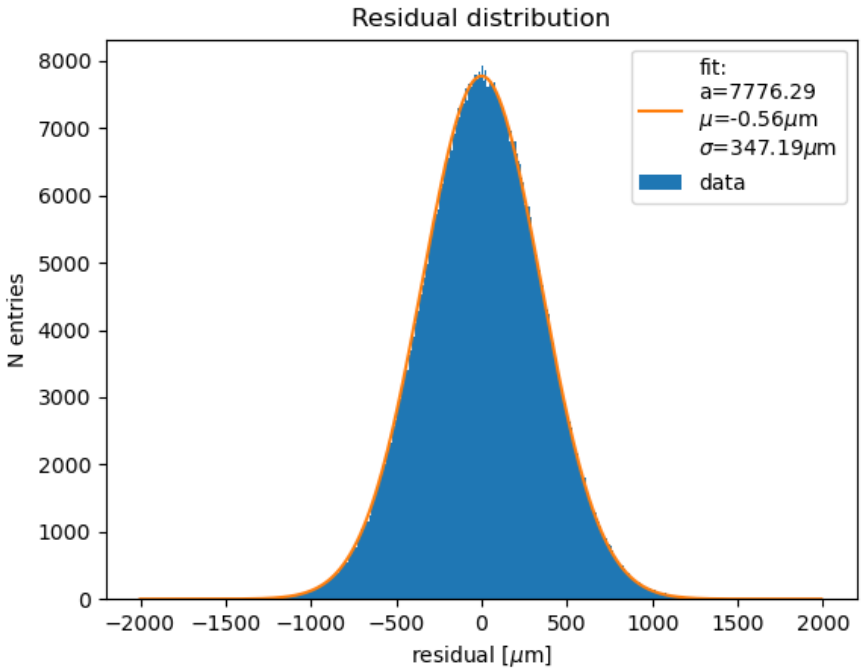

Figure 4.6: Histogram of residuals from fitted tracks. The residuals shown in this histogram are for all hits for 10^5 simulated tracks. The Gaussian fit to the residual distribution is centered around zero and shows a width of $\sigma \approx 350\,\mu\text{m}$, being interpreted as the spatial resolution. This way, spatial resolutions will be calculated in the context of this thesis.

defined as the width σ of the Gaussian fit.

[3]This is simplified to two dimensions, the full definition of a three dimensional residual is presented in chapter 7.2.

Part II

Experiment

5 Measuring the Muon Flux and Spectrum

An experiment was performed measuring the total flux of muons as well as their spectrum emerging from a SHiP target replica at the H4 beam line using protons from the CERN Super Proton Synchrotron (SPS). The experiment and the detector is outlined in this chapter.

5.1 Motivation

At the SHiP experiment, the detection of very weakly interacting particles is foreseen. Therefore, a very low background is necessary. In addition to creating these very weakly interacting, unknown particles, a large number of muons is produced along side them which would, when entering the hidden sector decay volume, result in a large background. In order to deflect the muons away from the decay volume, an active muon shield [67] is foreseen for the SHiP experiment[1]. For the optimization of this muon shield, a simulation of the muon flux from the target is performed. This simulation was based on GEANT4 [86, 87] and Pythia [68]. However, these simulations need validation, which can be achieved with a measurement of the flux and spectrum of muons emerging a target replica offering the same material distribution as the foreseen SHiP target.

Another aspect worth considering when irradiating a heavy target with a high intensity proton beam is radiation protection and environmental safety of the experiment. For this topic, simulations using FLUKA [66, 65] were performed [88] and its results can be validated as well. These simulations can then, when applied to the full SHiP experiment, render a safe operation possible.

5.2 Experiment Overview

The experiment designed for the measurement of the muon flux from the target replica is a typical fixed target experiment, as shown in figure 5.1. The 400 GeV protons from the SPS, after being counted by a set of beam counters, impact the target, which is situated in a massive concrete target bunker. The downstream section of the target

[1] For more information see chapter 3.3.3

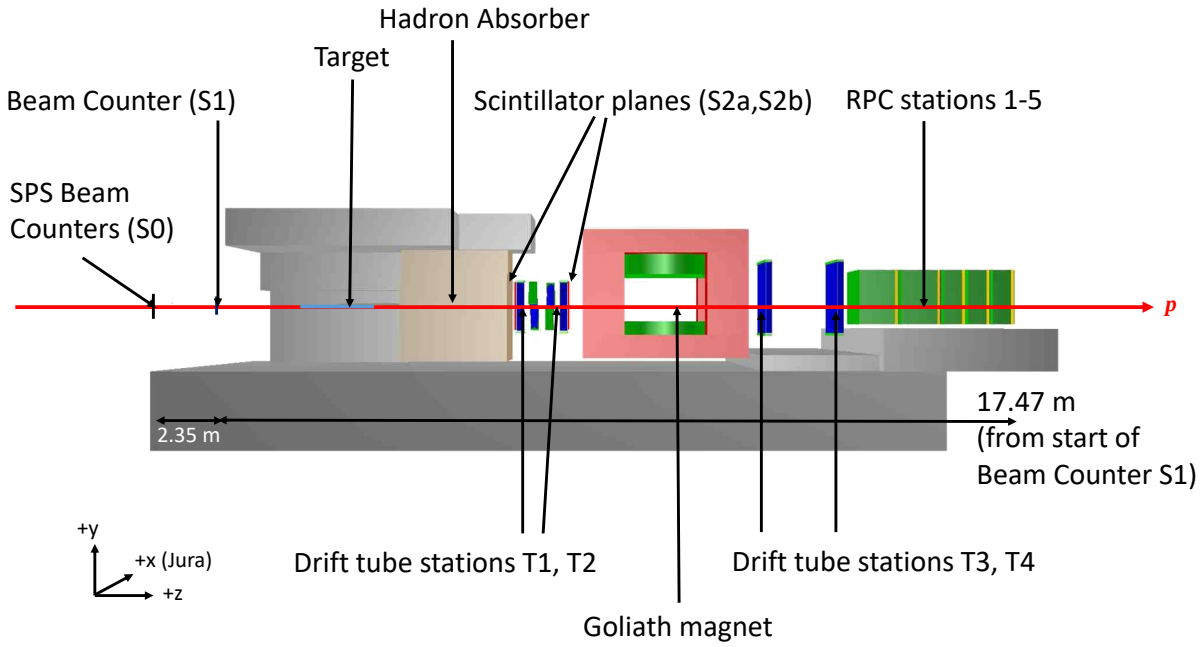

Figure 5.1: Sketch of the detector layout for the muon flux measurement as implemented in FairShip, the SHiP software framework. The proton beam (red, left to right) passes a set of beam counters before hitting the target which is situated in a concrete target bunker for radiation shielding. Downstream the target a massive hadron stopper is placed allowing only muons to pass through. These muons pass the drift tube stations T1 and T2, each of which offering one *module* of drift tubes with a certain stereo angle, allowing a three dimensional track reconstruction. Downstream these drift tubes, the muons pass the magnetic field of the goliath magnet and after being bent by the magnetic field, the tracks pass drift tube stations T3 and T4, followed by five stations of RPC detector [89].

bunker is made of an iron block of $(2.4 \times 2.4 \times 2.4)\,\mathrm{m}^3$ dimensions serving as an absorber for hadrons emerging the target. Its dimensions are designed in order to stop pions and kaons, while not limiting the transverse momentum acceptance too much. Directly downstream the hadron absorber, two *stations* of a drift tube spectrometer are placed. Each of the two upstream stations has one set of drift tubes oriented such that they are sensitive in the x-direction as well as one set of drift tubes rotated with a *stereo angle* in order to have a three dimensional track measurement. Downstream the stations T1 and T2, the Goliath magnet is placed, bending the muon tracks, enabling momentum reconstruction. The magnetic field is dominated by its y-component, thus bending the tracks in the xz-plane only. Therefore, another measurement of the y-component of the tracks' directions downstream the magnet is not considered necessary. Behind the magnet, two more stations of drift tubes are situated. These are oriented such that they are sensitive in the x-direction. The upstream stations and the downstream stations both measure (approximately) straight track segments which are extrapolated to within

Goliath's magnetic field and then matched in its center.

Furthest downstream, five planes of single-gap *resistive plate chambers* (RPC) are located interleaved with thick iron blocks. These provide muon identification and an independent, three dimensional track reconstruction. For the muon flux measurement, the muon identification is not necessary since only muons can pass the hadron absorber following the proton target. However, a second part of the experiment, which is not focused on in this thesis, did not have the hadron absorber in place. Matching tracks measured in the drift tubes with tracks measured in the RPC detector can however be used for example for track selection which is described later.

Proton delivery The protons are delivered in *spills* of 4.8 s duration by the SPS. Per SPS supercycle, there are either one or two spills with intensities between 10^6 and 10^7 protons per spill. A total of 20128 spills were used for analysis, amounting to $2.81 \cdot 10^{11}$ protons on target (p.o.t) as counted by the SC01 beam counter before normalization. In addition, $2.3 \cdot 10^{10}$ p.o.t were recorded without magnetic field in 1445 spills. This magnet off data can be used for alignment of the detector using straight tracks [85]. The recorded proton on target counts must be corrected due to the signal widths of the discriminated signals of the beam counters. The normalization and corrected p.o.t numbers are presented in [85].

5.2.1 Proton target

The proton target irradiated in order to measure the muon flux and spectrum emerging from it closely resembles the foreseen SHiP target design. It is a cylindrical target with a diameter of 10 cm and a length of 154.3 cm. Figure 5.2 shows a photo of the target replica before it was transported to the target bunker. When compared to the SHiP target[2], the replica lacks the tantalum cladding but instead is equipped with thicker tungsten and molybdenum slads in order to maintain the same number of hadronic interaction lengths [88, 89]. For mechanical stability, the target is cladded in a steel vessel. Since the beam energy deposited in the target is low compared to SHiP, active cooling of the target is not needed.

5.2.2 Beam Counters

The beam counters have two main tasks. They should provide info about the number of protons on target as well as serve as a part in triggering.

The number of p.o.t expressed here is calculated using a set of multiple detectors used as beam counters. First, as part of the SPS infrastructure, a scintillator plane of $10 \times 10\,\mathrm{cm}^2$ is present, which is read out by a photomultiplier tube (PMT). This first beam counter is

[2]See section 3.3.2.

Figure 5.2: Photography of the proton target before it was transported to the target bunker [56].

designated *S0*. The signal of S0 is discriminated and then counted on a scaler. After that the protons reach another beam counter station *S1*, which consists of two planes of plastic scintillator, each measuring $16 \times 16\,\mathrm{mm}^2$. Each of the scintillators is equipped with two PMTs, whose signals again are discriminated. These signals are passed to time to digital converters (TDCs) and their hit times are measured. In addition, a coincidence of its four PMTs is required and the coincidence is recorded on another scaler. The derivation of the p.o.t count needs to be corrected for dead times, mainly due to signal widths of the descriminator signals [90]. Figure 5.3 shows a photo of the beam counter setup. Another factor that needs to be corrected is due to the difference in size of the SPS beam counter and the S1 beam counter scintillators. Protons furthest from the beam axis of one spill might hit the larger S0 beam counter but not the S1 scintillators. These protons are called *halo protons* [90]. These are particularly interesting since they can hit the target and produce muons there but do not trigger the detector. Therefore, they create a random background of muons.

5.2.3 Trigger

The triggering of the detector is done using a set of plastic scintillators with PMTs attached to them. These are the beam counter scintillators *S1*, as well two scintillator plates, one upstream of drift tube station T1, the other one downstream of drift tube station T2. The scintillators situated next to the drift tubes are called *S2*. This setup can also be seen in figure 5.1. For a description of the setup defining S1 see section 5.2.2. The scintillators of station S2 have a surface area of $55 \times 110\,\mathrm{cm}^2$ and each scintillator is viewed by two PMTs. A muon candidate is identified by a coincidence of two out of the four S2 photo multipliers. The *master trigger* of the detector now is a coincidence of

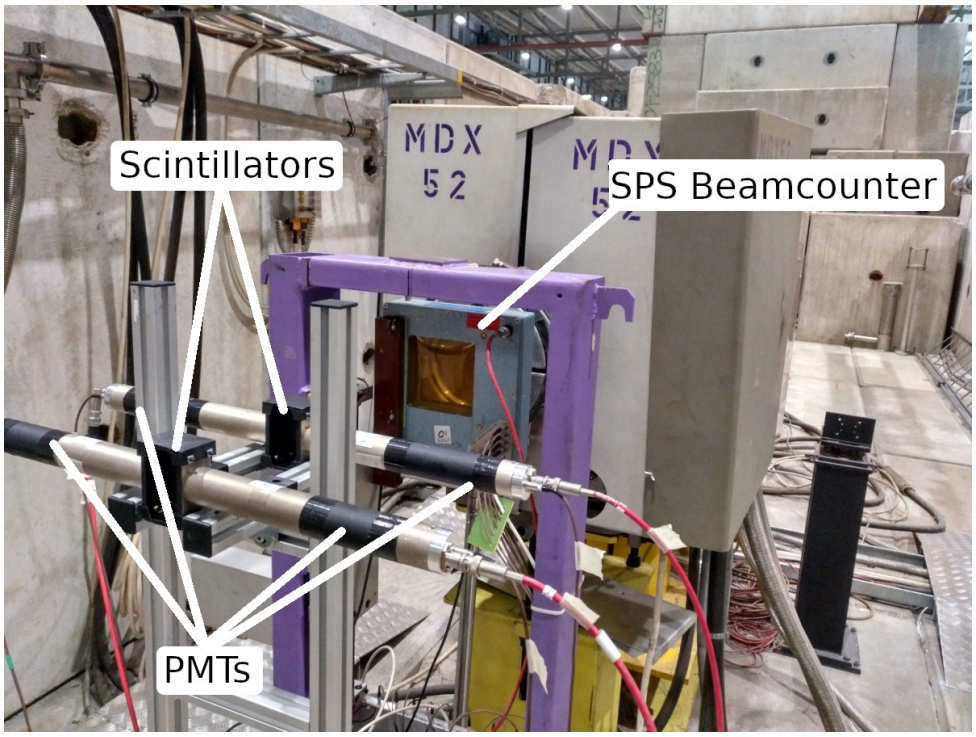

Figure 5.3: Photography of the SPS beam counter S0 as well as the S1 beam counter. The proton beam comes from the background in the image. The protons are then counted by the S0 beam counter first. After exiting on the exit window of a wire chamber measuring the beam shape, the protons propagate to the S1 beam counter station. It consists of two plastic scintillators, each equipped with two PMTs. The S1 beam counter requires a coincidence of the PMTs.

the S1-coincidence and the S2-coincidence, thus requiring a proton on target and a muon emerging the hadron stopper. The scintillators used for triggering as well as their relation to the proton target is shown to scale in figure 5.4. For a more detailed description,

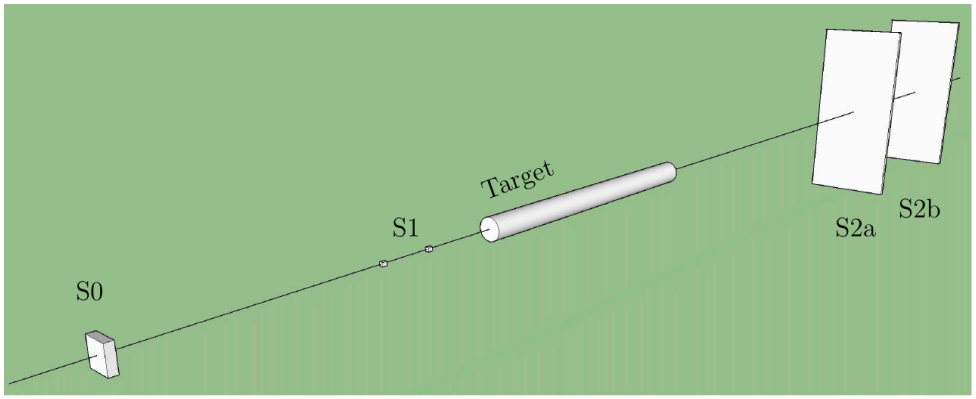

Figure 5.4: Illustration of the scintillators used for triggering in relation to the proton target. S0 denotes the SPS beam counter, the two beam counter scintillators are denoted as S1, S2a and S2b are the scintillators situated around the upstream drift tube stations T1 and T2. Image from [90].

including dead times and digital signal widths, see [90]. A sketch of the trigger logic is shown in figure 5.5.

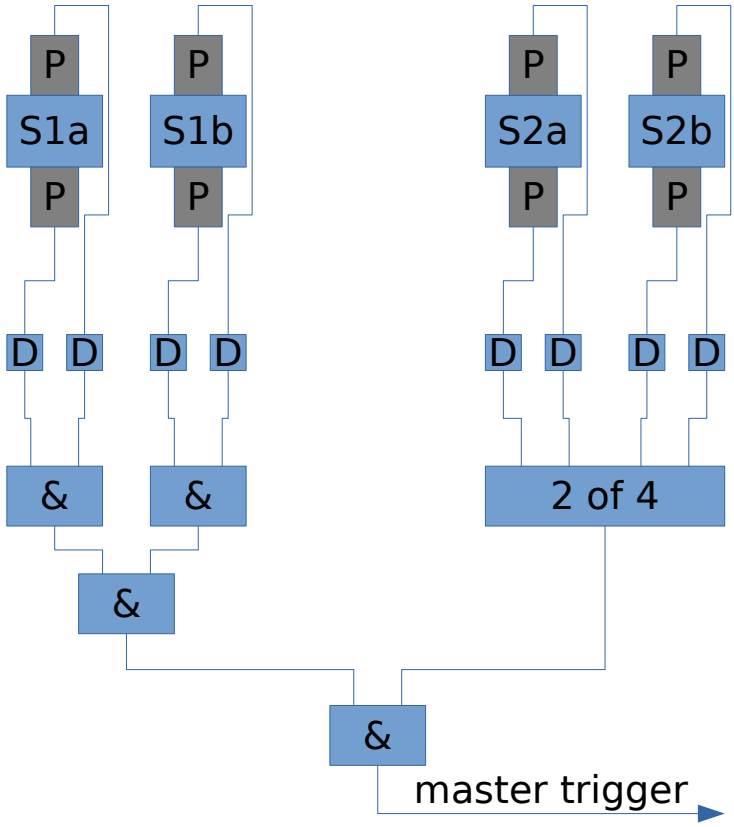

Figure 5.5: Illustration of the trigger logic. This is not to scale and just shows the logic. A letter *P* denotes a PMT, a letter *D* a discriminator. The two scintillators of the beam counter S1 are labeled S1a and S1b, the S2 scintillators accordingly.

5.2.4 Goliath magnet

The Goliath magnet [91] is a warm, dipole spectrometer magnet located at the H4 beamline of the SPS. It has outer dimensions of $4.5\,\mathrm{m} \times 3.6\,\mathrm{m} \times 2.79\,\mathrm{m}$ [91, 92]. The magnet is powered via two power converters called *Goliath* and *David*. Using two coils, the magnetic field is generated. Due different numbers of windings of the upper and lower coil, powering the magnet only with the Goliath power converter's maximum current of $3,600\,\mathrm{A}$, the magnetic field produced would not be homogeneous. Therefore, in order to compensate for this, an additional maximum current of $1750\,\mathrm{A}$ can be supplied via David to the lower coil only. This way, a homogeneous field can be achieved [92].

A recent measurement of the magnetic field using modern equipment was performed [92] including different configurations of the power converters.

During the data acquisition period, three configurations of the magnet were used. These are shown in table 5.1. The measurement of the magnetic field, however does not cover the whole aperture of the Goliath magnet. Therefore, the calculation of the B_y-component

Table 5.1: Field configurations of the Goliath magnet with the according current settings for the Goliath and David power converters that were used for the muon flux and spectrum measurements [85].

Configuration	Goliath current [A]	David current [A]
Nominal	3600	1600
Intermediate	2400	1166
Zero	0	0

was extended using an extrapolation [85] as shown in figure 5.6. At the *nominal* field configuration, the magnetic field measures approximately $B_y = 1.5\,\mathrm{T}$. The intermediate field configuration resulted in a 1.0 T magnetic field and was used for enhanced precision for low momentum muons [56, 85].

5.2.5 Drift tube spectrometer

The drift tube spectrometer is structured into four *stations*, designated T1 through T4 with stations T1 and T2 situated upstream the magnet, T3 and T4 downstream the magnet.

Since the construction, operation and alignment of the drift tube spectrometer was performed as part of this thesis, it is shown in more detail in chapter 6.

5.2.6 Muon tagger

The muon tagger is realized by five planes of single-gap resistive plate chamber (RPC) detectors interleaved with iron slabs for muon filtering. Directly upstream of the first plane of RPCs, a 80 cm thick iron slab is placed. In between the first and second plane, another 80 cm slab is placed and in between the other three planes, slabs with 40 cm thickness are located. The RPC planes themselves have an active area of $190 \times 120\,\mathrm{cm}^2$. The chambers are operatred in avalanche mode and each chamber is read via two panels of x/y-strips with a pitch of 1 cm [89]. Since downstream the proton target, in the experiment described in this chapter, a hadron stopper is located a muon identification is not needed. However, after completing the measurement of the muon flux and spectrum from the SHiP target replica, a second measurement was performed without the the hadron stopper in place. This measurement is outlined in section 5.5.

However, by requiring hits in the most downstream RPC plane and a track reconstructed in the RPC, the lowest energy muons can be filtered out since they cannot traverse the $\sim 2.8\,\mathrm{m}$ of iron.

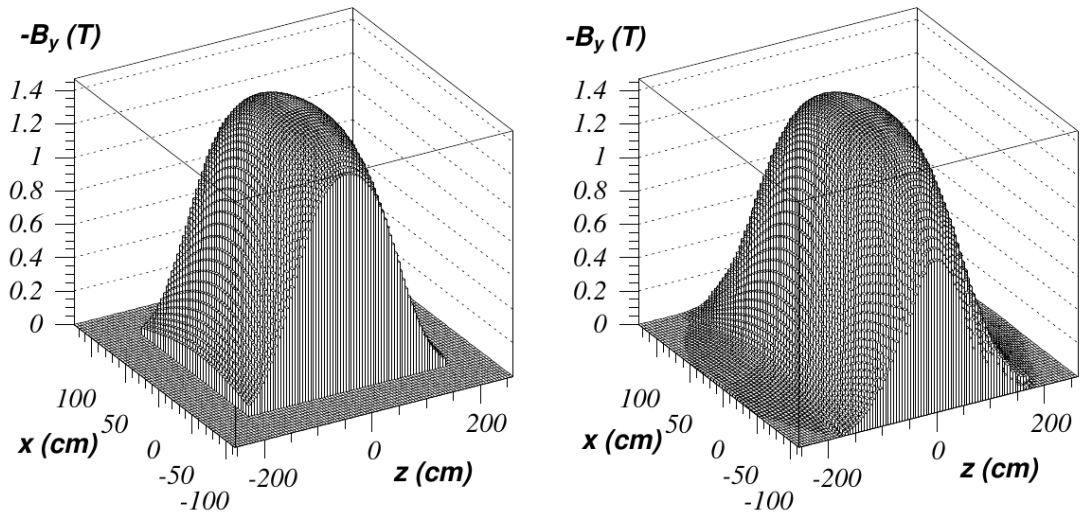

(a) $y = 0$

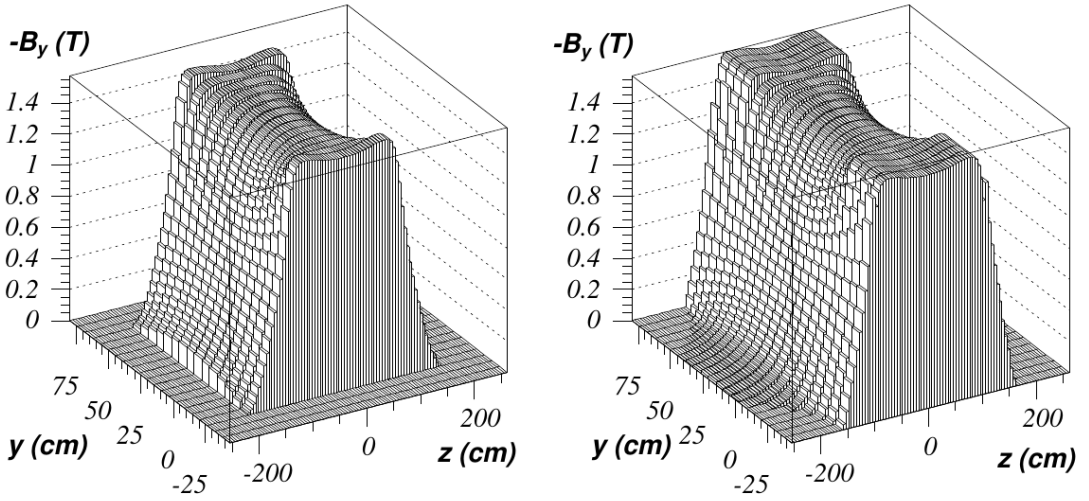

(b) $x = 0$

Figure 5.6: Goliath field map used for track reconstruction. Figure 5.6(a) shows the field strength as a function of x- and z-coordinates at $y = 0$ and figure 5.6(b) as a function of y and z at a fixed $x = 0$. The left hand plots show the measured field values, the right hand plots include extrapolated points that were used in FairShip [85].

5.3 Tracking and Momentum Resolution

The trackfit is performed using an iterative Kalman fitter with annealing from the *GENFIT* software package [93]. It uses the extended measurement of the magnetic field of the Goliath magnet presented in section 5.2.4. The trackfit is performed for the drift tube detectors and the RPCs separately. For muons with momenta larger than 10 GeV, the reconstructed tracks of the drift tubes and the RPCs need to match in order to accept a track for analysis. Lower momentum muons have such high deflection angles in the magnetic field of the Goliath magnet that they typically do not reach the RPC detectors.

Figure 5.7: Photography of the muon tagger as seen from behind. Five planes of RPC detectors are situated between walls of iron filtering for muons [56].

For those low energy muons, the analysis is performed using the drift tube tracks only [85]. An example plot of a track fitted in both the drift tube spectrometer and the RPC detector is shown in figure 5.8. Prior to the track fit, a pattern recognition is performed on the raw detector hits yielding starting values for the fit. The pattern recognition as well as consistency checks performed after the fit are explained in more detail in [85]. In order to determine the momentum resolution of the detector outlined above, a Monte Carlo Simulation was performed and the reconstructed momentum using the same tracking algorithm as for real data was compared to the momentum of the Monte Carlo truth. The resulting momentum resolution is shown in figure 5.9. The initial simulation was performed assuming a drift tube spatial resolution of $\sigma_{DT} = 270\,\mu\text{m}$ that was reported for this drift tube detector type from the OPERA experiment [94]. However, the drift tube resolution achieved in this experiment was only 350 µm [85]. The simulation was repeated with an additional hit smearing and the resulting momentum resolution is included in the plot shown in figure 5.9. The lower resolution compared to the value achieved at the OPERA experiment can be explained by two main factors. At the OPERA experiment, the environment was controlled, hence the ambient temperature and pressure was constant (and monitored), what was not the case for this measurement. However, temperature and pressure can have an impact on the rt-relations of drift tubes. Additionally, the value reported from the OPERA experiment is achieved after applying a software-alignment of the detector, which was not done for the experiment presented here.

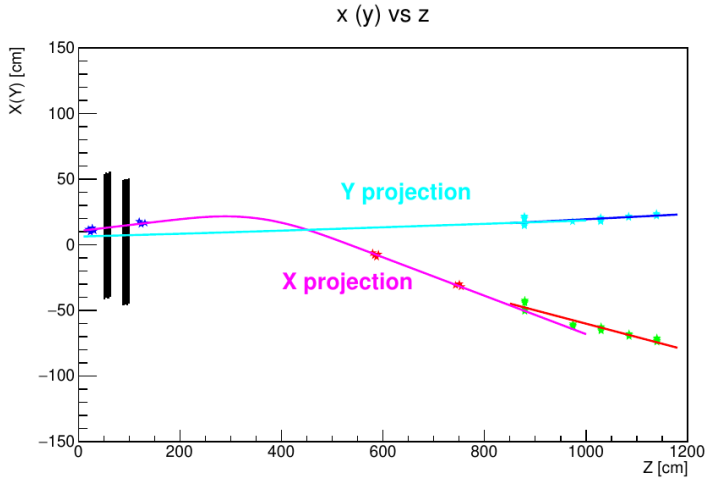

Figure 5.8: Example of a reconstructed muon track both in $x-$ and $y-$ projections. This contains hits in the drift tube spectrometer as well as the RPC stations. The magenta curve represents the x-projection of the track reconstructed in the drift tubes only. The tracks x-projection reconstructed in the RPC stations is shown in red. This shows the curvature of the track within the Goliath magnet. The blue data points are hits of drift tubes in stations T1 and T2. The stereo modules are represented as black lines and their hits are not drawn in this display. The red data points downstream the magnet are drift tube hits in stations T3 and T4. Green data points represent the x-coordinates of RPC hits and the cyan points show their respective y-coordinates [85].

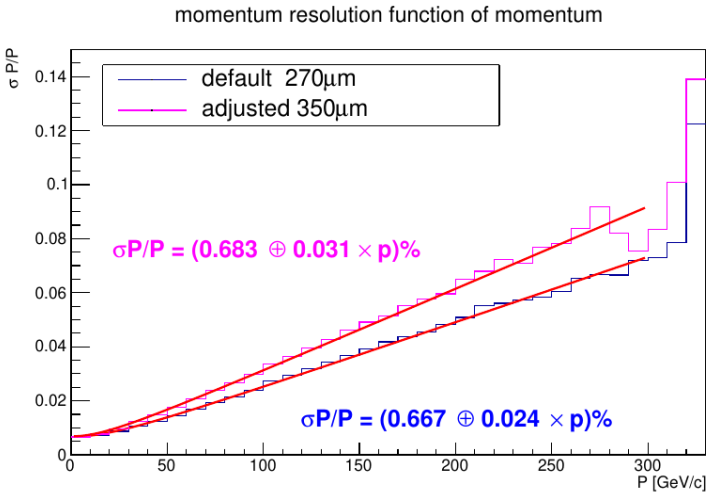

Figure 5.9: Momentum resolution of the spectrometer used to determine the muon flux and spectrum. The momentum resolution was determined using a Monte Carlo simulation of muons reconstructed with two assumed drift tube hit resolutions. For low momenta, the momentum resolution is dominated by multiple scattering effects, hence the hit resolution is negligible. At higher momenta, the momentum resolution is a linear function of the hit resolution [85].

5.4 Result Summary

The recorded dataset was used to check the validity of the physics simulation for the SHiP experiment, as well as the radiological simulation, required for the approval of the SHiP experiment in terms of health- and environmental safety. Therefore, the measured flux of muons was calculated in different momentum bins from the reconstructed tracks and compared with the the muon flux from simulated tracks in that same bin. The result is summarized in table 5.2. Momenta below 5 GeV/c are neglected, since the full-scale SHiP

Table 5.2: Number of reconstructed muon tracks per 10^9 POT per GeV/c, summarizing the results of the muon flux and spectrum measurement. Table adopted from [89]. To check the validity of the physics simulation for the SHiP experiment, the number of tracks reconstructed for real data is compared with the according number from the MC simulation. The ratio between data and simulation is also calculated for several momentum bins. Momenta below 5 GeV/c are neglected since the full-scale SHiP experiment will have a hadron absorber of 5 m thickness, which only muons above 5 GeV/c momentum will be able to exit. The statistical errors are negligible. The uncertainties for real data are dominated by the uncertainty on the POT normalization, while for simulation it is dominated by a different reconstruction efficiency when compared to data [89].

Interval [GeV/c]	data	simulation	ratio
5 - 10	$(1.13 \pm 0.02) \times 10^5$	$(1.12 \pm 0.03) \times 10^5$	1.01 ± 0.04
10 - 25	$(2.40 \pm 0.05) \times 10^4$	$(1.85 \pm 0.06) \times 10^4$	1.29 ± 0.05
25 - 50	$(4.80 \pm 0.10) \times 10^3$	$(3.76 \pm 0.11) \times 10^3$	1.28 ± 0.05
50 - 75	$(9.83 \pm 0.20) \times 10^2$	$(8.00 \pm 0.20) \times 10^2$	1.23 ± 0.05
75 - 100	$(2.95 \pm 0.06) \times 10^2$	$(2.50 \pm 0.08) \times 10^2$	1.20 ± 0.05
100 - 125	$(1.10 \pm 0.02) \times 10^2$	$(0.90 \pm 0.03) \times 10^2$	1.14 ± 0.05
125 - 150	21.0 ± 0.4	20.1 ± 7.5	1.04 ± 0.04
150 - 200	6.4 ± 0.1	6.6 ± 0.3	0.96 ± 0.04
200 - 250	0.76 ± 0.02	0.88 ± 0.06	0.86 ± 0.06
250 - 300	0.26 ± 0.01	0.26 ± 0.03	0.97 ± 0.11

experiment will provide an iron filter downstream of the proton target, which only muons with momenta above 5 GeV/c will be able to exit [89].

The difference between data and simulation is in a reasonable range, considering the complex interactions, resulting in muons released from hadronic collisions. A graphical comparison, highlighting the reasonable agreement between data and simulation is shown in figure 5.10, which also contains a comparison of the transverse momentum distribution for data and simulation. The measured spectrum can be be used to adjust the simulation. This adjusted and validated simulation can then be used to validate the background-studies for the SHiP experiment as well as optimize its muon shield. A possible source of the difference between data and simulation is the different number of muons from kaon and pion decays. It was observed that by increasing the contribution of these particles

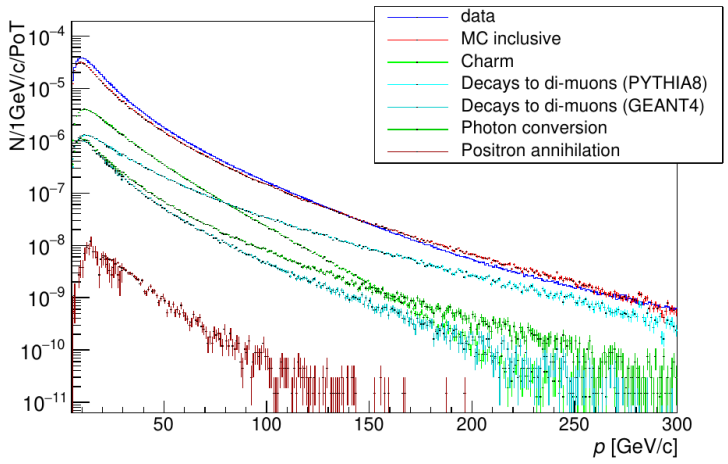

(a) Momentum distribution

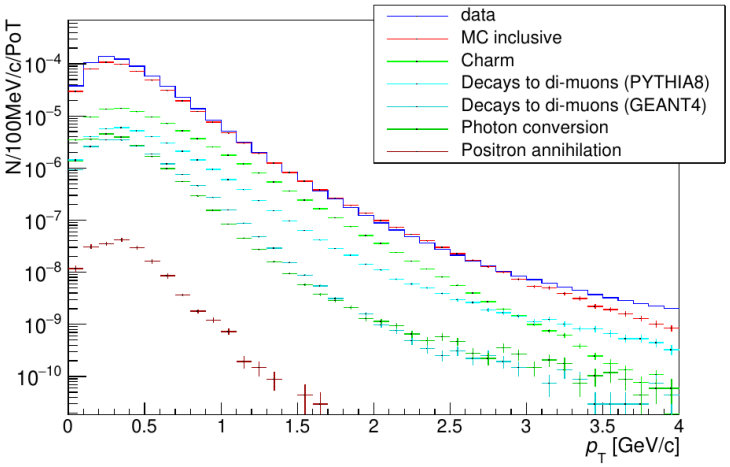

(b) transverse momentum distribution

Figure 5.10: Comparison of the total muon spectrum (a) and muon transverse momentum p_T distribution (b) between data and simulation. The spectra are normalized to the number of POT. The data (shown in blue) shows reasonable agreement with the simulation (red). For the simulation, some contributions to the total spectrum are highlighted, in particular these are muons from charm decays, from decays of low-mass resonances to two muons (computed with two different muon generation toolkits), from photon conversion and positron annihilation. Note the different momentum scales. Images taken from [89].

in the simulation could decrease the discrepancy [89]. For a detailed description of the results and conclusions from the experiment, see [89, 85].

5.5 Charm Cross Section Measurement

The aims of the SHiP experiment include the examinations of tau neutrinos as well as heavy neutral leptons. Both of these particle types originate in decays of charmed

hadrons[3]. These charmed hadrons can be produced either in primary proton interactions or in secondary interactions associated with a hadronic cascade shower [57].

Simulations performed for the SHiP experiment indicate an increase of the charmed hadron yield by a factor 2.3 due to the cascade production [95]. An existing measurement of the associated charm production cross section [96] used a thin target where the cascade production was negligible. Therefore, a measurement of the production cross section for charmed hadrons was proposed using a thick target, thus including cascade production in order to validate the SHiP simulations of charmed hadron production [97]. After the measurements for the muon flux determination were completed, the detector setup was therefore altered for an optimization run for the proposed charm production measurement.

The altered detector layout is illustrated in figure 5.11. Here, instead of the SHiP target

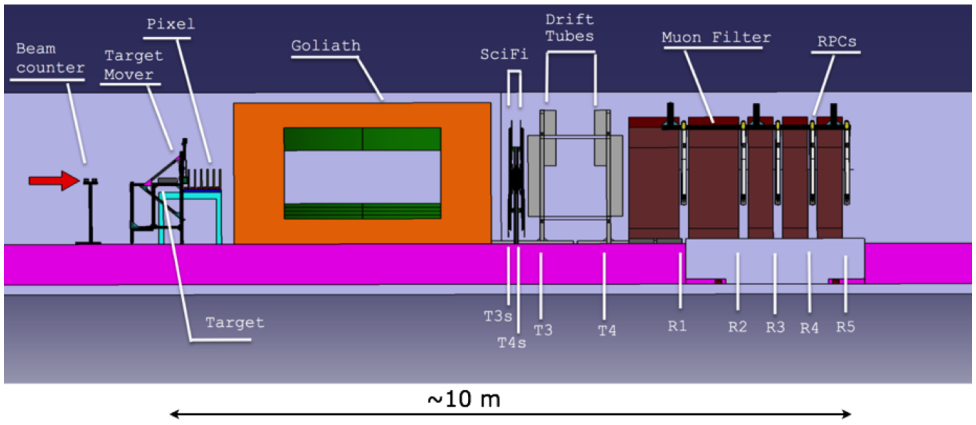

Figure 5.11: Lateral view of the experimental setup used for the charm cross section measurement [56].

replica, bricks with the SHiP target material interleaved with nuclear emulsion films for high precision tracking were hit by the 400 GeV SPS protons. For the event reconstruction in the target bricks, the determination of the charge sign of tau leptons and muons is essential. Therefore, downstream the target bricks, a spectrometer is located. The target bricks, due to the accumulative nature of film exposure, were situated on a moving table, moving the brick on scan lines through the fixed beam spot. In front of the target bricks, additional lead bricks without instrumentation were placed in some measurement runs, in order to enhance the cascade production. Downstream of the target bricks, a silicon pixel detector was placed, still upstream the Goliath magnet. Downstream the magnet, a *scintillating fibre (SciFi)* detector was placed, providing tracking with high granularity near the beam axis.

Due to the lack of a hadron absorber downstream the target bricks and the small targets compared to the SHiP target replica shown before, a significant fraction of the primary protons as well as a number of hadrons escape pass through the detector close to the beam axis. These hadrons would, when passing through the drift tube detector, induce such a

[3]For more info see chapter 3.2.

high occupancy close to the beam axis that the detector would not be able to efficiently track muons anymore, which is needed for the charge sign determination of tau leptons in the target bricks. Downstream the magnet, further off the beam axis, the particle flux was considered small enough to operate low granularity drift tube detectors. The drift tube walls had openings around the beam axis in order to allow the hadrons close to the beam axis to pass in between the drift tubes. Downstream the drift tubes, the RPC muon tagger was situated, operated the same way as described before.

A reconstructed event from a developed and scanned nuclear emulsion brick is shown in figure 5.12. The measurements allowed the development of a tracking software for the

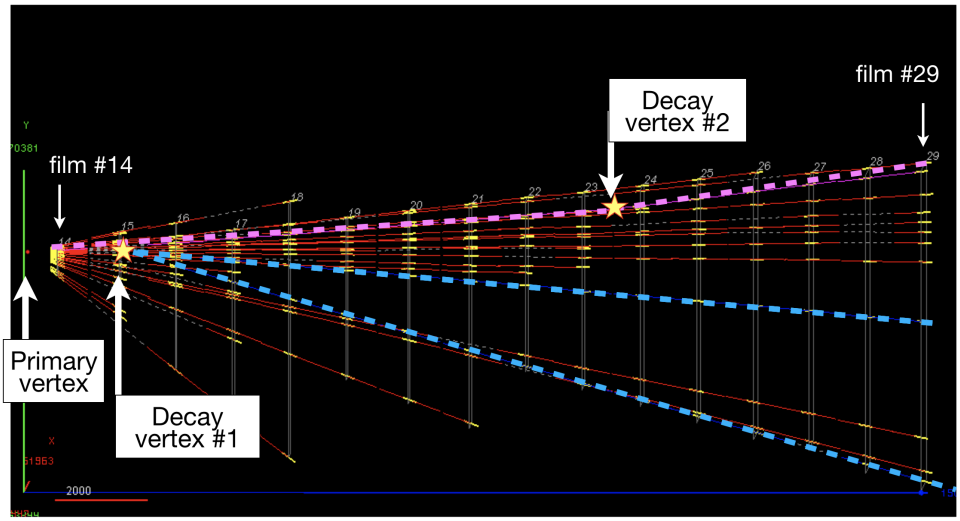

Figure 5.12: Reconstructed charm event from a tungsten target brick. The target material was interleaved with sheets of nuclear emulsion. The event shows a primary vertex and two secondary decay vertices, which are reconstructed candidates for charmed hadrons [57].

scanned emulsion films in a high energy and high intensity environment [57]. This implies tracking challenges such as small kink angles at vertices and particularly densely exposed emulsion films.

While the setup and operation of the drift tube detector for this experiment was also part of the work associated with this thesis, no further focus will be set on this part of the experiment. The results of this measurement are planned for publication. However, by the time of publishing this thesis, they were not yet available.

6 The Drift Tube Spectrometer

The drift tube spectrometer consists of existing as well as newly built detector components. Many parts of the hardware are based of the drift tube spectrometer used at the OPERA experiment [98]. For measurements with a high intensity proton beam such as the SPS beam, the requirements in terms of trigger rate are much higher compared to OPERA, which was a *low rate* experiment. While the trigger rate at OPERA was in the order of some Hz, here a trigger rate on the order of several kHz is expected. Therefore, the use of new TDC boards and the development of completely new software for data acquisition was necessary. This chapter will give an overview of the drift tube spectrometer itself, its electronic readout and the data processing.

The detector-related work performed in the context of this thesis was mainly focused on[1] the following tasks, all of which are explained in more detail in the following:

1. Assembly of new drift tube modules
2. work on the data acquisition software, with a focus on fast data storage, buffering and network interactions
3. parts of the correction of asynchronous clocks
4. setup, commissioning and operation and decommissioning of the detector

6.1 OPERA Drift Tube Modules

The drift tube spectrometer consists of *modules* of 48 drift tubes, sharing the same design as the *precision tracker* of the OPERA experiment [94]. The drift tube spectrometer for the muon flux measurement consists of a total of 576 drift tubes with two different lengths. These are arranged in four stations along the beam axis.

Each drift tube consists of an aluminum tube with an outer diameter of $38^{+0}_{-0.15}$ mm and a wall thickness of 850^{+0}_{-150} µm. In the tube centers, gold-plated tungsten wires with a diameter of 45 µm are spun, which are produced by *California Wire Factory (CWF)*.

The drift tubes are arranged in *modules* of 48 drift tubes each, consisting of four adjacent layers of twelve drift tubes each. Figure 6.1 shows a detailed drawing of such a module. This staggering of the tubes is optimized such that a muon track transversing a drift tube

[1] But not limited to

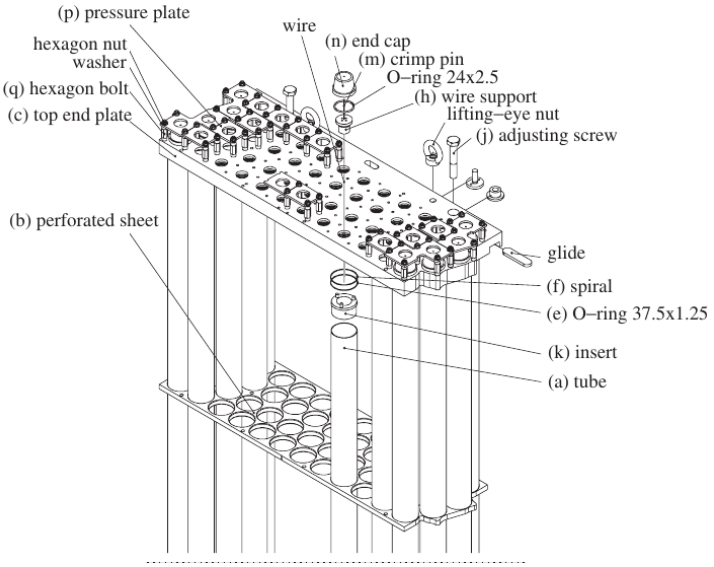

(a) Readout end

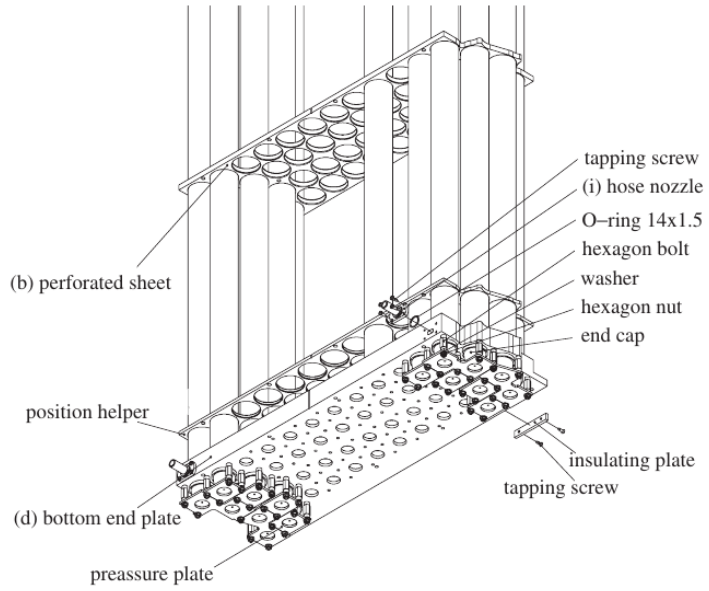

(b) Non-readout end

Figure 6.1: Explosion sketch of an OPERA type drift tube *module*. A module is a physical assembly of 48 drift tubes arranged in four layers of twelve tubes each. Edited from [94].

module produces in average 3.5 hits per module, enabling a two dimensional track fit[2] independently for each drift tube module, which requires at least three hits.

The modules are designed such that they can be placed next to one another without disrupting the staggering of the drift tubes. This is illustrated in figure 6.2. This way, walls of active volume can be easily built. The drift tubes upstream the spectrometer magnet have a length of 110 cm, downstream the magnet the tubes are 160 cm long.

Within one drift tube module, the gas is supplied to its 48 drift tubes through canals

[2]No direction component along the wire axis.

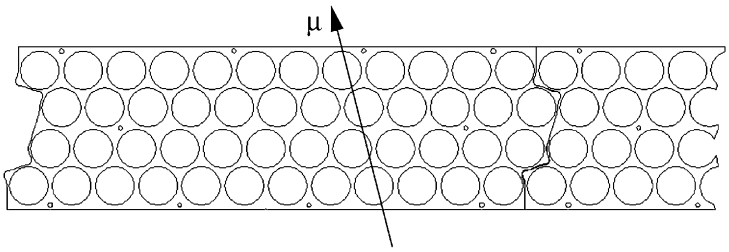

Figure 6.2: Sketch of two drift tube modules next to each other. Note that the module on the right side continues the staggering of its neighbouring modules [94].

milled into the end plates of the module. This way, gas lines are only needed from the gas reservoir, the exhaust and short gas lines connecting whole modules with each other. The connectors for gas lines are strictly on the sides of the modules without readout electronics.

A detailed description of the drift tube modules within the context of the SHiP muon flux measurement can be found in [99].

6.2 Readout Electronics

The electric signals on the drift tubes' sense wires are small amplitude pulse forms, which for this context, are not of particular interest. Due to the small amplitude, the signals are first electronically amplified and discriminated, spacially close the the sense wire. This way, the path, analog signals travel is minimized, reducing the impact of electromagnetic noise picked up on wires from the environment, which digital signals are less prone to. The times, the drift tubes' signals overpass the set discriminator thresholds, can then be recorded. The hardware used for these tasks is presented in the following.

6.2.1 Preamplifiers and Discriminators

The electric signals on the drift tubes' sense wires are too small in amplitude to be detectable by the readout electronics used, specifically the TDC boards[3]. Hence, the signals need to be electronically amplified. In addition, the TDC boards require their input following the digital signal standard *LVDS* [100]. Therefore, the drift tube signals are passed to preamplifier boards that were custom made for the OPERA experiment. Twelve tubes, all in one layer of a drift tube module are served by one preamplifier board. Each board is equipped with three preamplifier chips, each chip serving four channels, hence four drift tubes. The amplifier chips are from the *L3* experiment at CERN [101]. These are *differential amplifiers*, both the positive and negative signal are then passed on the preamplifier board to discriminators, outputting their signals according to the digital LVDS standard. A sketch showing the electronics for amplification and discrimination of

[3]See section 6.2.3.

one drift tube's signal is shown in figure 6.3, a photo of an actual preamplifier board is shown in figure 6.4.

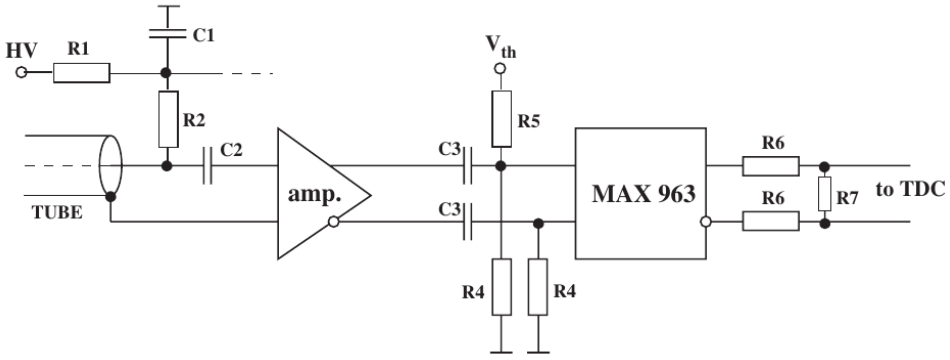

Figure 6.3: Electronics amplifying and discriminating the electric signals from a single drift tube [94].

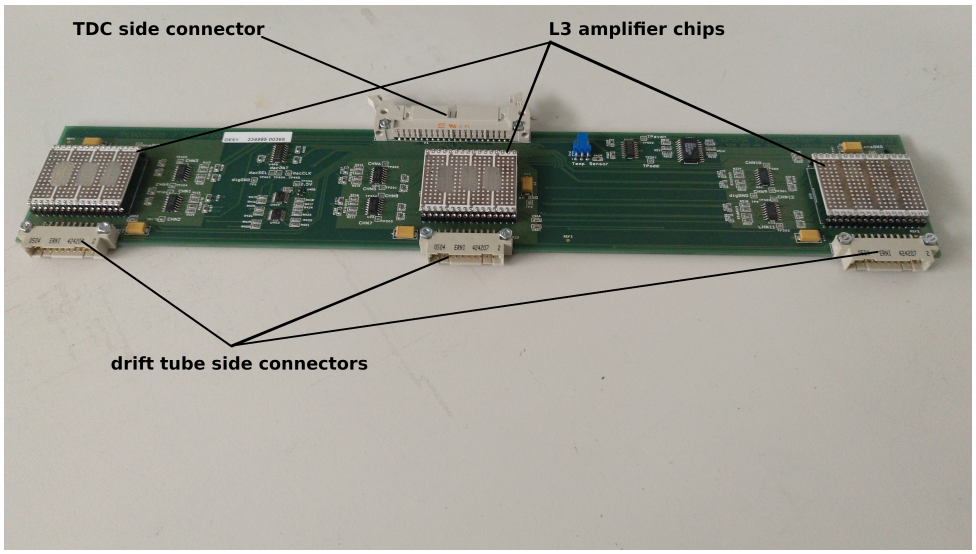

Figure 6.4: Photo of a preamplifier board. These boars are custom designs made for the OPERA experiment. Each board holds three amplifier chips originally designed for the L3 experiment. Each amplifier has four channels, hence one board can serve a layer of twelve drift tubes. Additionally, the preamplifier boards contain discriminators for both the positive and negative output of the differential amplifiers. Hence, each tube requires two output lines, resulting in a total of 24 output signals for the drift tubes only. The *drift tube side* connectors are attached to a distribution board on the drift tube modules, the discriminated signals of the tubes are then fed to TDC readout via 40 line flat cables. A total of 24 of those 40 pins are required for drift tube signals, the remaining pins are used for slow control steering, such as threshold settings for the discriminators. For one drift tube module, four of these preamplifier boards are required.

6.2.2 Slow Control

The slow control describes all tasks related to the readout and steering of the experiment which are not time critical, e.g do not need to be performed for trigger occurrences. In particular, in the context discussed within this thesis, it is limited to setting discriminator thresholds for the analog, amplified drift tube signals and reading the status of the connected preamplifier boards. The discriminators, located on the preamplifier boards discussed above, can have their threshold voltages set utilizing the OPERA Support Board (OSUB) [102]. These are custom boards produced and developed for the OPERA experiment. They provide additional features such as temperature readout from special sensors that were not used or generation of test pulses. The latter feature could not be used since it depends on the use of further legacy OPERA readout electronics that could not deal with the comparably high trigger rate in the experiment discussed within this thesis.

6.2.3 TDC Boards and VME Link

The drift times were recoreded with *time to digital converters (TDCs)*. In particular, boards of the type CAEN v1190A [103] were used. These TDC boards offer 128 channels each and can measure time differences with a resolution of 98 ps. In order to record drift times for each drift tube of the spectrometer as well as some additional times, such as master trigger and PMT times of the scintillators used as triggers, five of these TDC boards were used. Each board has an internal clock with a frequency of 40 MHz. Even though it is possible to provide them an external, synchronized clock, this was not done in the experiment described in this thesis. At each clock cycle, a trigger can be recorded which introduces a time jitter of 25 ns. The correction of the jitter as well as the synchronization of measured times from all the TDC boards, are described in sections 6.6.1 and 6.6.2.

The TDC boards are connected to a VME bus, via which the TDCs can be read out in order to transfer their data to a *DAQ computer*. For this task, an *optical link bridge* was used, in particular the CAEN v2718 [104]. Compared to a VME link via USB, the optical link provides a higher bandwidth. With an expected trigger rate of $f_{\text{trig}} \approx 10\,\text{kHz}$ and tracks passing $n_{\text{mod}} = 6$ modules[4] when transversing the detector with an average of $\langle h \rangle = 3.5$ hits per module, the rate of hits is:

$$R_{\text{hits}} = f_{\text{trig}} \cdot n_{\text{mod}} \cdot \langle h \rangle = 2.1 \cdot 10^5\,\text{s}^{-1}$$

The measured hit times are digitized by the TDC boards with 19 bit accuracy, wrapped into a 32 bit memory block containing additional information such as the TDC chip that recorded an individual hit. Each hit's pulse form might contain several pulses that over-

[4] These are two modules each for stations T1 and T2, one module of T3 and one of T4.

shoot the discriminator threshold and for each of these discriminated pulses, both the times of the rising and the trailing edges are recorded. This is rendered possible since the CAEN v1190 boards allow recording multiple hits per channel and trigger with a dead time of 5 ns. Assuming $n_{\text{pulses}} \approx 3$ pulses per hit, the bandwidth B needed for transfer of the hit data alone can be approximated to:

$$B = R_{\text{hits}} \cdot 2 \cdot n_{\text{pulses}} \cdot 32\,\text{bit} \approx 4.032 \cdot 10^7 \frac{\text{bit}}{\text{s}} = 4.807 \frac{\text{MB}}{\text{s}}$$

Here, the transfer of headers and trailers containing information per trigger are neglected. This data rate exceeds the maximum bandwidth available with the USB 1.0 standard in full speed mode, for which a USB VME bridge would have been available. Even though by only recording the first hits per channel and per hit only the leading edge, it would have been possible to use USB but using an optical link provides a safety margin and allows the recording of extra data. Especially the availability of both leading and trailing edges proved useful for noise rejection, since noise pulses typically have a small *time over threshold* when compared to *real* drift tube hits.

For the readout and steering of the VME boards, a new DAQ software was written using the CAEN VMElib [105] for issuing commands to the VME hardware.

6.3 Assembly

While several drift tube modules used in the drift tube spectrometer were already assembled and ready for use, several modules were newly assembled for the measurement described in this thesis. In addition, mounting frames defining the detector layout of the drift tube spectrometer were built.

At both ends of the tubes, there are aluminum *end plates*, which house canals for supplying drift gas to the tubes of a module as well as feed throughs for the tubes and sense wires. A cross section of a drift tube mounted into a tube end plate is shown in figure 6.5. The tubes themselves are held in the module using a friction fit. The electric contact to the end plates is achieved using a metal spiral scratching the outer tube wall when it is inserted into the end plate, increasing electric contact. Gas tightness is achieved with a rubber o-ring on each side of the end plate. At both and plates, the wires are are spun with a weight of 160 g through plastic wire supports holding it in the center of the tube. Inside the tubes, there a no further wire supports. On both sides then, the wire is fastened using a crimp pin. The drift tube modules are built so that they can be read out on only one side of the wire. This side is called the *read-out side*. On this side, the crimp pin is fed through a plastic end cap and equipped with a conductive socket contact. All the end caps are pressed onto another o-ring for gas tightness using a pressure plate screwed onto bolts next to each end cap.

The assembly of the drift tube modules was performed in Hamburg, the assembled

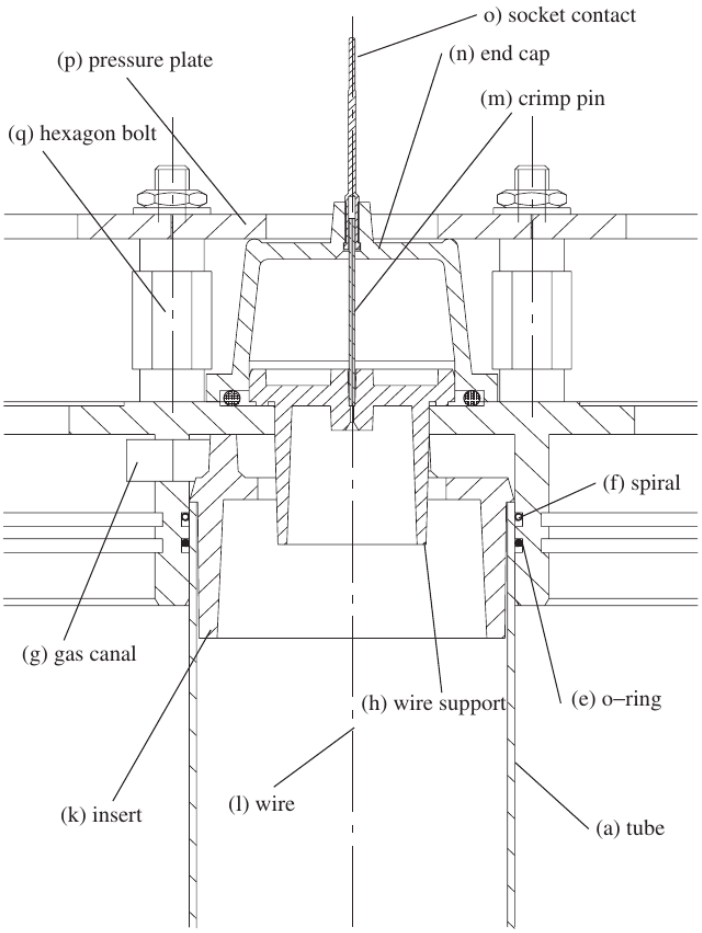

Figure 6.5: Detail drawing of the side for front end electronics of an OPERA type drift tube module [94].

modules were then shipped to CERN for commissioning and testing.

6.4 Commissioning and Testing

After the assembly of the drift tube modules they were shipped to CERN where they were tested during two commissioning visits. For the commissioning and testing, the H8 beamline of the SPS was used. There, muons were available from a more upstream experiment allowing a testing of all drift tube modules with high statistics when compared to a commissioning and testing using only atmospheric muons. Goals of the commissioning visits were to check if the drift tube modules, especially the newly assembled ones, work as intended and, if needed, replace dead channels, which could happen for example if a wire ripped during transport. Additionally, parameters such as high voltage of the tubes as well as threshold voltages for the discriminators were examined. Lastly, the commissioning served as an integration test of the newly developed DAQ process (see chapter 6.6).

Here, the drift tube stations T1 through T4 were assembled from the individual modules. Figure 6.6 shows a photo of the drift tube modules of stations T1 and T2 during

the commissioning phase at the H8 beam line. For the stations T1 and T2, aluminum

(a) T1

(b) T2

Figure 6.6: Photography of stations T1 and T2 during the commissioning phase at the H8 beamline at the CERN SPS. During the commissioning phase, all the wiring for providing high and low voltage to the tubes and readout electronics was attached. Aluminum plates covering the preamplifier boards have been attached as well as shielding against electromagnetic noise. The holding frames for the drift tube modules of T1 and T2 were attached to each other during the commissioning phase for better stability, here it is shown before connecting them.

shielding covers for the amplifiers, shielding the analog electronic part from electromagnetic noise, were attached and tested. For the final setup, the stations T1 and T2, as well as the stations T3 and T4 would have been connected to each other for improved stability. In the experimental area at the H8 beam line, however, there was not enough space to connect T3 and T4 to each other. Therefore, the detector walls of T3 and T4 were assembled individually, while T1 and T2 were already connected and later transported as a unit to the H4 beam line using a crane.

A photo showing the drift tube wall T3 at the H8 beam line in the commissioning phase is shown in figure 6.7.

Figure 6.7: Photography of stations T1, T2 and T3 at the H8 beamline at the SPS during the commissioning phase. This is the final status after the first commissioning visit.

Using the straight muon tracks available at the H8 beam line, the data quality could have been analyzed for the newly assembled detector. Monitoring the data quality was mainly done using the dirft time spectra, which are well known from prior knowledge of the same detector type used in the OPERA experiment. While commissioning the detector, methods to reject noise could have been tested as well. Noise, produces hits at random times, which result in a flat distribution overlaying the drift time spectrum. This can often be rejected by a cut for the *time over threshold*, which is available since both the leading and trailing edge times are recorded by the TDCs. Here, the cut is applied such that hits with a time over threshold below 10 ns are rejected. A representative drift time spectrum for this detector is shown in figure 6.8. The effect of the applied cut for noise is shown in figure 6.9. In figure 6.9, a peak at small times can be seen which can be corrected for with the noise cut as well. This is also typical for noise since the probability for a voltage pulse due to noise to surpass a certain discriminator threshold is constant

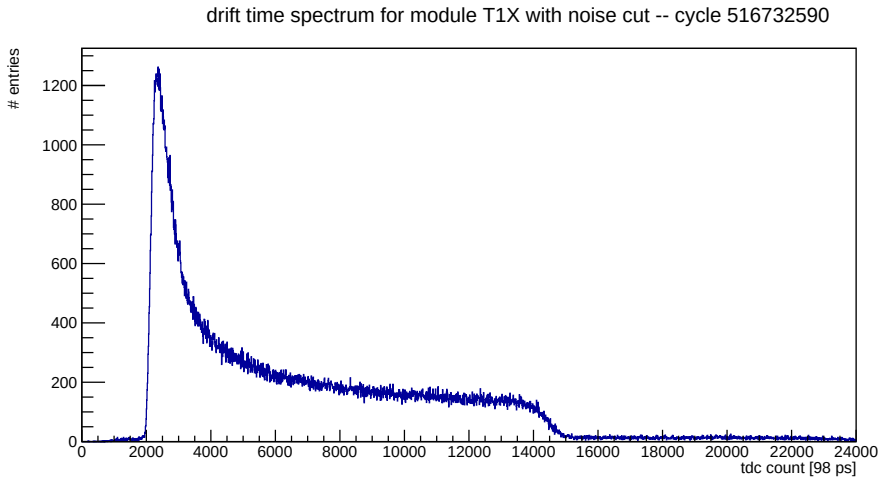

Figure 6.8: Drift time spectrum for the drift tube module T1X. This contains a simple noise cut where events that did not surpass the trigger threshold for a certain time over threshold are not considered. Note that this drift time spectrum was taken from a run in the physics data acquisition. However, this plot is representative for the data quality achieved in the commissioning phase. The drift time spectrum shows the behavior known for this drift tube design from the OPERA experiment.

over time. For later times, this leads to an exponential drop in the drift time spectrum, representing the probability of the *first* noise pulse surpassing the threshold. The fact that a constant noise distribution is present in the drift time spectrum (fig. 6.9(a)) in addition to the exponential drop, hints towards the presence of at least two systematically different noise amplitudes.

The drift tubes are supplied with drift gas one after another in a gas line, hence the drift gas quality can differ throughout the gas line. To account for this, the rt-relations are calculated for individual sets of four drift tubes, following each other in the gas line. Furthermore, new rt-relations are calculated for each spill of protons to consider changes of the drift gas quality over time.

6.5 Experimental Setup

After the commissioning phase, drift tube stations were transported using a crane to the H4 beam line. Here, the drift tube walls of stations T3 and T4 were connected to each other and the detector was prepared for the *survey measurement*, described in section 6.5.2, which provided an initial coordinate measurement of the detector components. The gas supply lines were setup, with the order of gas flow entering station T1, followed by T2, T4 and last T3.

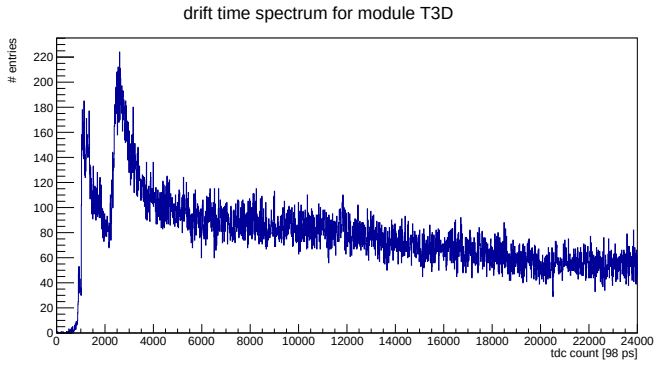

(a) before noise cut

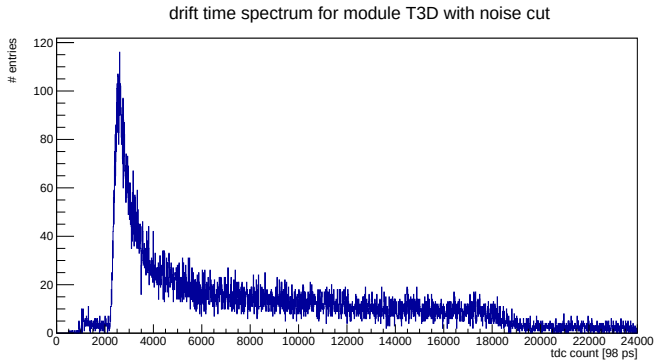

(b) with noise cut

Figure 6.9: Drift time spectrum for module T3D before (a) and after (a) applying a noise cut via time over threshold. Here, only hits were accepted with a time over threshold of more than 10 ns. Since this is a lateral module of the T3 detector wall and far off the beam axis, it has a comparably low number of hits. This increases the effect of noise, which can be seen as more or less flat distribution overlaying the drift time spectrum. By applying a cut, only accepting larger time over thresholds, this noise can be largely reduced. The larger peak before the beginning of the drift time spectrum before the cut is typical for noise as well and can be reduced using a larger discriminator threshold.

6.5.1 Drift Gas Supply

Throughout all measurements described in this thesis, a drift gas mixture of Ar:CO_2 in the mixing ratio 80:20 is used. To ensure a continuous flow of gas, gas is provided from large gas tanks with the pressure reduced $\sim$ 2 bar overpressure compared to the surrounding environment. All drift tube stations are supplied gas in a single line, starting at station T1, passing through stations T2, T4 and finally T3. A closure for gas tightness is achieved using a bubbler, where the gas flow exhausted from the last drift tube module in the gas flow is led through oil with the exhaust valve is under the oil's surface. This prevents surrounding air to enter the drift tubes.

6.5.2 Survey Measurement

After setting up the detector[5], CERN's survey group performed an optical survey measurement, providing coordinates of measurement points attached to the individual detector elements with an accuracy of 500 µm at a $1\,\sigma$ level, described in [106]. The survey measurement provided coordinate measurements of the beam counter, the target and all drift tube stations.

The survey measurement used optical reflector targets of known dimensions that were attached to predefined spots on each measured detector part. The coordinates were given for each of those reflector targets and from those the exact locations of each detector component were calculated.

For the survey, a line of sight to the optical target is needed from a large area around the detector. Due to the front-end electronics at one end of the drift tube modules, bolt adapters were therefore needed as attachment points for the optical targets, which is shown in figure 6.10. In order to determine the exact positions of the individual drift tubes themselves (e.g the top and bottom end positions of a sense wire), the sizes of the optical target, as well as the attachment bolt need to be corrected. The correction of the attachment bolts and the conversion of the coordinates in the reference frame, the survey used, to the FairShip reference frame is described in [99].

6.6 Data Acquisition

In order to fulfill the experimental requirements for the measurements described here, a new data acquisition (*DAQ*) was developed. The DAQ system used at OPERA for the drift tube spectrometer was not considered suitable due to the comparably high trigger rate and dated software basis. In principle, the process of data acquisition describes both the software and hardware used to digitize and record physical signals, such as voltages. Here, the focus will be on the software and the processing of the digitized data. The hardware that was used is described in chapter 6.2 and the references given there.

6.6.1 Drift Time Measurement and Jitter Rejection

The CAEN v1190 TDC boards provide an internal 40 Mhz clock. Even though a trigger signal can be accepted by the TDC boards at any time, the creation of an event time stamp is only possible after a clock cycle, if a trigger occurred in the last cycle. This results in a *jitter* of 25 ns, as this is the resolution that the trigger time is known to. The time resolution of the TDC chips themselves, on the other hand is much better and can be set to as high as 98 ps, which was used for the measurements described within this thesis.

[5]For the muon flux and spectrum measurement. After changing the setup for the charm CC measurement, another survey measurement was performed.

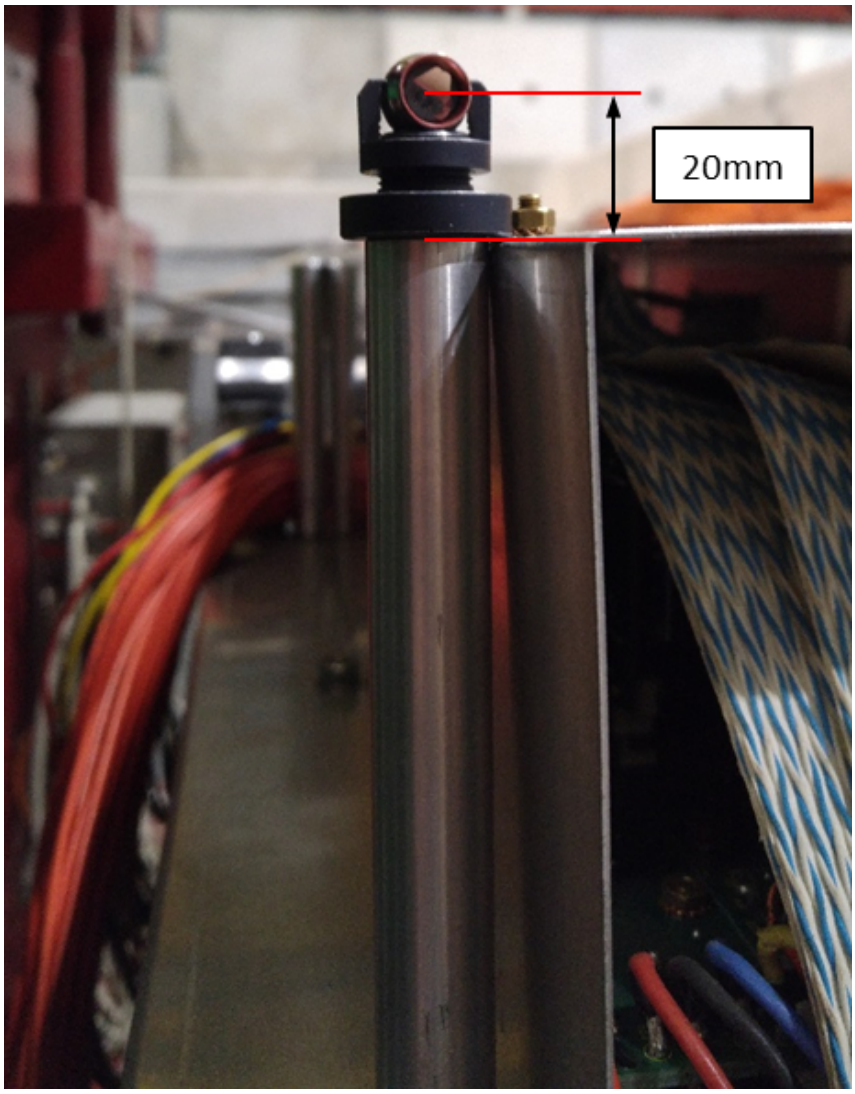

Figure 6.10: Photo of the survey target attached to the bolt adapter for the survey measurement [106]. The black optical reflector target needed to be attached on an adapter bolt so that the target reaches over the aluminum shielding of the front-end electronics. This way, the optical target can be seen from around the detector which is needed for the optical alignment.

The measurements of all TDC channels, are started at the same time and *time differences* of the recorded channels on one TDC board can be measured with the set resolution of 98 ps. Therefore, the trigger signal itself is recorded on a separate TDC channel, enabling a high resolution calculation of the drift time. The jitter can then be rejected by subtracting the trigger time t_{trig}, recorded on each TDC, from the measured signal arrival time. This is then corrected for jitter. The trigger signal that is distributed to all TDC boards, however, is delayed by an OPERA Trigger Board (OTB) [107]. The OTB was first foreseen to be used for generating the trigger coincidence logic but was then replaced by extra hardware during the experiments commissioning phase. Since the process was tested with the OTB beforehand, however, the delay was kept in place. When the drift time t_d is now calculated as $t_d = t_{\text{signal}} - t_{\text{trig}}$, the resulting drift time spectrum

is systematically shifted to later times by the delay from the OTB.

So, to calculate an absolute drift time from the time difference described above, it needs to be corrected for the undelayed *master trigger* time t_{mt}, which is only recorded on TDC4.

Finally, the drift time t_d for a channel on TDC x is calculated via:

$$t_d = (t_{\mathrm{signal}} - t_{\mathrm{trig}})_{\mathrm{TDC}x} - (t_{\mathrm{mt}} - t_{\mathrm{trig}})_{\mathrm{TDC4}} \,. \tag{6.1}$$

The distribution of delayed and undelayed trigger signals to the different TDC boards is shown in figure 6.11. The distribution of (delayed) trigger arrival times for one spill is

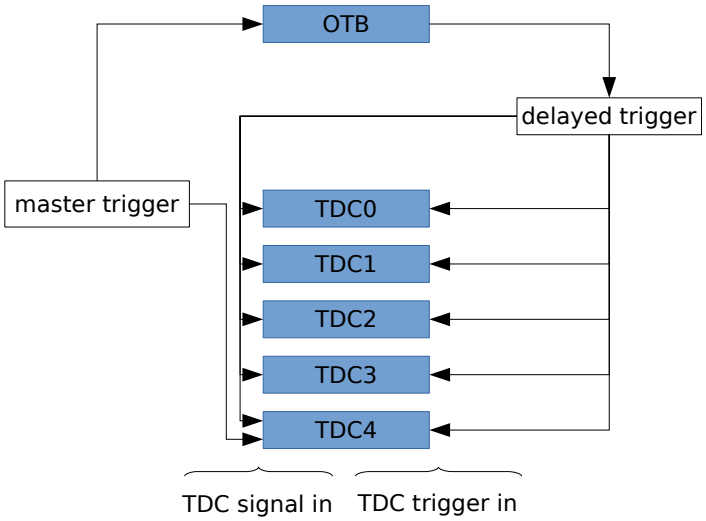

Figure 6.11: Distribution of master trigger signal to TDC boards. The master trigger is delayed by the OPERA Trigger Board (OTB). The delayed signal then triggers the readout on each TDC board. In addition, the delayed signal is read on a TDC channel on each TDC board. This way, the jitter due to the 40 MHz clock of the TDC boards can be corrected. The arrows denote signal propagation paths, the end without the arrowhead is an output, the other side is connected to an input. The TDC inputs on the left hand side denote the sockets for signal input on the TDC boards, the right hand side inputs are trigger input sockets.

shown for TDC as an example in figure 6.12. This clearly shows the jitter of 25 ns as width of the distribution. This distribution is representative for the according distributions of the other TDC boards, which are shown in the appendix in figure A.1.

6.6.2 Asynchronous Clock Correction

Usually, in this context, a clock synchronization is not required since all measured drift times are corrected for the master trigger time, which is recorded on TDC4[6]. This way, TDC4 serves as *master board* and time stamps for the events are calculated using its

[6]See section 6.6.1.

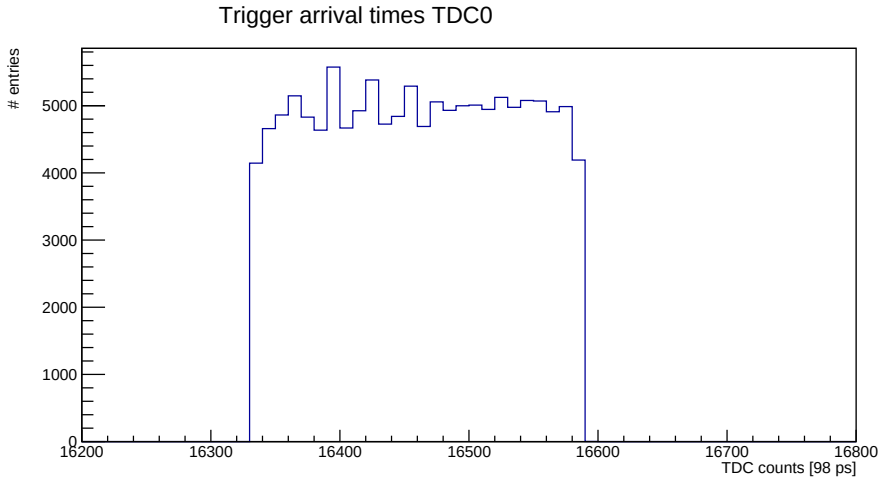

Figure 6.12: Histogram of trigger arrival times recorded for one spill on TDC0. It shows a flat distribution with a width of 25 ns. This width accounts for the jitter since the trigger arrives at a random time between two clock cycles of the TDC's internal 40 MHz clock.

master trigger arrival time. The absolute time stamps for each trigger are then calculated as the time from the start of the proton spill[7].

In case any errors occur and the master board's clock counter cannot be used, a different method to calculate time stamps was used. Then, for *all* TDC boards except the master board, the number of their individual clocks' cycles since the last trigger is calculated. If these numbers match[8], this count is added to the last known clock counter of the master board. In case the numbers of clock cycles for the remaining boards do not match, but two of them had the same number of clock cycles since the last trigger, this number is added to the clock counter of the master board. If however, all three remaining TDC boards have unmatching clock counts since the last trigger or more than one TDC boards had readout errors for a specific event, the event is rejected and an error message is sent to the central DAQ host.

6.6.3 SHiP Data Formatting

The data collected by the TDCs is converted to a data format which is foreseen to be used in the SHiP experiment. Hence, the whole DAQ process for the experiment discussed here, also serves as a testbed for online data handling using the SHiP data format.

Data is ordered in `DataFrame`s, representing one triggered event. Each subdetector creates such a `DataFrame` for each trigger. A frame consists of a header and a data part. The header contains general information of the triggered event, such as the total size the event in bytes, the `partitionID` which encodes the subdetector that sent a particular

[7]The start of the spill is announced via network and a hardware NIM signal is sent. Its arrival time is the start of spill reference. See section 6.6.5 for technical details.

[8]Which they typically do.

`DataFrame`. The drift tube spectrometer, in this experiment, has the `partitionID` *0C00*. It additionally holds a cycle identified which encodes the spill of protons that a frame belongs to. The header also contains a frame time which is a 25 ns precision time stamp of the triggered event. The time extent, encoded in the SHiP data format header, was used here to store the sequential trigger number in contrast to its use for SHiP, where triggerless readout is foreseen. Lastly, the header contains flags which can be used to encode errors that occurred during data acquisition. An illustration detailing the header as part of a `DataFrame` is shown in figure 6.13. Following the header, the hits recorded

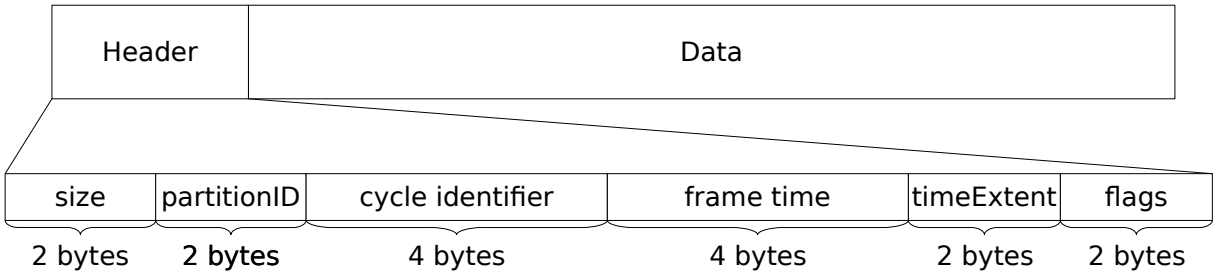

Figure 6.13: Illustration of data structure sent to the event builder via network. For each trigger, a data frame is constructed and sent. It consists of a 16 byte long header, followed by the formatted hits. It contains the size of the complete event in bytes and the partition ID, identifying a subdetector, for the drift tube spectrometer this is 0C00. Additionally it holds a cycle identified, encoding the spill that this event is a part of as well as the frame time, which is the time stamp for the trigger of this event. The field timeExtent is in this context not used according to its name but holds a sequential trigger number within the spill. Finally, the header contains a field for flags, which can be used to encode errors that occurred during data acquisition or conversion of an event.

for that event are located within the `DataFrame`. The hits are formatted according to the `RawDataHit` subformat, which holds the channel (drift tube) that was hit and a hit time for that channel. For the drift tube spectrometer, the hit time was the measured drift time. A `RawDataHit` can contain optional extra data, which was not used for the drift tube spectrometer. The `RawDataHit` structures are sequentially ordered in memory following the header for each hit of an event. This is illustrated in figure 6.14.

6.6.4 Data Storage

The acquired data collected during one spill is held in RAM for the duration of that spill. Therefore, a buffer of 100 MB size is used. The raw data sent by the TDC boards via the VME bus is collected in that buffer. In case the buffer runs full, dynamic allocation of more buffers is possible, but the first buffer is planned such that it should be sufficient. This should minimize time costly memory allocation operations while in the spill with a high trigger rate. From this buffer, the data conversion to the SHiP data format was

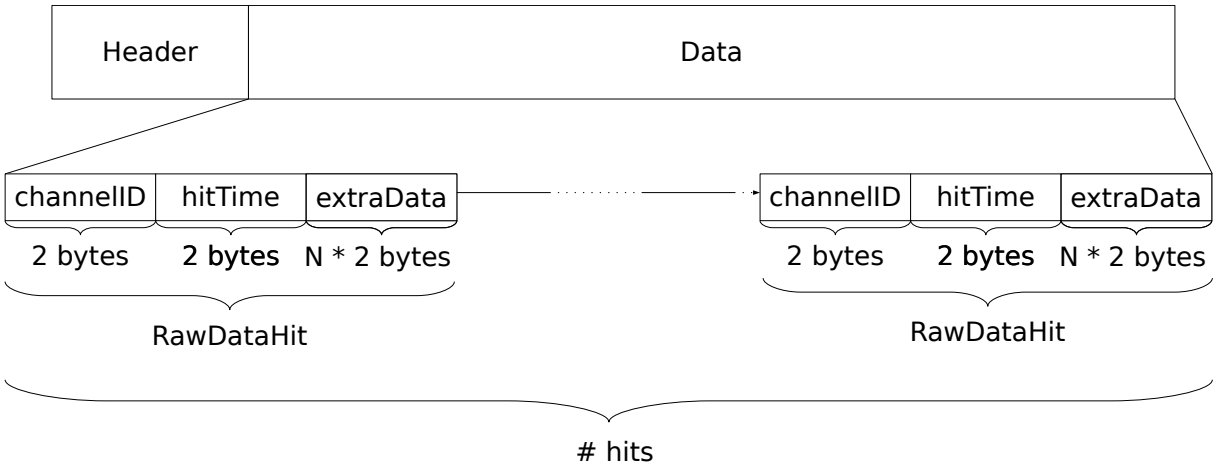

Figure 6.14: Illustration of the formatted hits sent via network as part of a `DataFrame`. The channel ID identifies an individual drift tube and the hit time holds the measured drift time for that tube. The field for extra data was not used for the drift tube spectrometer.

performed. Both the raw data from the TDCs as well as the converted data in the SHiP format were stored on the local hard disk of the DAQ computer and backed up at CERN and on a UHH[9] file server. The backup of the raw TDC data allows the later offline reconversion, in case any errors in the SHiP format conversion were detected.

6.6.5 Network Control and Data Transfer

Transferring of acquired data from the local DAQ PC to the event builder PC, as well as remote state setting[10] of the DAQ software, is performed via a TCP/IP network connection. Therefore, the *ControlHost* software package [108] is used, which implements a *publisher/subscriber* model. A central controlling computer serves as publisher for so-called `DAQCommand`s. The computers controlling the local DAQ for a specific subdetector subscribe to the distribution of `DAQCommand`s, which is then handled by the ControlHost library. Each `DAQCommand` has an attached *payload* which specifies the receiver of the command, which can be a single subdetector or any set, including all subdetectors. Additionally, it contains a message, what action is expected to be performed.

After a `DAQCommand` was received by a local DAQ computer (from now on *client*), its receipt must be acknowledged by sending a `DAQAck` message, which on the other hand the central DAQ controller subscribed to. When the actions that were requested in a command are completed or no actions needed to be performed, an additional `DAQDone` message is sent back by all clients to the central DAQ.

It is possible to disable certain subdetectors via a command, requiring them to not take any data at triggers until reactivated. Even though a subdetector might be disabled, all

[9] Universität Hamburg
[10] Active, waiting, disabled, etc.

commands must be checked and acknowledged. A list of the `DAQCommand`s that can be issued to the subdetectors by the central DAQ control is given in table 6.1. This includes possible payloads for those commands as well as the expected reaction to the command.

Table 6.1: Commands that can be issued by the central DAQ host to the local computers controlling the DAQ and slow control for one subdetector.

`DAQCOMMAND` label	payload	reaction
SoR (Start of RUN)	• RUN ID (• subdetector ID)	• acknowledge receipt • prepare DAQ for new RUN if own or no detID is passed • create directory for new RUN • send SoR data frame • report done
SoS (Start of Spill)	• Cycle ID	• acknowledge receipt (if active) • run DAQ loop • record SoS hardware signal • read reference time for spill • send SoS data frame • report done • record and send data
EoS (End of Spill)	• Cycle ID	• acknowledge receipt • record EoS hardware signal • send EoS data frame • do not wait for trigger only wait for new commands • wait until all data for ended spill is sent • report done including number of triggers
EoR (End of Run)	• RUN ID	• acknowledge receipt • send EoR data frame • report done
Enable	• subdetector ID	• acknowledge receipt • record data until disabled • report done
Disable	• subdetector ID	• acknowledge receipt • do not record data until enabled • report done
Stop	• subdetector ID	• acknowledge receipt • end DAQ process
EvbLimit	• number of events	• acknowledge receipt • limit number of events per spill sent via network • report done

A special command is the *SoS* (Start of Spill) command. In addition to acknowledging its receipt, the subdetectors are provided a NIM signal with the command. The hardware

signal needs to be recorded and and special `DataFrame`[11] is generated. The header of that `DataFrame` contains the information that it is a SoS-frame encoded in the cycle identifier and the frame time at which the SoS signal was recorded. This serves as reference time for the incoming spill. This `DataFrame` is sent via network to the event builder process. After sending the `DataFrame`, the `DAQDone` report is sent. Since each subdetector sends these frames with their individual reference times, the event builder can already do online consistency checks since the frame times of each subdetector are expected to match. However, if the reference times differ for detectors but they have consistent trigger times within the spill for their own local DAQ, the data acquired with that particular detector can later be matched to that of the other detectors, since its own reference time was reported to the event builder.

A similar procedure is required after receiving the *EoS* (End of Spill) command, which is again accompanied by a NIM hardware signal. A special `DataFrame` is sent again, enabling to compute the total time of data acquisition for the past spill, which can provide useful data for later, offline data matching in case the subdetectors report mismatching time stamps.

The `DataFrame`s constructed by the local DAQ processes during the spill are also sent to the event builder. This can either happen while in the spill or after receiving the EoS command. For the DAQ of the drift tube spectrometer, a high performance local DAQ application was developed, allowing both of these methods. In operation however, the data was sent after receiving the EoS command. After all `DataFrame`s are sent, the special EoS frame is sent at the very last frame of a spill. After that, the reaction to the EoS command is reported done.

[11] See section 6.6.3.

Part III

Alignment

7 Method Description

In order to perform a track fit from individual measurements of the detector components, knowledge about the positions of the hit detector components is crucial. The initially used positions of each part of the detector were calculated from the survey measurement, as described in [106, 99]. However, these measurements do have a finite precision, and other limitations. For example, due to switching the Goliath magnet on or off or maintenance work on the detector, the measurements and calculated positions of the detector components might be different from their actual positions. The process of correcting these offsets using data taken with this *misaligned* detector is called *alignment*. The alignment of the drift tube spectrometer used here, will be described in the following chapter.

7.1 Track Based Alignment

A common way of performing an alignment of a tracking detector is called *track based alignment*. Here tracks are needed that are known to be straight. Therefore, during the phase of data acquisition, special sets of data were taken with the Goliath magnet switched off. This resulted in muon tracks without curvature passing the spectrometer. When performing a straight line fit of these tracks, by analyzing the residuals for specific sets of drift tubes, systematic offsets can be studied. Therefore, a sufficient number of tracks passing the detector is needed in order to reduce statistic errors.

While taking data, the taken data was grouped into *runs*. Each run is performed with a certain set of parameters, such as magnetic field strength or operating parameters of the detectors, such as discriminator threshold voltages or gas pressure for the drift tubes. A total of three runs was taken with the magnetic field of Goliath switched off. These are in particular:

1. RUN 2199
2. RUN 2200
3. RUN 2201

In reality, the muon tracks however are not exactly straight. When the muon passes the material of the detector, such as the aluminum walls of the drift tubes, they can undergo scattering on the material, introducing *kinks* to the track. This effect, however is smaller for higher energy muons, so methods can be applied to select higher energy muon tracks

for alignment. The energy of the muons, on the other hand, can not be directly calculated without being able to measure the muon momentum in the absence of a magnetic field.

To select higher energy tracks, the tracks fitted in the drift tube spectrometer can be extrapolated to the RPC muon tagger. Between each layer of the RPC detector, iron is placed. A track, reaching the most downstream layer of RPC needs at least a minimal amount of energy.

Systematic offsets can be analyzed in several different ways. Here, the well tested software package *Millepede II* [109, 110] is used. This is a two part process, first the data needed for alignment is gathered. From this data the standalone *pede* application calculates the corrections to the detector coordinates in a global fitting process[1]. The collection of the data needed by pede is done by performing a *refit* of the tracks using the General Broken Lines (GBL) algorithm [111].

7.2 GBL Refit

The GBL track fit is based on the already implemented track fit using a Kalman fit algorithm with annealing from the genfit software package. The Kalman fitted track serves as *seed* for the GBL fit. As a Kalman fitted tack, in principle, might include scattering between points, which is not included in the linear track model for this GBL fit, the first and last hits of this track are used with a linear interpolation between them. For this strictly linear track, a *predicted measurement* is calculated as the shortest distance between the seed track and the wire for each hit tube. When compared to the drift radius measured by a hit tube, a *residual* can be calculated. These residuals, are provided to the GBL fitting algorithm alongside a Jacobi-Matrix defining the propagation of track parameters from one hit to another. The GBL fitting algorithm now minimizes the residuals by altering the parameters of the linear track model, which are introduced in the following section.

When, in addition to the values mentioned above, the dependence of the residuals of some *global parameters of the detector* is provided, the data needed for alignment can be calculated in the fitting process which can later be fitted using the program *pede*. The calculation of all values needed for fitting and alignment is presented in the following sections.

7.2.1 Shortest Distance Between Seed Track and Sense Wire

The shortest distance between a seed track and the sense wire of a hit tube can be calculated as the shortest distance between two straight lines. The approximation of two infinitely long lines is applicable since the channel that the sense wire belongs to must

[1] See reference [110] for details.

have a hit recorded to be selected. We describe a straight line by the vector equation

$$\vec{s} = \vec{x}_0 + s \cdot \vec{d}. \tag{7.1}$$

In equation (7.1), $\vec{x}_0$ is any point on the line, s is an arbitrary scalar and $\vec{d}$ the direction of the straight.

For calculating the closest approach of two lines, we start with two straight lines, one for the seed track and one for the wire.

$$\vec{s}_{\text{track}} = \vec{x}_1 + s \cdot \vec{d}_1 \tag{7.2}$$
$$\vec{s}_{\text{wire}} = \vec{x}_2 + t \cdot \vec{d}_2 \tag{7.3}$$

The shortest distance is the vector $\vec{\sigma}$ connecting the *points of closest approach* (PCA) on each line with each other. When we call the PCA on the track $\vec{x}$ and the PCA on the wire $\vec{y}$, we can write $\vec{\sigma}$ as

$$\vec{\sigma} = \vec{x} - \vec{y} \tag{7.4}$$

Since $\vec{x}$ and $\vec{y}$ are on these lines, we can insert (7.2) for $\vec{x}$ and (7.3) for $\vec{y}$. This results in

$$\vec{\sigma} = \vec{x}_1 + s \cdot \vec{d}_1 - \left(\vec{x}_2 + t \cdot \vec{d}_2\right) \tag{7.5}$$
$$= \vec{x}_1 - \vec{x}_2 + s \cdot \vec{d}_1 - t \cdot \vec{d}_2 \tag{7.6}$$
$$= \vec{q} + s \cdot \vec{d}_1 - t \cdot \vec{d}_2. \tag{7.7}$$

In equation (7.7), $\vec{q} := \vec{x}_1 - \vec{x}_2$ was used.

For unknown values of s and t, $\vec{\sigma}$ describes a plane that contains the track and is parallel to the wire. The shortest distance is perpendicular both to the track and the wire. So by demanding

$$\vec{\sigma} \perp \vec{x}, \vec{y}$$

we can write the requirement

$$\vec{\sigma} \cdot \vec{d}_1 = 0, \tag{7.8}$$
$$\vec{\sigma} \cdot \vec{d}_2 = 0. \tag{7.9}$$

By inserting (7.7), this can be written as

$$0 = \left(\vec{q} + s \cdot \vec{d}_1 - t \cdot \vec{d}_2\right) \cdot \vec{d}_1 \tag{7.10}$$
$$= \vec{q} \cdot \vec{d}_1 + s\left(\vec{d}_1 \cdot \vec{d}_1\right) - t\left(\vec{d}_2 \cdot \vec{d}_1\right), \tag{7.11}$$
$$0 = \left(\vec{q} + s \cdot \vec{d}_1 - t \cdot \vec{d}_2\right) \cdot \vec{d}_2 \tag{7.12}$$
$$= \vec{q} \cdot \vec{d}_2 + s\left(\vec{d}_1 \cdot \vec{d}_2\right) - t\left(\vec{d}_2 \cdot \vec{d}_2\right). \tag{7.13}$$

In (7.11) and (7.13) the terms $\vec{q} \cdot \vec{d_i}$ are constants and both these equations can be subtracted by this term. This results in

$$-\vec{q} \cdot \vec{d_1} = s\left(\vec{d_1} \cdot \vec{d_1}\right) - t\left(\vec{d_2} \cdot \vec{d_1}\right), \tag{7.14}$$

$$-\vec{q} \cdot \vec{d_2} = s\left(\vec{d_1} \cdot \vec{d_2}\right) - t\left(\vec{d_2} \cdot \vec{d_2}\right). \tag{7.15}$$

$$\tag{7.16}$$

This equation system can be solved as the matrix equation

$$\begin{pmatrix} \vec{d_1} \cdot \vec{d_1} & \vec{d_2} \cdot \vec{d_1} \\ \vec{d_1} \cdot \vec{d_2} & \vec{d_2} \cdot \vec{d_2} \end{pmatrix} \cdot \begin{pmatrix} s \\ t \end{pmatrix} = \begin{pmatrix} -\vec{q} \cdot \vec{d_1} \\ -\vec{q} \cdot \vec{d_2} \end{pmatrix} \tag{7.17}$$

The equation (7.17) can then be solved by any appropriate algorithm. Within the context of this thesis, the equation was solved by the *LU decomposition* algorithm from the ROOT software framework [112], where L and U are (L)ower and (U)pper triagonal matrices which are the results of a Gaussian elimination so that

$$M = L \cdot U.$$

Now, by extrapolating each of the two straights by s or t times their direction respectively, the points of closest approach can be calculated. Using this, now the vector $\vec{\sigma}$ expressing the shortest distance between track and wire can be calculated via equation (7.7).

Implementation When applied to the actual experiment data, the track is described by equation (7.2). Here, the position $\vec{x}_1$ on the track is the first hit coordinate from the seed track. The direction $\vec{d_1}$ is the difference vector of the hit locations between the very first and very last hits.

The wire on the other hand, described by equation (7.3), has a direction $\vec{d_2}$ which is the difference vector of the top and bottom ends of the wire. These are calculated from the *survey measurement*[2] performed by CERN's survey group, taking the design of a drift tube module[3] into account.

7.2.1.1 Residual Vector

The residual vector $\vec{r}$ is the difference between the shortest distance $\vec{d}$ and the drift distance r_t that is obtained from a drift time measurement and then calculated using the rt-relation as shown in chapter 4.3. The drift distance r_t is only known as a scalar. So the *measurement* vector $\vec{m}$ can be defined as the shortest distance $\vec{d}$ between track and

[2] See section 6.5.2.
[3] See section 6.1.

wire scaled to the length r_t. The residual $\vec{r}$ can be calculated using:

$$\vec{r} = \vec{d} - r_t \cdot \frac{\vec{d}}{|\vec{d}|} = \vec{d} - \vec{m} \tag{7.18}$$

This residual vector is sketched in figure 7.1.

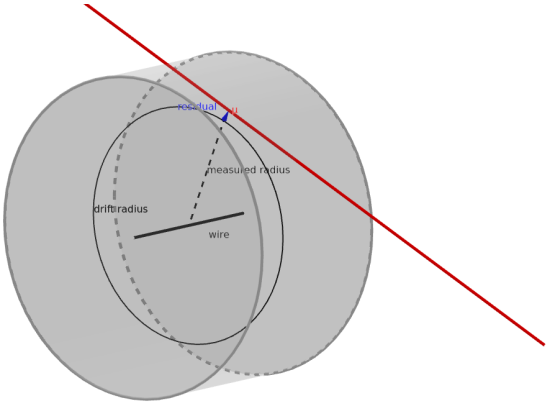

(a) Overview

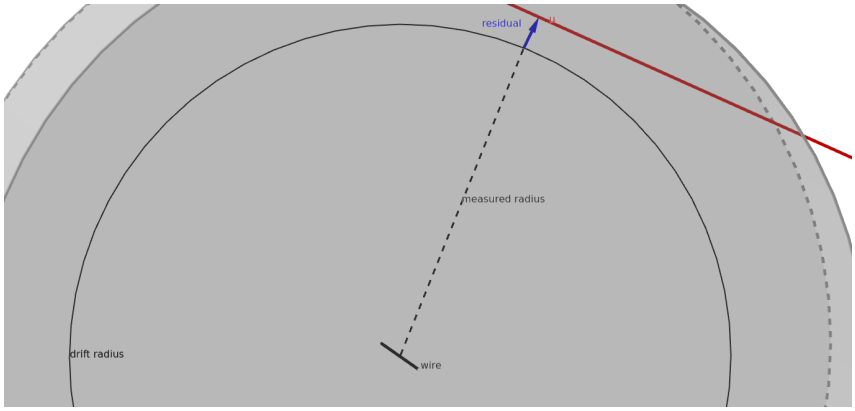

(b) Detailed view on the residual vector

Figure 7.1: Sketch showing the residual vector that the GBL fitter is provided. An overview is shown in 7.1(a) and a more detailed view on the residual is shown in 7.1(b). A fitted muon track or any other track prediction (red) crosses the tube and passes the wire (solid black). The shortest distance (dashed black) between wire and track can be calculated. The difference between measured drift circle (solid black circle) and shortest distance now is the residual (solid blue vector).

Note that the residual $\vec{r}$ can be defined in a different way, namely as

$$\vec{r}_{alt} = \vec{m} - \vec{d} \tag{7.19}$$

The residuals shown in (7.18) and (7.19) are slightly different. In the first case (7.18), if the measured drift distance is larger than the distance $\vec{d}$ between track and wire, the residual vector will point in the opposite direction as $\vec{d}$, while for a too short drift distance,

it will point in the same direction as $\vec{d}$.

For a residual shown in (7.19), on the other hand, a too small drift distance will result in a residual anti parallel to $\vec{d}$ and vice versa.

7.2.2 Measurement and Fit Reference Frames

The fit could, in principle, be performed in any reference frame. The frame, that the fit is performed in is called the *fit frame* for short. For a drift tube measurement, this exploits the missing resolution of drift tubes along their sense wires, reducing the dimension of the fit problem. The fit frame chosen here are the offsets in the *global* x and y directions for a plane perpendicular to the beam direction at any given *global* z. So the base vectors of the fit frame are the global x, y-directions. When expressed as a matrix of row vectors, the fit system base B_f is:

$$B_f = \begin{pmatrix} 1 & 0 & 0 \\ 0 & 1 & 0 \end{pmatrix} \tag{7.20}$$

In addition to the fit frame, for each hit a 2-dimensional *measurement frame* can be defined, where one direction is parallel to the shortest distance between track and wire and the other axis is parallel to the sense wire of a hit tube. To calculate the residual in this measurement frame, the shortest distance $\vec{d}$ between track and wire is calculated using equation (7.7). From there on, the rotational matrix R is calculated, rotating this vector $\vec{d}$, which is expressed in global coordinates, such that it is parallel to the x'-axis of the new measurement frame. Now, the residual vector $\vec{r}$ calculated using equation (7.18) can be expressed in the measurement frame. Then, the residual $\vec{r}'$ in this system is:

$$\vec{r}' = R \cdot \vec{d} - \begin{pmatrix} r_t \\ 0 \\ 0 \end{pmatrix} \tag{7.21}$$

In equation (7.21), r_t denotes the measured radius of the drift circle which is calculated from the measured drift time. Now, the third component of this vector, which is parallel to the beam direction, can be dropped to obtain the needed 2-dimensional measurement vector for the GBL fit.

The precision $\vec{\varsigma}$ of the detector, for a given spatial resolution σ of a drift tube in this reference frame is:

$$\vec{\varsigma} = \begin{pmatrix} \sigma^{-2} \\ 0 \end{pmatrix} \tag{7.22}$$

This reference frame is beneficial for detectors like drift tubes, only capable of delivering a 1-dimensional measurement such as the radius of a drift circle, since all components with a precision ς of zero are dropped in the process of fitting the track in GBL.

Now, every hit of a track is expressed in a different reference frame. Before providing them to the GBL fit algorithm, a projection matrix for this hit to the fit frame must be

calculated and provided with the residuals.

7.2.2.1 Projection Matrix

The projection from the fit system to the measurement system is a (2×2) matrix. It is calculated using the rotation matrix M transforming a vector expressed in the measurement reference frame to the global reference frame. This is the inverse of the rotational matrix R, calculated for equation (7.21), hence

$$M = R^{-1}.$$

Finally, the projection matrix P can be calculated as

$$P = (B_f \cdot M)^{-1}, \tag{7.23}$$

using the base vectors of the fit system B_f from equation (7.20). In the end, the GBL fitter is provided the hit coordinates as the projection matrix from equation (7.23), the residual vector in the measurement system from equation (7.21) and the precision vector from (7.22) for each hit.

7.2.3 Linear Track Model

Within the context of this thesis, only straight tracks are considered. The GBL fit, when applied for real data, is only applied to data taken with the magnet switched off, hence with straight muon tracks. The model used for straight tracks is described in the following.

The parametrization of the track model is one of very few things that GBL specifies. A three dimensional track is described with a set of five parameters $\mathcal{P}$:

$$\mathcal{P} = \left(\frac{q}{p}, \frac{dx}{dz}, \frac{dy}{dz}, x_0, y_0\right) \tag{7.24}$$

In particular, these are a *curvature* of the track, two *slopes* and two *offset coordinates*. The coordinate system, in which these parameters are expressed can be freely chosen by the user, some coordinate systems might however be better suited for a particular problem, than others.

For the experimental setup described here, the following set of parameters shown in (7.24) was used. Here, $\frac{q}{p}$ with charge q and momentum p is the curvature of the track. Since only straight tracks are considered, in the following

$$\frac{q}{p} = 0$$

is used for all tracks. Since the beam direction is parallel to the z-direction, the slopes are here used in the x- and y-directions as $\frac{dx}{dz}$ and $\frac{dy}{dz}$ respectively. The offsets x_0 and y_0

are the coordinates of the track at any fixed z, for example a track extrapolation to $z = 0$ can be used.

7.2.4 Jacobi Matrix

The GBL fitting algorithm fits the track model to a set of *GblPoints* that a *GblTrajectory* consists of. Each GblPoint represents a measurement, thus in the context of this thesis, a drift tube hit. At each point, a *Jacobi matrix* needs to be provided that describes the propagation of the track parameters from one point to another. It contains the partial derivatives of each track parameter at point i on the track with respect to all parameters at point j. The definition of the Jacobian is shown in (7.25).

$$J_{ij}^{nm} = \frac{\partial \mathcal{P}_n}{\partial \mathcal{P}_m} \tag{7.25}$$

When applied to the linear track model shown in (7.24), the derivatives of the track parameters with respect to themselves are all constant, as they do not change from hit to hit.

For the linear track model used in this thesis, with the beam direction being the z direction, the only parameters changing from point i to point j on the track are the local offsets of the track at those points. Hence, from now on the following constraints are used:

$$\frac{dx}{dz} = const$$
$$\frac{dy}{dz} = const.$$

The track offsets x_j and y_j at point j can be calculated from the respective parameters at point $i = j - 1$ as:

$$x_j = x_i + \frac{dx}{dz}\Delta z_{ij} \tag{7.26}$$
$$y_j = y_i + \frac{dy}{dz}\Delta z_{ij} \tag{7.27}$$

Now, the respective values for the Jacobian can be calculated by the partial derivative with respect to the slopes, which is shown in (7.28) and (7.29).

$$\frac{\partial x_j}{\partial \left(\frac{dx}{dz}\right)} = \Delta z_{ij} \tag{7.28}$$
$$\frac{\partial y_j}{\partial \left(\frac{dy}{dz}\right)} = \Delta z_{ij} \tag{7.29}$$

Using (7.28) and (7.29) now in (7.25), the Jacobian that is used within this thesis is:

$$J_{ij} = \begin{pmatrix} 1 & 0 & 0 & 0 & 0 \\ 0 & 1 & 0 & 0 & 0 \\ 0 & 0 & 1 & 0 & 0 \\ 0 & \Delta z_{ij} & 0 & 1 & 0 \\ 0 & 0 & \Delta z_{ij} & 0 & 1 \end{pmatrix} \tag{7.30}$$

7.3 Pede Alignment

The track based alignment of the detector is performed using the standalone program *pede*, which is part of the Millepede package [109]. The so called *mille binary files* created in the process of the GBL track fit are then refitted globally using *pede* [110]. Using labels for the detector components, the user can define groups of the detector that are aligned as a single detector part. For each hit of any drift tube in the process of fitting, a set of *global derivatives* is calculated and written to the mille binary file by GBL. These global derivatives are not used for the track fit but only for the alignment by *pede*. The alignment process is described in the following.

7.3.1 Global Derivatives

When a track is fitted to a set of hits, a *prediction* $\mathbf{p}(x_p, y_p, z_p)$ of the measurement can be calculated. In case of a drift tube detector, this prediction is the shortest distance vector from the wire to the track.

A *measurement* $\tilde{m}$, in general, differs from the prediction. One contribution to the difference between prediction and measurement is the inherent precision of the detector. For a drift tube, this is for example limited by the primary ionization statistics, resolution of the drift time measurement or diffusion of the electron cloud in the tube. Would the exact coordinates of each tube that was hit be perfectly known, these physical limits on the drift tube performance explained the residuals. For a real detector however, the exact positions of each detector component (e.g drift tube) are not known to a perfect precision. In the specific case of the drift tube spectrometer described here, an assumed position can be calculated from the survey measurement for each drift tube.

For a prediction $\mathbf{p}(x_p, y_p, z_p)$, small displacements $(\Delta x, \Delta y, \Delta z)$ and rotations (α, β, γ) result in a distorted measurement $\tilde{m}$:

$$\tilde{m} = m + \begin{pmatrix} \Delta x \\ \Delta y \\ \Delta z \end{pmatrix} + \alpha \begin{pmatrix} 0 \\ -z_p \\ y_p \end{pmatrix} + \beta \begin{pmatrix} z_p \\ 0 \\ -x_p \end{pmatrix} + \gamma \begin{pmatrix} -y_p \\ x_p \\ 0 \end{pmatrix} \tag{7.31}$$

Here, m is the measurement vector of a tube that is only disturbed by inherent inaccuracies of the tube itself.

Another contribution to the difference between measurement and prediction is the offset of assumed and real coordinates of each detector component. The two contributions to the residual described before can now be separated. The first contribution (ionization statistics, diffusion etc.) can not be predicted and is different for each hit. The second contribution, small translations and rotations of the real detector coordinates with respect to the assumed ones, are the same for every hit of a specific drift tube. Therefore, in the context of *pede* alignment, the small translations and rotations are called *global parameters*. These are summarized in a global parameters vector $\vec{g}$:

$$\vec{g} = \begin{pmatrix} \Delta x \\ \Delta y \\ \Delta z \\ \alpha \\ \beta \\ \gamma \end{pmatrix} \tag{7.32}$$

When the dependence of the residuals of the global parameters $\vec{g}$ is known, these parameters can be optimized in order to minimize the residuals. This dependence is described by the derivative shown in equation (7.33).

$$\frac{\partial \vec{r}}{\partial \vec{g}} = \frac{\partial \vec{r}}{\partial \tilde{m}} \cdot \frac{\partial \tilde{m}}{\partial \vec{g}} \tag{7.33}$$

The residual $\vec{r}$ in equation (7.33) that *pede* uses is the residual of the fit performed using the GBL algorithm. As the GBL fit is performed in a reference frame where the measurement is always along the positive x-axis, a different reference frame must be used for alignment that is the same for each hit but can differ for each tube. Here, for each tube, a reference frame is chosen where the y-axis is parallel to the sense wire and the z-direction is the beam direction, thus parallel to the global z-direction.

So when the measurement prediction $\mathbf{p}(x_p, y_p, z_p)$ and the global parameters are given in the alignment system, marked by index a but the residuals are given in the measurement system, marked by index m, the derivative in equation (7.33) needs to be adjusted as shown in equation (7.34).

$$\frac{\partial \vec{r}_m}{\partial \vec{g}} = \frac{\partial \vec{r}_m}{\partial \vec{r}_a} \cdot \frac{\partial \vec{r}_a}{\partial \tilde{m}} \cdot \frac{\partial \tilde{m}}{\partial \vec{g}} \tag{7.34}$$

The residual $\vec{r}_m$ in the alignment system can be calculated from the residual $\vec{r}_a$ in the measurement system by

$$\vec{r}_m = R \cdot \vec{r}_a,$$

where R is the rotational matrix rotating a vector from the alignment to the measurement system. This matrix R is calculated from the known rotations from global coordinates to the measurement system M and the rotation from global coordinates to the alignment

system[4] A:

$$R = A \cdot M^{-1} \tag{7.35}$$

The partial derivative $\frac{\partial \vec{r}_m}{\partial \vec{r}_a}$ can now be written as:

$$\frac{\partial \vec{r}_m}{\partial \vec{r}_a} = A \cdot M^{-1}.$$

The term $\frac{\partial \tilde{m}}{\partial g}$ in equation (7.34) is:

$$\frac{\partial \tilde{m}}{\partial \vec{g}} = \begin{pmatrix} 1 & 0 & 0 & 0 & z_p & -y_p \\ 0 & 1 & 0 & -z_p & 0 & x_p \\ 0 & 0 & 1 & y_p & -x_p & 0 \end{pmatrix} \tag{7.36}$$

The derivative $\frac{\partial \vec{r}}{\partial \tilde{m}}$ in equation (7.34) can be written as:

$$\frac{\partial \vec{r}}{\partial \tilde{m}} = \frac{\partial \left(\tilde{m} - \vec{p}\right)}{\partial \tilde{m}} = \mathbb{1} - \left(\frac{\vec{d} \cdot \vec{n}^t}{\vec{d} \cdot \vec{n}}\right) = \left(\delta_{ij} - \frac{d_i n_j}{\vec{d} \cdot \vec{n}}\right) \tag{7.37}$$

Since all drift tube planes are in the xy-plane, the normal $\vec{n}$ is parallel to the z-axis for all hits. Using this in equation (7.37), the term $\frac{\partial \vec{r}}{\partial \tilde{m}}$ can be written as:

$$\frac{\partial \vec{r}}{\partial \tilde{m}} = \begin{pmatrix} 1 & 0 & -\frac{d_x}{d_z} \\ 0 & 1 & -\frac{d_y}{d_z} \\ 0 & 0 & 0 \end{pmatrix} \tag{7.38}$$

Using (7.38) and (7.36) in (7.33) now yields the 3×6 matrix describing the relation between residuals and the global parameters which is provided to the GBL points. The *alignment* now is performed by minimizing the residuals through an alteration of the global parameters translation and rotation for a given set of labels.

7.3.2 Labels

The drift tube spectrometer described in this thesis is built from drift tube modules[5]. The spectrometer stations T3 and T4 are then built out of four of these modules next to each other. The precision that individual modules are built with is considered much higher than the accuracy of placing the modules next to each other with minimal gaps in between and higher than the optical survey measurement. Hence, a first step would be to align the relative positions and rotations of whole drift tube modules.

[4] See chapter 7.3.3
[5] See section 6.1.

In a second step, individual drift tubes can be aligned. By mounting the drift tube modules to the mounting frame, torsion forces can be applied to the module, which are considered smaller in magnitude than the misalignment of whole modules. However, they can have a similar magnitude as the spatial resolution of the tube, thus correction of this misalignment might be beneficial.

For the alignment, the derivatives of the residual are calculated with respect to the six global parameters, being three translations and three rotations. For each hit, the global derivatives are calculated and stored alongside a list of *labels* for that hit. These labels must be unique for each *alignable* unit. Each of these units then has six labels, one for each global parameter. For the case of module-wise alignment, the labels are four-digit numbers. Here, the first digit describes the station, a module is part of. The second digit accounts for the stereo view of stations T1 and T2. The third digit increases for the drift tube modules that are placed next to each other in stations T3 and T4. The last digit runs from one through six and accounts for the six global parameters.

Tables showing a decoding of the labels are presented in tables B.1 through B.3 in the appendix.

7.3.3 Alignment Reference Frames

The alignment can be performed in any reference frame. A typical choice is the global reference frame. Here, the application of the alignment parameters is particularly simple but for the alignment constraints might be needed in order to calculate correct values. In the context of this thesis, an alignment system was chosen that is unique to each *alignable detector part*. In a first step, whole modules of drift tubes are aligned. So, each drift tube module has its own alignment system. This system has its origin in the geometrical center of the module itself. The local y'-axis is parallel to the sense wires, the local z'-axis is parallel to the beam axis, which is also the global z-axis. Hence, the local x'-axis is parallel to the global x-axis for all modules as well, except for the two modules rotated around the beam axis with a stereo angle in order to be able to perform a three dimensional track fit. In case of aligning individual tubes, the reference frame has its origin in the wire's center with the local y' direction in the wire direction and the local z' direction parallel to the beam direction.

7.4 Application of the Alignment Results

The alignment results are summarized in a textfile created by the program pede. Here, for each defined label, a correction is given. These are in particular three *incremental*, rotational corrections α, β and γ and three translations Δx, Δy and Δz.

From the rotation corrections α, β and γ, a rotational correction matrix ΔR can be

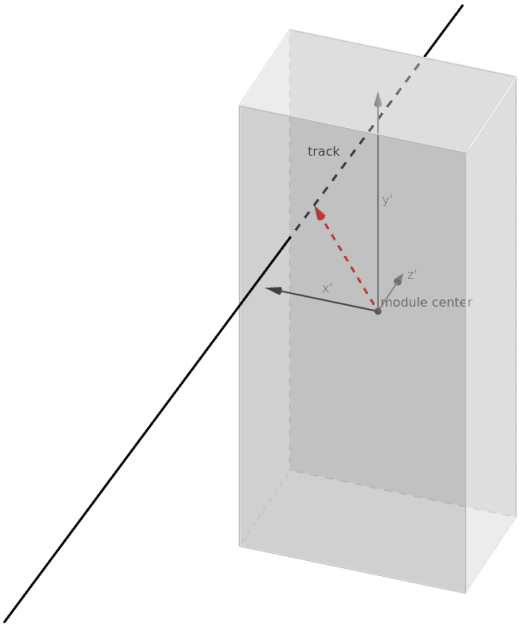

Figure 7.2: Illustration of the reference frame for module alignment. A drift tube module is illustrated as a grey box for simplification. The modules geometric center is the origin of the alignment system. The *measurement prediction* (red vector) for a tube in the module that was hit by a track (black line) can be calculated as the vector from the system's origin to the point of closest approach on the track (calculation explained in chapter 7.3.3). The measurement prediction is used for *pede* alignment in equation (7.36).

calculated as [110]:

$$\Delta R = R_\alpha R_\beta R_\gamma \approx \begin{pmatrix} 1 & \gamma & -\beta \\ -\gamma & 1 & \alpha \\ \beta & -\alpha & 1 \end{pmatrix} \tag{7.39}$$

So when applying a rotation, aligned the detector element is first rotated by α around its local x'-axis, then by β around the new local y'-axis and finally by γ around the new z'-axis.

Note that equation (7.39) is an approximation, which is sufficient for small angles α, β and γ [110]. In case, an alignment results in corrections so large that this approximation is not sufficiently accurate anymore, this rotation can be applied either way but then, additional alignment iterations are needed, potentially resulting in smaller corrections to the prior result.

For the rotations, the term incremental means that a detector element, whose nominal, local reference frame is already rotated with respect to the global reference frame with a

rotation matrix R, is after alignment rotated by

$$R \to \Delta R R.$$

The corrections $\Delta\vec{r} = (\Delta x, \Delta y, \Delta z)$ transform to the local reference frame translation $\Delta\vec{q}$ as [110]

$$\Delta\vec{q} = \Delta R R \Delta\vec{r}. \tag{7.40}$$

Now for each hit, an aligned transformation from global to local coordinates can be given as [110]:

$$\vec{q}_{\text{aligned}} = \Delta R R(\vec{r} - \vec{r_0}) + \Delta\vec{q} \tag{7.41}$$

In equation (7.41), $\vec{r}$ is the position of a hit in global coordinates and $\vec{r_0}$ is the origin of the local reference frame of the hit detector element in global coordinates. The minimization algorithm is described in detail in [110].

8 Toy Monte Carlo Tracks

In order to test the GBL fitter, a simple toy Monte Carlo (*MC*) simulation was created. Here, for each fitted track the truth is known and the performance of the fit can be checked by comparing the fitted result to the truth. The term *toy* indicates that it uses a rather simple model and neglects effects like scattering of tracks within the detector material or detector efficiency. This simulation is only intended to test the performance of the fitting algorithm itself. Note that the SHiP software framework FairShip contains a full Monte Carlo simulation taking all these effects into account. However, for this purpose, a simpler and faster to compute simulation is sufficient.

The toy MC tracks (from now on MC) are generated in two different setups, one with a uniform distribution of track slopes $\frac{dx}{dz}$ and $\frac{dy}{dz}$ and a second setup with a forward boosted distribution, to check the dependence of the fit- and alignment performance on the slope distribution, hence the *spectrum*.

8.1 Track and Hit Generation

The generation of tracks and hits from the MC are separate processes. This section describes the process of creating both tracks and hits as well as options that are available for the generation.

8.1.1 Random Number Generation

The pseudo random numbers for this method were created with a *Mersenne Twister Generator*, specifically the generator MT19937 [113], as it is implemented in the C++ language standard library. This generator only fails two tests for random number quality in the *TestU01* framework [114] but offers a good compromise with computation time. Failing two tests of the stringent TestU01 framework can be considered a good result. Especially, since in this context no physical interactions are taken into account and the random numbers are only used to generate two points in a three dimensional space for each track, the random number generator can be considered sufficient for this task. Its periodicity of $P = 2^{(624-1)\cdot 32} - 1 \approx 2 \cdot 10^{6001}$ allows the generation of practically any number of unique MC tracks. The random number generator has an internal state that is held throughout the program run time to ensure that all random numbers drawn for each track and each hit follow a pseudo random sequence, that is well tested.

8.1.2 Track Generation

The track generation is based on the generation of *two points* on the track. One of these points is directly upstream of the very first drift tube module of station T1, the other point is directly upstream of the station T4[1]

For this purpose, two planes, each at a constant z are defined. One plane is upstream of station T1, the other one upstream of station T4. In each of these planes, x- and y-offsets are drawn as uniformly distributed random numbers, so using the z-coordinate from the planes the offsets are drawn at, two points $\vec{p}_1$ and $\vec{p}_2$ on the track are generated. Information stored for one MC track is the point upstream of T1 and the direction $\vec{t}$ of the track, which is:

$$\vec{t} = \vec{p}_2 - \vec{p}_1$$

For these tracks, no physical interactions with the detector material are simulated. Based on these MC tracks, MC hits can be generated. The normalized distribution of slopes $\frac{dx}{dz}$ is shown in figure 8.1.

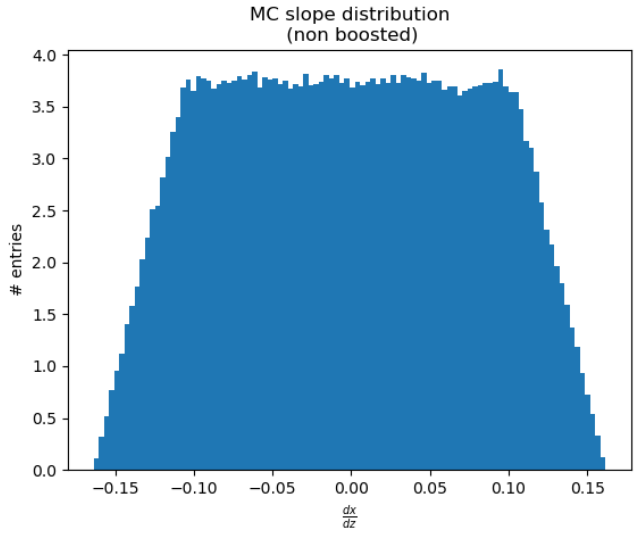

Figure 8.1: Distribution of slopes $\frac{dx}{dz}$ in the x-direction. The distribution is normalized to $\sum = \frac{1}{\text{binwidth}} \approx 307$. It shows a flat distribution with linear tails towards both ends. The tails are due to the uniform distribution of generated points the tracks start at.

8.1.3 Hit Generation

The hit generation for a given MC track is performed so that the hits fit the detector position as measured by the survey measurement. For each tube in the detector, the distance from the sense wire to the MC track is calculated. If this distance is smaller than

[1]For a detector description see chapter 5.2 and for the naming convention of the drift tube stations and modules in particular figure B.1 on page 173.

one drift tube's radius of 1.815 cm, a hit is generated. This hit consists of a numerical identifier (*ID*) of the tube as well as the drift radius. While for real data, the distance is calculated from a *time measurement* using the *rt*-relation, which itself comes with errors, for the MC hits an unsmeared distance d_{clean} from wire to track is stored. Additionally, the hits are smeared to simulate the spatial resolution of a drift tube. The smeared drift radius is stored alongside the unsmeared distance in order to test the performance of the fit. Note that for the fitting, only smeared hits are used.

Therefore, after a list of clean hits was generated for a track as described above, each hit is smeared with a Gaussian distributed uncertainty. This is done by drawing a Gaussian distributed random number δd, where the distribution is centered at zero with a width of $\sigma = 350\,\mu\text{m}$. Finally, the smeared hit radius d_{smeared} is stored for each hit, which is calculated as

$$d_{\text{smeared}} = |d_{\text{clean}} + \delta d|.$$

In addition, during hit generation, misalignment of the detector can be simulated. The user can pass a list of drift tube IDs to the hit generator for which a misalignment should be applied. Thereby, any set of drift tubes can be translated and rotated by user chosen amounts[2]. The hit generation then generates hits for the *new* position of these tubes. After the hit generation, the applied misalignment is forgotten and the assumed position of the tubes as implemented in the FairShip Software framework is used again for track fitting.

Note that the MC hits do not take inefficiencies of drift tubes into account. After the hit generation, optional cuts can be applied, for example to reject MC tracks with less than a given number of hits.

8.2 GBL Fit of MC Tracks

In order to test the GBL track fit for the setup described in this thesis, a track fit of the MC tracks using the GBL fit is performed. Therefore, the MC tracks are used as seed, from which the residuals provided to the GBL fitter are calculated.

First, the detector layout is unaltered from the survey measurements, hence no misalignment is introduced and $N = 10^5$ tracks were generated and fitted. A first test is based on the χ^2-distribution of the fit. For a good fit of many tracks, the distribution of the χ^2-probability is expected to show a uniform distribution with a mean value of 0.5. The χ^2-probability calculated for the GBL fit of MC tracks is shown in figure 8.2. The plot of the χ^2-probability shows the expected, uniform distribution with a mean of 0.499 ± 0.001. Another test of the fitting method is to check if the residuals of the fit

[2]Here, for any linear combination of translations, the wire directions remain constant. Rotations on the other hand keep the origin of the tube's alignment reference frame in place and change the direction of each wire. Note that if drift tube modules are aligned and the module's geometric center is the origin, the center position of a single drift tube does change due to rotations around the module center.

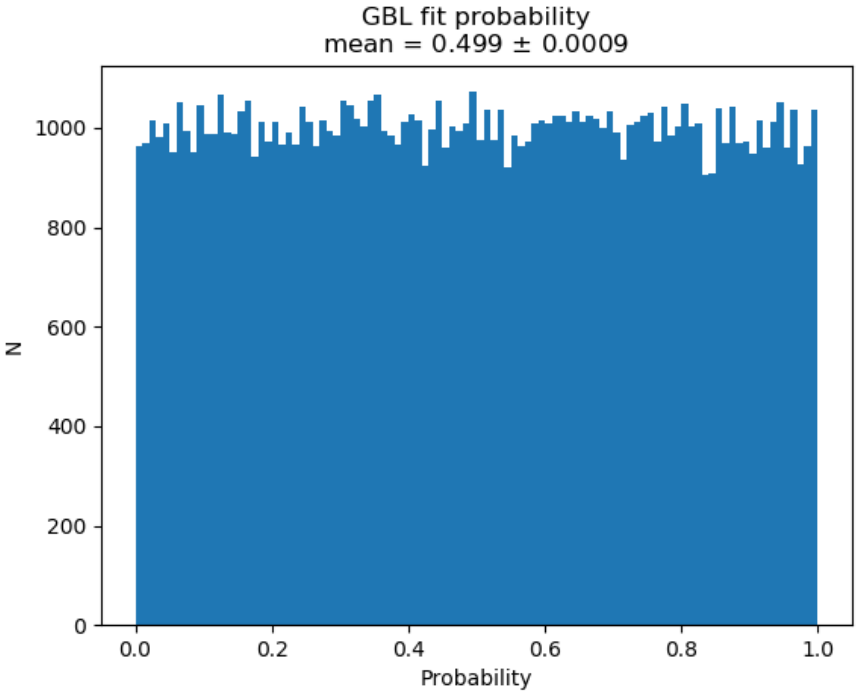

Figure 8.2: Distribution of the χ^2 probabilities for 10^5 tracks generated with the toy MC. The mean of the distribution is around 0.5 which hints to a fit to the correct model.

represent the width of the Gaussian distribution the hits were smeared with. A plot of the residual distribution after performing the GBL fit is shown in figure 8.3. The fitted track is expected to be reasonably close to the *real* (unsmeared) hit distance, given the track is fitted to a sufficient number of hits. The residuals then follow the distribution of the hit smearing, which can be seen in figure 8.3. Therefore, the fit is considered to use a model describing the data and find a reasonable track. The latter point is further analyzed in section 8.2.1 by comparing fitted tracks to the MC truth.

8.2.1 Comparison with MC Truth

To further test the fit quality, the fitted GBL tracks are compared with the MC truth. Therefore, the deviation angle to the slopes, both in x- and y-directions are calculated. In particular, the slopes $\frac{dx}{dz}$ and $\frac{dy}{dz}$ of the fitted GBL track are compared with the according values of the MC truth. These slopes are native parameters to the linear track model used for fitting[3] the tracks and are directly accessible after the fit. The deviation between the fitted tracks and MC truth is calculated using

$$\Delta\alpha = \left(\frac{dx}{dz}\right)_{\text{fit}} - \left(\frac{dx}{dz}\right)_{\text{truth}} \tag{8.1}$$

$$\Delta\beta = \left(\frac{dy}{dz}\right)_{\text{fit}} - \left(\frac{dy}{dz}\right)_{\text{truth}}. \tag{8.2}$$

[3]Shown in equation (7.24).

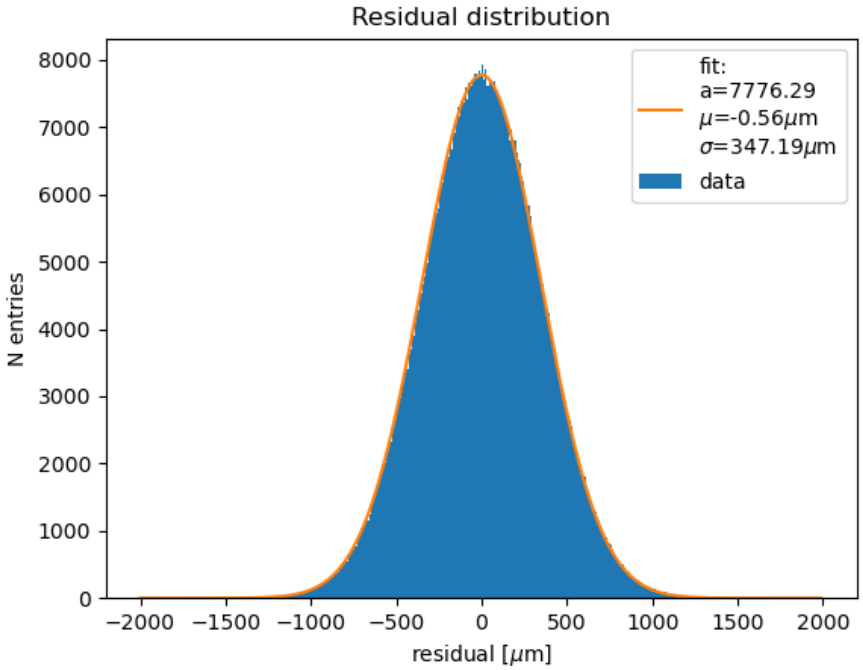

Figure 8.3: Residual distribution of the GBL fitted MC tracks for $N = 10^5$ tracks. This represents the Gaussian distribution the simulated hits were smeared with. This is used as a test if the GBL fit finds correct tracks. The parameters of the fitted Gaussian function are the height a, the mean value μ and the width σ.

These slopes can be converted to angular deviations via

$$\Delta\alpha_{\text{deg}} = \frac{180^\circ}{\pi} \tan^{-1}(\Delta\alpha) \tag{8.3}$$

$$\Delta\beta_{\text{deg}} = \frac{180^\circ}{\pi} \tan^{-1}(\Delta\beta). \tag{8.4}$$

These deviations were calculated for $N = 5 \times 10^5$ MC tracks. Histograms, showing the deviations in x- and y directions are shown in figure 8.4. It can be seen that the deviation from the MC truth in x direction is much smaller than in the y direction. This can be explained with the smaller number of hits contributing to a measurement of the y coordinate, as only two modules of drift tube are rotated with a stereo angle, offering a sensitivity to y. From a Gaussian fit of the distributions, the width σ is calculated, resulting in the values

$$\sigma_x = (0.052 \pm 6.7 \cdot 10^{-5})^\circ$$

$$\sigma_y = (0.822 \pm 0.004)^\circ.$$

It would be expected that the fit would reproduce the MC truth tracks which would show in sharp peaks at zero for both x- and y-slopes. The MC truth however is smeared at

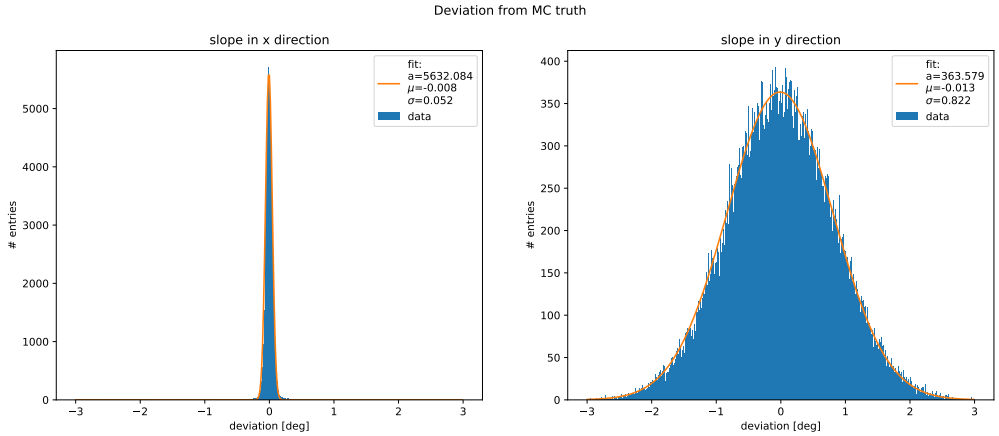

Figure 8.4: Difference in slope angles between fitted track and MC truth. The deviation from the MC truth for the slope in x direction is shown on the left side and for the y direction on the right side. The wider distribution for the slope in y direction is expected since only two modules of drift tubes are rotated with a stereo angle and, due to track selection, a maximum of eight hits per track can be used to determine the y coordinates. The angles are calculated using equations (8.3) and (8.4). The parameters of the fitted Gaussian functions are the height a, the mean value μ and the width σ.

each hit with a 350 µm wide Gaussian distribution, hence deviations different from zero can be explained.

The distributions are centered around zero showing no systematic errors in the fitting algorithm, the width of the distributions of slope deviations can be considered the angular resolution assuming only Gaussian hit smearing.

8.3 Alignment

In order to test the alignment procedure, MC tracks and corresponding hits were generated for an artificially misaligned detector geometry. Three misaligned setups were tested, in particular these are a purely *translational* misalignment and a purely *rotational* misalignment. Last, an artificial misalignment was tested where the detector was both translated and rotated from its nominal position. These test cases were performed with whole modules of drift tubes misaligned as a unit.

In case of a translational misalignment, the hits for a given track were generated fitting a detector geometry where all modules of stations T3 and T4 were shifted by the constant vector

$$\vec{t} = \begin{pmatrix} -0.5 \\ 0 \\ -0.2 \end{pmatrix} \text{ cm}. \tag{8.5}$$

In case of a rotational misalignment, all the modules of station T3 were rotated around

the z-axis by an angle $\gamma = 0.5° \approx 8.7\,\text{mrad}$. The modules were rotated in their geometric center positions which equals to their local alignment reference frames' origins.

After the hit generation, the MC tracks are fitted using the GBL fitter assuming an undistorted detector geometry so not using knowledge about the artificial misalignment. After fitting, the produced alignment data is fitted using the *pede* program. In case of the translation alignment, the corrections calculated by *pede* were applied and the same set of MC tracks was fitted again in the misaligned and then corrected detector geometry to examine the effect of the alignment on the spectrometer resolution.

At last, the translational alignment was tested again with another set of MC tracks, where the tracks were generated simulating a *forward boosted* situation which more closely resembles the track distribution expected for a fixed target experiment with 400 GeV/c protons.

For all cases, the coordinates of both drift tube modules of station T1 were *fixed* so that they can be used a reference for the alignment.

8.3.1 Alignment Reference

In principle, by applying a global translation or rotation on all detector elements would not change the fitted track at all. Hence, the alignment corrections for any alignable detector component[4] are calculated with respect to a *fixed* reference component. For all the alignment results presented within this thesis, the alignment reference is the module T1X, hence the most upstream drift tube module. Its sense wires are (nominally) oriented such that they run in parallel to the global y-axis, hence this drift tube module is not sensitive in the y-direction. This would result in arbitrary corrections that could be applied in terms of translations in the y direction. To account for this, of the first stereo module T1V, the correction in its local x direction[5] is fixed as well. Additionally, all drift tube modules are constrained such that they can not be translated along their sense wire axes, which would again not change the fit results. This would only result in lower efficiency since the GBL fit implemented here treats the drift tubes as infinitely long.

Additional constrains can be applied for the alignment corrections. If for a specific alignment setup, constrains are used, they are introduced for this context.

8.3.2 Residual Asymmetry

For a misaligned detector, the residuals for tracks passing on either side of the drift tube are asymmetric. To demonstrate this, MC tracks were fitted in the detector geometry with the translational misalignment applied as shown in equation (8.5). So the *true* position is offset in the $-x$ direction from the *assumed* position used for track fitting. Now, a histogram of the residuals only from the misaligned modules is shown in figure 8.5. When

[4] First whole drift tube modules, later single drift tubes or any arbitrary subset of drift tubes
[5] In the alignment system, this is perpendicular to both the wire- and the global z-direction.

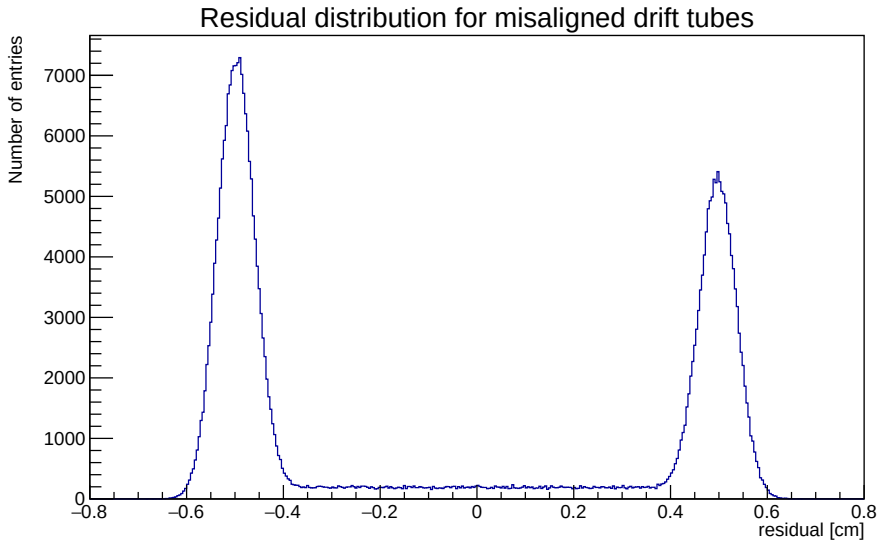

Figure 8.5: Residual distribution for the misaligned drift tube modules calculated with MC tracks. For the MC, the detector walls T3 and T4 were misaligned by $\Delta x = -0.5\,\text{cm}$. This shows two peaks at $\pm\Delta x$, depending on which side of the assumed tube position the track passed.

the residual distribution of the misaligned modules is plotted only for tracks passing the sense wire at the $-x$ or $+x$ direction respectively, the distributions shown in figure 8.6 can be seen.

The asymmetry can be understood by looking at the direction of the residual vector for tracks passing at different locations, which is illustrated in figure 8.7. Here, the sign of the residual vector changes for tracks passing in between the assumed and the real position of a drift tube which results in an asymmetric residual distribution.

By rejecting hits where the track passes the assumed wire position at the side pointing towards the *real* position of the wire, so here the $-x$ direction at a distance smaller than the measured drift radius, the residual distribution changes to the one shown in figure 8.8. Here, the tail towards positive residuals for tracks passing on the negative drift side disappeared and the two Gaussian peaks are equal in width and centered at equal distances. The *pede* program for calculating the alignment corrections needs symmetric residual distributions in order to work properly. By rejecting hits where the distance between seed track and sense wire is smaller than the measured drift distance, a symmetric distribution can be achieved. When applied to real data instead of MC, the direction towards the *real tube location* is unknown, hence all hits where the track distance is smaller than the measured drift radius must be rejected. This, however, reduces the number of hits usable for alignment, resulting in a larger statistic uncertainty.

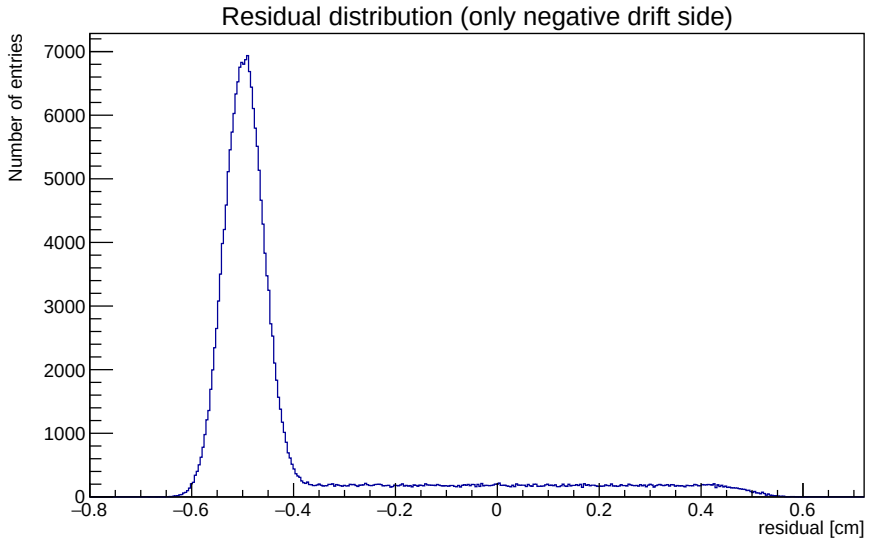

(a) only tracks passing on the $-x$ side of the wire

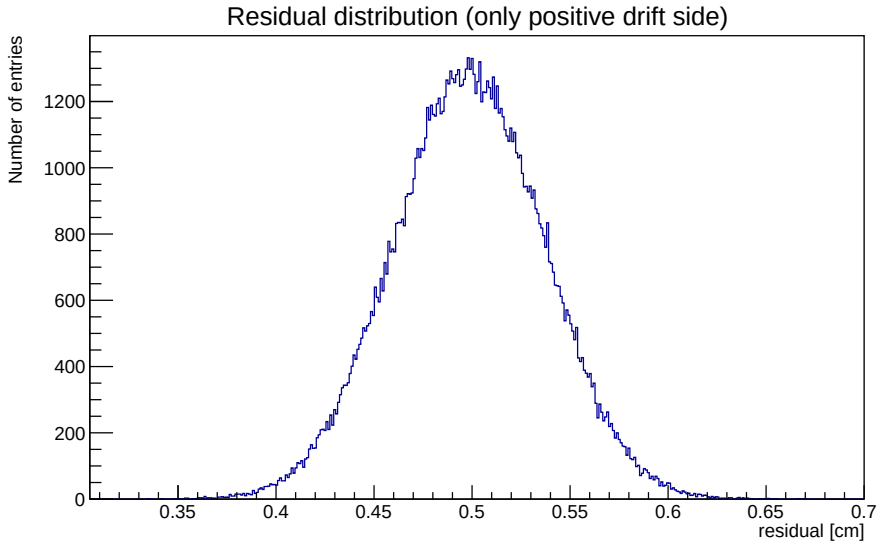

(b) only tracks passing on the $+x$ side of the wire

Figure 8.6: Residuals for misaligned drift tube modules.

8.3.3 Translational Alignment

A first test of the alignment procedure was performed using the translational misaligned MC data. The cut on distances between track and sense wire motivated in section 8.3.2 was applied. The alignment parameters were calculated for whole modules of drift tubes. For each parameter label[6], a correction is calculated. Hence, for each drift tube module, corrections to all six alignment parameters, introduced in equation (7.32), are calculated. These are three translation directions and three rotation angles. Since in this case, misalignment of the detector was performed using only translations, rotations are not shown

[6]See section 7.3.2.

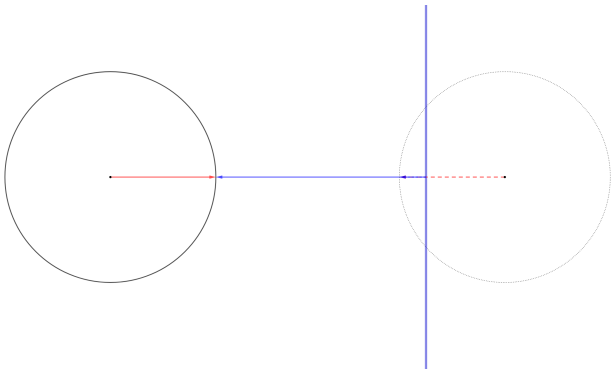

(a) Track within assumed drift circle

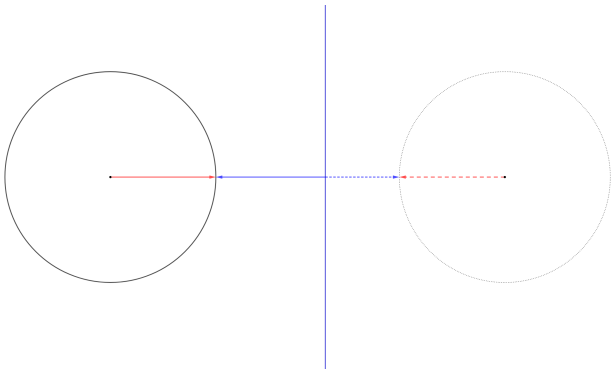

(b) Track between assumed and true drift circle

Figure 8.7: A track (solid blue) passing a drift tube. In this example, the true position of the sense wire is on the left side of the track. The drift circle measured at the true position of the tube is shown as the solid circle. Due to misalignment, the tube is *assumed* to be on the right side of the track, the measured drift circle at the assumed position is shown as dashed circle. The residual vector (blue vector) points from the track to the measurement (drift circle). When the track passes in between the true and assumed position but closer to the assumed tube than the radius of the drift circle the residual points towards the assumed sense wire, shown in (a). If the distance of the track increases and the track is in between the true and assumed *drift circle*, the residual vector changes direction, as shown in (b) and points to the opposite direction of the *real residual*.

here. However, the alignment algorithm calculates rotational corrections compatible with zero in case no rotational misalignment was applied.

The corrections calculated using the *pede* program are shown in figure 8.9 for station T3 and in figure 8.10 for station T4.

It can be seen that corrections calculated using the *pede* alignment algorithm are close to the *real* correction using knowledge from the MC truth (shown as red dashed line). The alignment process can be repeated as an iterative process, possibly enhancing the alignment results. Here, the corrections calculated without iterating were sufficient to reproduce the expected residual distribution as presented in the following.

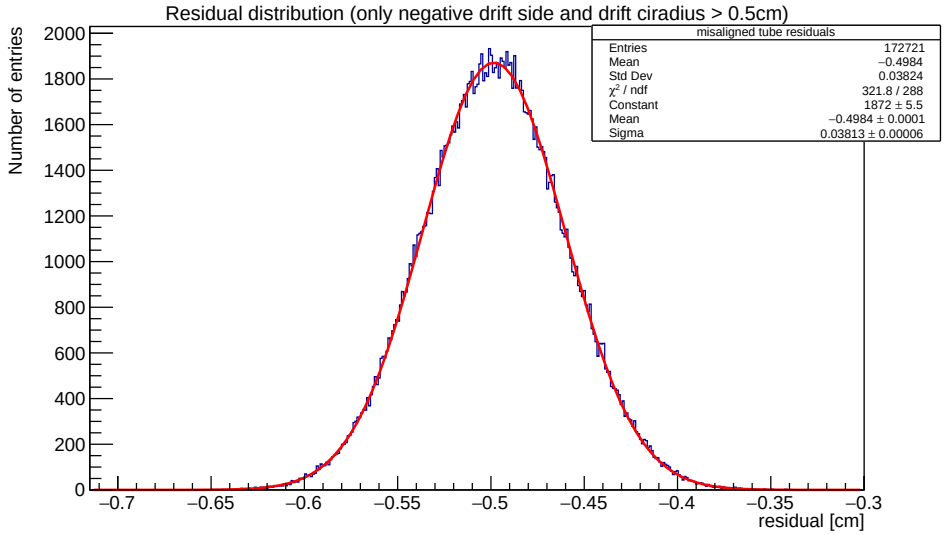

(a) only tracks passing on the $-x$ side of the wire

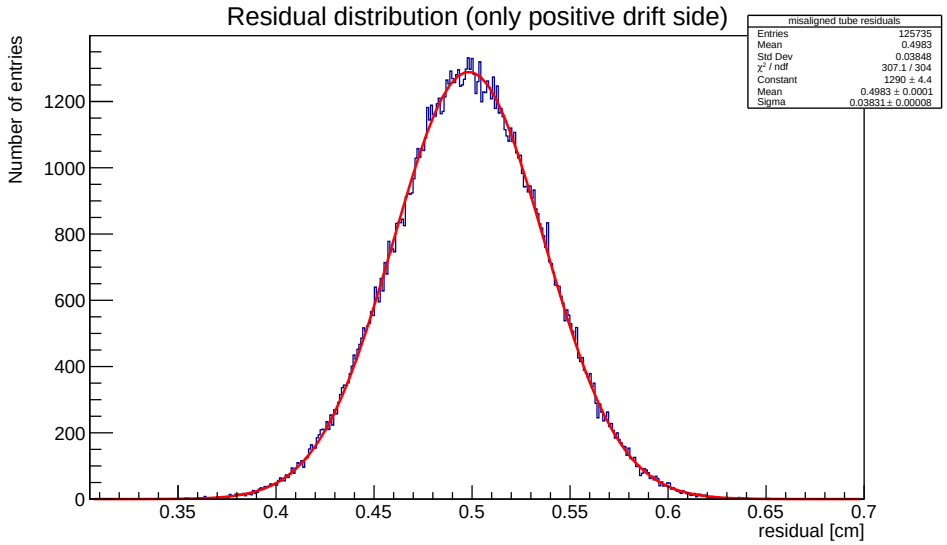

(b) only tracks passing on the $+x$ side of the wire

Figure 8.8: Residuals for misaligned drift tube modules with hits passing in between assumed and real position of the tube at a distance smaller than the drift radius rejected.

8.3.4 Residual Improvements

After calculating the corrections to the translational misalignment using pede[7], these were applied to the detector geometry. Then another, smaller set of $N = 5 \cdot 10^4$ tracks was simulated and fitted using GBL in the corrected detector geometry.

A comparison of the residual distributions both for the misaligned and the aligned detector setup are shown in figure 8.11. In figure 8.11(a), the residual distribution is

[7]Presented in section 8.3.3.

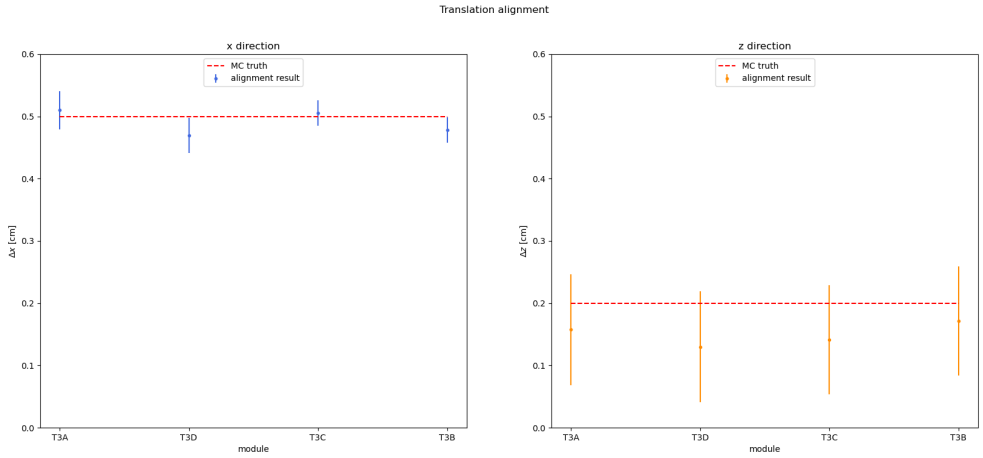

Figure 8.9: Correction for translational misalignment of drift tube station T3, calculated using the *pede* software. The residuals that were minimized by *pede* were calculated from GBL fitted MC tracks. A total of $5 \cdot 10^5$ tracks were fitted in a detector artificially misaligned by $\Delta x = -0.5\,\text{cm}$ and $\Delta z = -0.2\,\text{cm}$. The left plot shows the corrections in the x direction, the right plot for the z direction. The MC truth is indicated by dashed red lines. As corrections, they have a sign opposite to the detector misalignment.

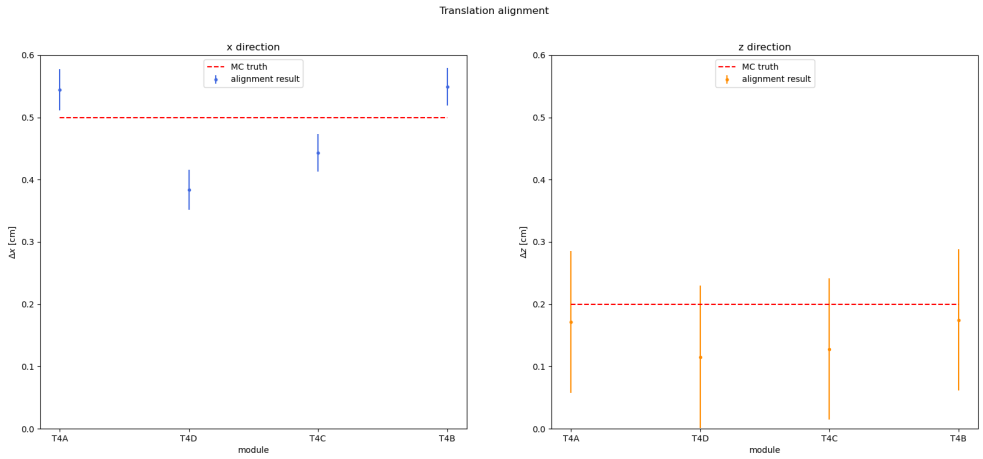

Figure 8.10: Correction for translational misalignment of drift tube station T4, calculated using the *pede* software. The residuals that were minimized by *pede* were calculated from GBL fitted MC tracks. A total of $5 \cdot 10^5$ tracks were fitted in a detector artificially misaligned by $\Delta x = -0.5\,\text{cm}$ and $\Delta z = -0.2\,\text{cm}$. The left plot shows the corrections in the x direction, the right plot for the z direction. The MC truth is indicated by dashed red lines. As corrections, they have a sign opposite to the detector misalignment.

wider than the width of the hit smearing, which results in a decreased spatial resolution due to the misalignment. After the alignment procedure (figure 8.11(b)), the residual distribution shows a width of $\sim 350\,\mu\text{m}$, which is the smearing width of the MC hits. Therefore, a single step of alignment is considered sufficient for the setup used in this

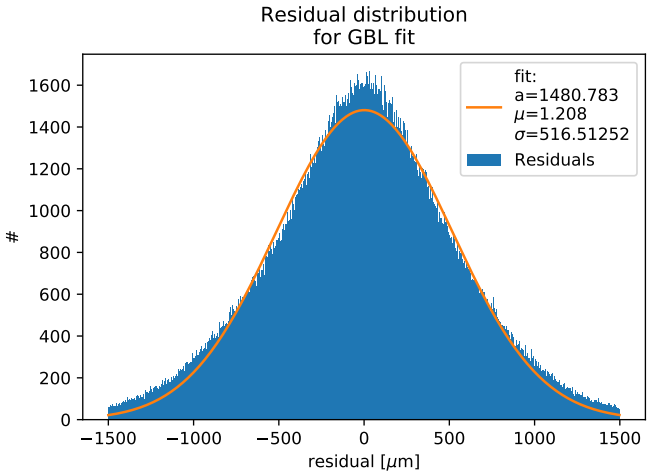

(a) initial setup

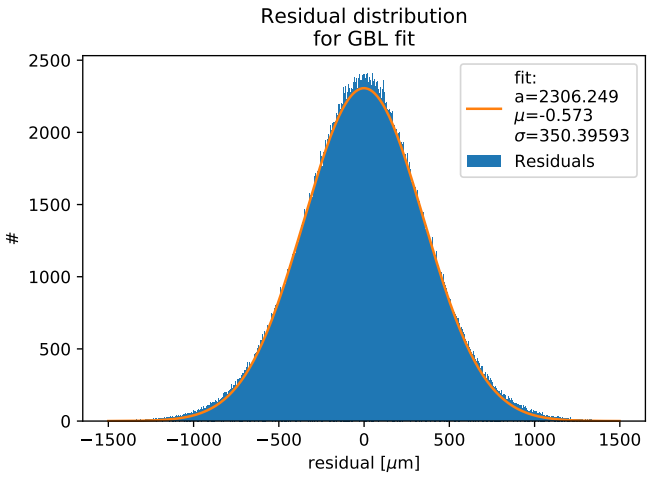

(b) aligned detector

Figure 8.11: Residual distribution for the track fitted using the GBL algorithm to MC data for that an artificial misalignment was introduced. A total of $5 \cdot 10^4$ tracks was generated and the detector walls T3 and T4 were offset by $-0.5\,\text{cm}$ in x-direction and $-0.2\,\text{cm}$ in z-direction. The MC hits were smeared with a Gaussian smear of width $\sigma = 350\,\mu\text{m}$. Due to the misalignment of the detector, the residual distribution of the initial fit (a) is significantly wider than the smearing, which effectively reduces the spatial resolution for real data. After applying the corrections calculated using the *pede* alignment, the residual distribution's width matches the smearing again (b).

simulation. For a more realistic setup, however, more iterations might be required. This is particularly important for forward boosted tracks. This is shown in chapter 8.3.6 and 8.3.7.

8.3.5 Rotational Alignment

In addition to translational alignment shown above, the correction of small rotations was tested. Here, all drift tube modules of station T3 were rotated around their local z'-axis[8] by $\gamma = 0.5°$. The corrections calculated for each module in station T3 are shown in figure 8.12. The results of the correction calculation are again close to the MC truth. In case

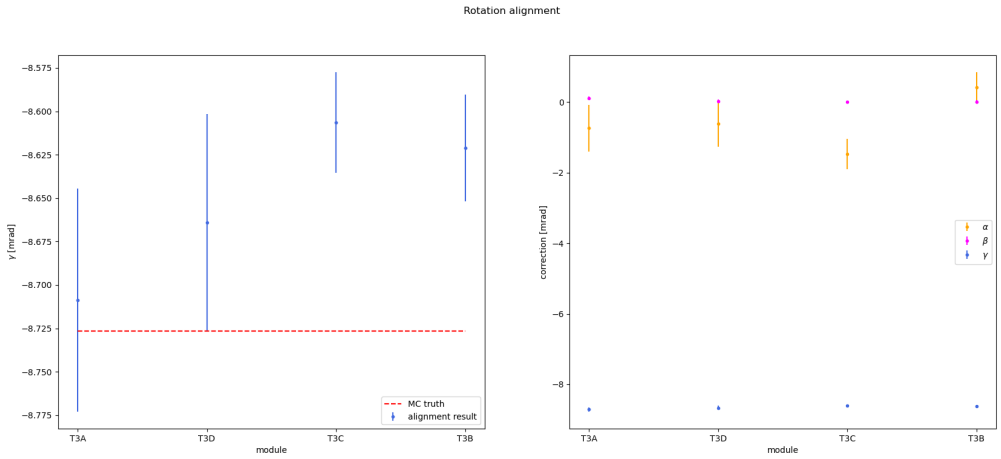

Figure 8.12: Correction for rotational misalignment of drift tube station T3, calculated using the *pede* software. A total of $5 \cdot 10^5$ MC tracks was fitted in a detector, where all drift tube modules of station T3 were artificially rotated around the z'-axis by 0.5°, corresponding to $\gamma \approx 8.7\,\text{mrad}$. The left plot shows the calculated corrections of γ alongside the MC truth, the right plot shows the corrections for γ in relation to the remaining two rotation angles. The MC truth is indicated by a dashed red line. As corrections, they have a sign opposite to the detector misalignment. Each module was rotated around its geometric center.

of correcting a rotational misalignment, an additional difficulty arises when compared to the correction of a pure translation. The further away a track passes a drift tube module from its geometric center (the alignment system's origin), the larger the effect of the misalignment. This introduces larger relative errors, compared to the translational alignment.

For testing, a setup was chosen where only the rotation angle γ was altered. Here, the effect of the systematic error is largest, since the achievable lever arm is largest with the half wire length of $\sim 80\,\text{cm}$ for stations T3 and T4.

[8] See e.g figure 7.2.

8.3.6 Realistic Detector Misalignment

A more realistic test of the alignment algorithm was performed with the 5×10^6 tracks that were simulated in a misaligned detector setup. In the real setup, the detector components were aligned using a survey measurement with a precision of 500 µm. For this test, a translation was applied to the $x-$ and z coordinates of each module of the stations T3 and T4, so that their combined effect shifts the end points of the drift tube's sense wire by the amount of 500 µm. In addition, a rotational misalignment around the z-axis was introduced such that the positions of the wire ends are shifted along the x-direction by additional 500 µm. Rotations around the other axes were not misaligned for this test as a precise measurement of the tracks' x-coordinates is considered most important.

The misalignment introduced to the MC generation is the translation $\vec{t}$ and the rotation γ:

$$\begin{aligned} \vec{t} &= \begin{pmatrix} 0.03536 \\ 0 \\ -0.03536 \end{pmatrix} \text{ cm}, \\ \gamma &= +0.625\,\text{mrad}. \end{aligned}$$

To correct this misalignment, an iterative alignment step was performed after the first, *initial* alignment step, which is described in the following section. To evaluate the effect of the alignment, the residual distribution was used. The distribution before the first alignment step, hence from the GBL fit in the misaligned detector geometry, is shown in figure 8.13. It shows a deviation from a normal distribution and a width, which is much larger than the Gaussian smearing width of the hits of 350 µm. Hence, for this misalignment setup, a substantial degradation in the spatial resolution can be observed.

After computing the alignment corrections using *pede* and applying the corrections for a second fit with the corrected geometry, the residual distribution shown in figure 8.14 was achieved. This now follows a normal distribution but does not yet represent the width of the hit smearing, showing ~ 20 µm degraded spatial resolution from the optimum value for the MC data. During the refit, however, new alignment data is calculated that can now be used for an iterative alignment process.

8.3.6.1 Iterative Alignment Steps

For the realistic detector misalignment, two iteration steps of the alignment were performed. After completing the GBL fit of the tracks in the misaligned detector, the resulting alignment data was optimized using *pede* in the *initial* alignment step. The corrections, calculated in this step were then applied to the detector coordinates and a complete refit of all tracks was performed using the corrected geometry, again resulting in a new set of alignment data. This new set of data was again optimized using *pede*. The

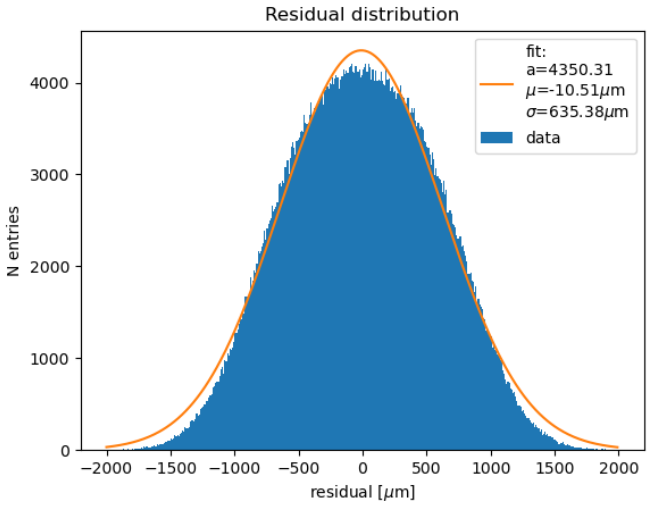

Figure 8.13: Residual distribution for misaligned stations T3 and T4 of the initial track fit, thus for the misaligned detector. The distribution is not Gaussian, however it is fitted with a Gaussian function to have a rough estimate of the distribution's width. Here, it is calculated to be $\sigma \approx 635\,\mu\text{m}$. The simulated hits were smeared using a Gaussian smearing with a width of $350\,\mu\text{m}$, hence this misalignment effectively reduces the spatial resolution of the drift tube spectrometer.

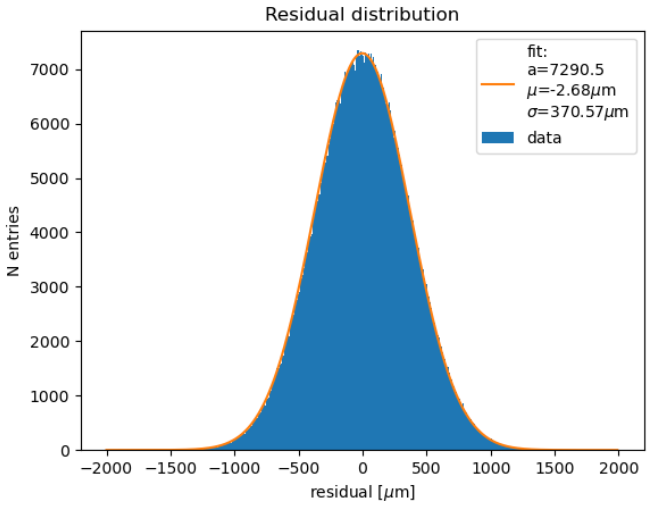

Figure 8.14: Residual distribution after correcting the misalignment with the alignment results from the first iteration. Other than the corrected detector coordinates this is the same data set as for figure 8.13. The distribution now has a Gaussian shape and a width of $\sim 370\,\mu\text{m}$. This is a significant improvement. However, since the hits are smeared in MC with a width of $350\,\mu\text{m}$, this width would be expected for the residual distribution if the detector is perfectly aligned. For a combined alignment of translation and rotation, more iterations after the initial alignment step are needed.

results were compared to the MC truth of the misalignment that was originally applied to the detector. The corrections that were calculated for all three misaligned degrees of freedom are shown in figures 8.15 for station T3 and 8.16 for station T4 respectively.

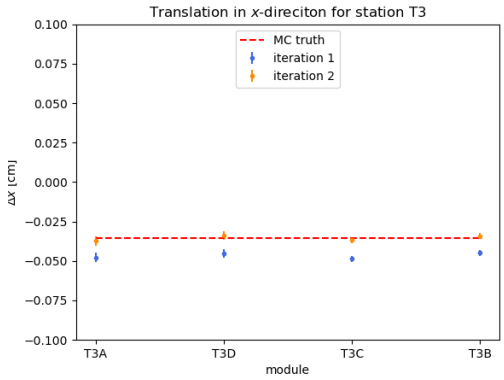

(a) translation along x

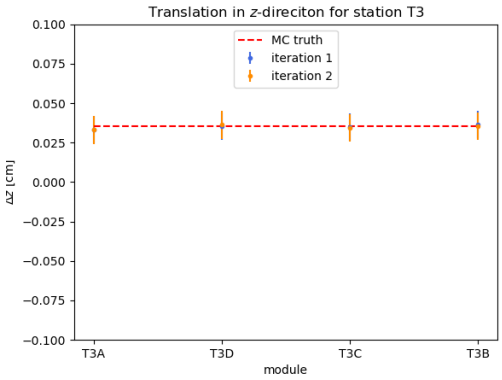

(b) translation along z

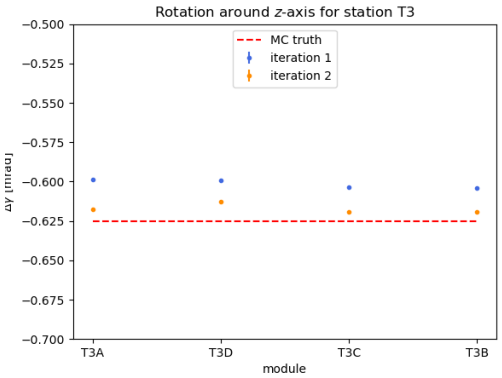

(c) rotation around z

Figure 8.15: Comparison of the alignment result to the MC truth for station T3. The alignment was also performed in an iteration step after applying the initial alignment and refitting using the corrected detector geometry from the initial alignment step. The corrections calculated in the initial alignment steps are drawn in blue, the corrections for the iteration in orange. In all cases, the correct value the should be corrected derived from the MC truth is shown as dashed, red line. The translational correction along the x-axis (a) approximates the MC truth within its 1σ error after one iteration step. For translations along the z-axis (b), no improvements were observed for an iteration step. The correction for the rotation angle γ around the z-axis (c) improve after iterating but after the first iteration the MC truth still is not within the 1σ error for this correction.

In figures 8.15 and 8.16 it can be seen that an alignment iteration shifts the corrected detector positions closer to the true misalignment, which was introduced in the simulation. Here, only one iteration on the initial alignment step was tested. However, any number of iterations can be performed until that point where the residual distribution does not

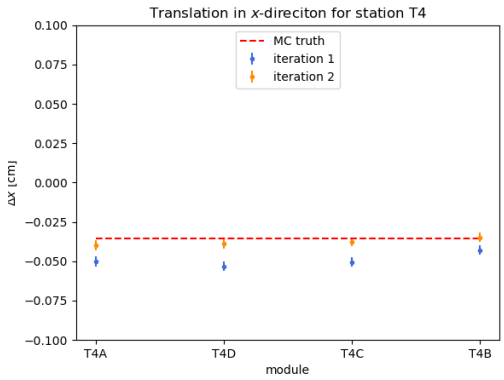

(a) translation along x

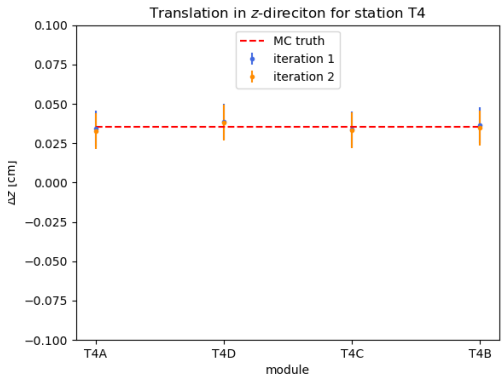

(b) translation along z

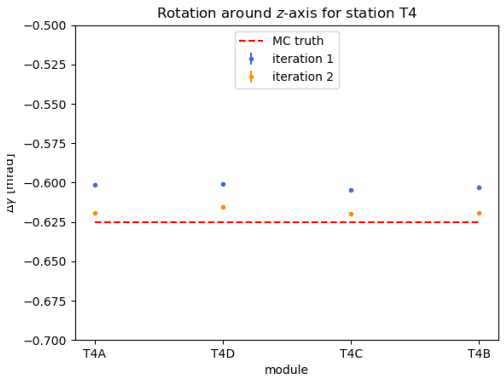

(c) rotation around z

Figure 8.16: Comparison of the alignment result to the MC truth for station T4. The alignment was also performed in an iteration step after applying the initial alignment and refitting using the corrected detector geometry from the initial alignment step. The corrections calculated in the initial alignment steps are drawn in blue, the corrections for the iteration in orange. In all cases, the correct value the should be corrected derived from the MC truth is shown as dashed, red line. The translational correction along the x-axis (a) approximates the MC truth within its 1σ error after one iteration step. For translations along the z-axis (b), no improvements were observed for an iteration step. The correction for the rotation angle γ around the z-axis (c) improve after iterating but after the first iteration the MC truth still is not within the 1σ error for this correction.

get any narrower after an alignment step.

8.3.7 Forward Boosted Tracks

As a last test, aligning for translations was tested again using MC tracks that were generated in a forward boosted distribution. In order to generate forward boosted tracks, two points were generated with the track being a straight line connecting these two points. The first, upstream point on the track was generated in a cylindrical volume of radius

$r = 5\,\text{cm}$ and length $l = 80\,\text{cm}$. The center of that *target-cylinder* is located on the beam axis, at a distance 3.6 m upstream of the drift tube station T1. The second point is generated at a plane directly upstream of station T1. In this plane at $z = 17\,\text{cm}$, a point is generated at a distance r from the beam axis, which is generated from a Gaussian distribution, centered around zero and a width of $\sigma = 3.0\,\text{cm}$. A point with this radius was finally placed in the xy-plane at a uniformly distributed, random angle in the range $[0, 2\pi)$. This does neither resemble the real coordinates of the target, nor does it account for the expected spectrum of the muons, hence their angular distribution.

The forward boosted tracks were again fitted using GBL in the translational misaligned detector geometry described above. The global derivatives were then aligned using *pede*. The results of the *pede* alignment are shown in figure 8.17. It can be seen that for forward

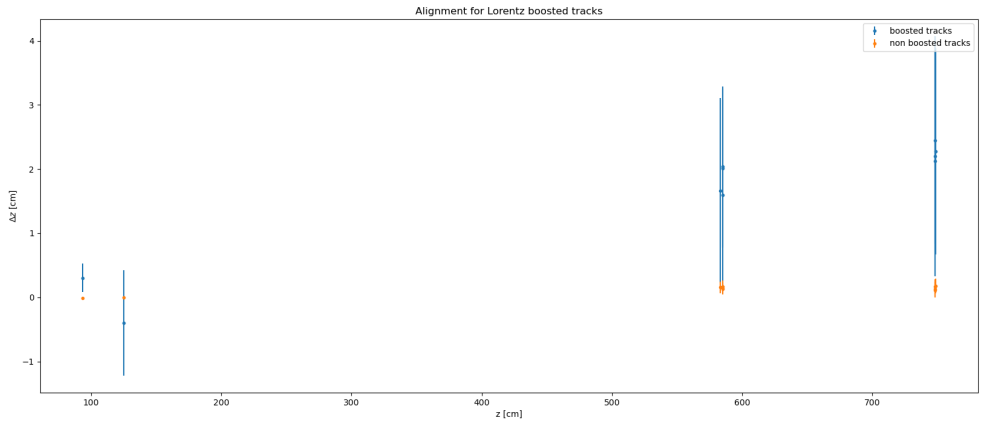

Figure 8.17: Corrections Δz calculated by *pede* plotted against their z-coordinate. For MC tracks simulated with a forward boost (blue), the calculated alignment has a dependence of the z coordinate itself, which is not the case for non-boosted tracks (orange). Both sets of tracks contained $5 \cdot 10^5$ tracks each and are simulated in the same, artificially misaligned detector geometry with only translational misalignment of stations T3 and T4 of $\Delta x = -0.5\,\text{cm}$ and $\Delta z = -0.2\,\text{cm}$.

boosted tracks, due to the much smaller angle of the tracks with respect to the beam axis, the translation corrections along the beam axis are far off the MC truth values and the errors grow with the distance from the target. When constraining the shift along the beam axis in the *pede* alignment process, arbitrary values for all the other alignment parameters are found, rendering an alignment using only forward boosted tracks impossible. It must be noted, however, that the performance of the GBL fit is not affected by the spectrum of tracks that is to be fitted. This only impacts the alignment process.

8.3.7.1 Track Sampling

By selecting a sample from the forward boosted tracks where the selection is done in such a way that the remaining slope distribution shows a wider spread, the alignment can be rendered possible for tracks with a forward boosted slope distribution. This *resampling* of the tracks was tested for the boosted MC tracks by defining a function which describes the probability p, to accept a track with a certain slope x') from the original sample to the reshaped sample. First, a histogram of the slope distribution is calculated for the original sample. For each slope bin, the probability $p(x')$ is calculated to accept a track with a slope, fitting into that particular bin. This probability is defined as

$$p(x') = \begin{cases} \frac{N_{\max}}{N_{\text{tracks}}(x')}, & \text{if } \frac{N_{\max}}{N_{\text{tracks}}(x')} < 1 \\ 1, & \text{otherwise} \end{cases} . \tag{8.6}$$

Here, $N_{\text{tracks}}(x')$ is the number of tracks in each specific bin of the original sample and $N_{\max}$ an arbitrary number, describing the mean content of the bins in the newly created sample, where tracks have been rejected. For this analysis, $N_{\max}$ was chosen to be 10 % of the bin content of the maximum bin in the unsampled distribution. The probability function to accept a track to the new sample, calculated using formula (8.6) is shown in figure 8.18. Then for each track in the unsampled set of tracks, the probability p to

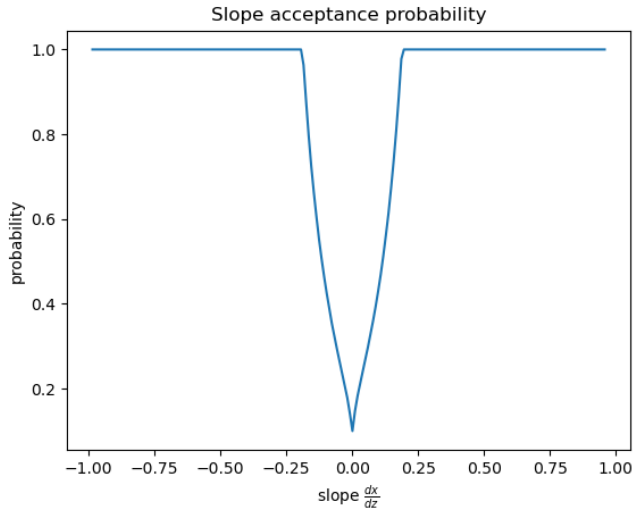

Figure 8.18: Probability function to accept a track with a certain slope to the resampled set of tracks. The probability p for each slope is calculated as. In the process of resampling, for each track the slope is calculated and the probability p to accept this track is looked up in the function shown above. Then a uniformly distributed random number $n \in [0, 1)$ is generated. If that random number fulfills $n < p$, the track is accepted to the new sample.

accept it is calculated using (8.6) and a random number $n \in [0, 1)$ is drawn. If this random number is smaller than p, the track is accepted to the new sample.

For an original set of $N = 10^7$ forward boosted tracks, the slope distribution of the resampled tracks is shown in figure 8.19.

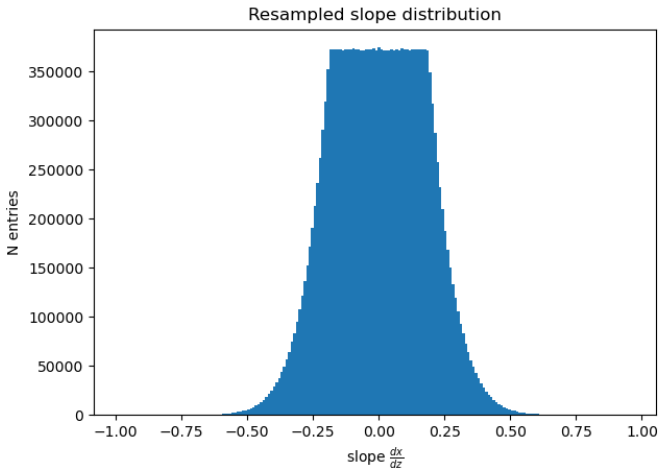

Figure 8.19: Slope distribution of forward boosted MC tracks after resampling.

Using these tracks, the GBL fit as well as the *pede* alignment is performed again. Therefore, the realistic misalignment setup was used again which was aligned with this sampled set of tracks. The results of the alignment can be seen in figures 8.20 for station T3 and 8.21 for station T4.

This shows that through selecting tracks from a set of forward boosted tracks, such that the remaining tracks have a more uniform slope distribution, the alignment is possible using forward boosted tracks at the cost of an increased statistical error.

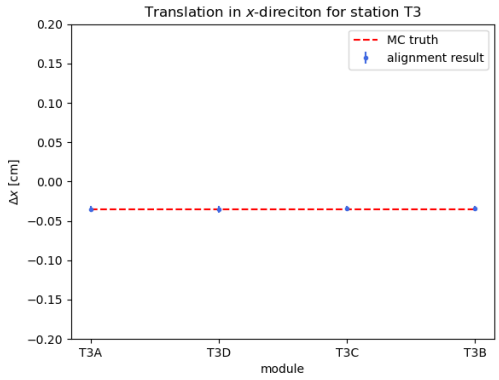

(a) translation along x

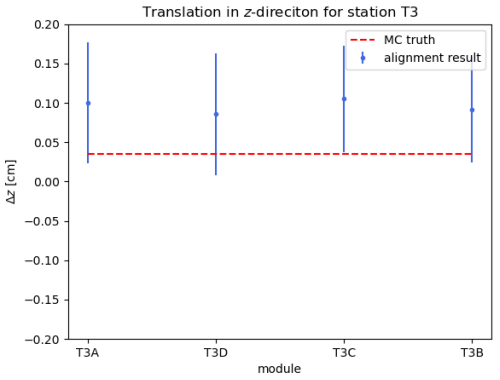

(b) translation along z

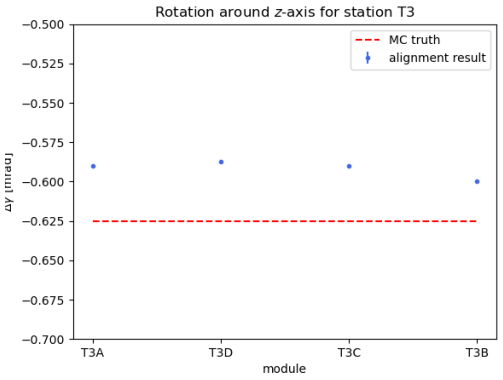

(c) rotation around z

Figure 8.20: Alignment corrections for station T3 computed with the resampled set of forward boosted tracks. Other than for the full set of tracks, with the reshaped distribution, all coordinates can be corrected. Just like for the uniformly distributed tracks for the non-boosted setup, the rotation angle γ needs to be corrected in an iterative process.

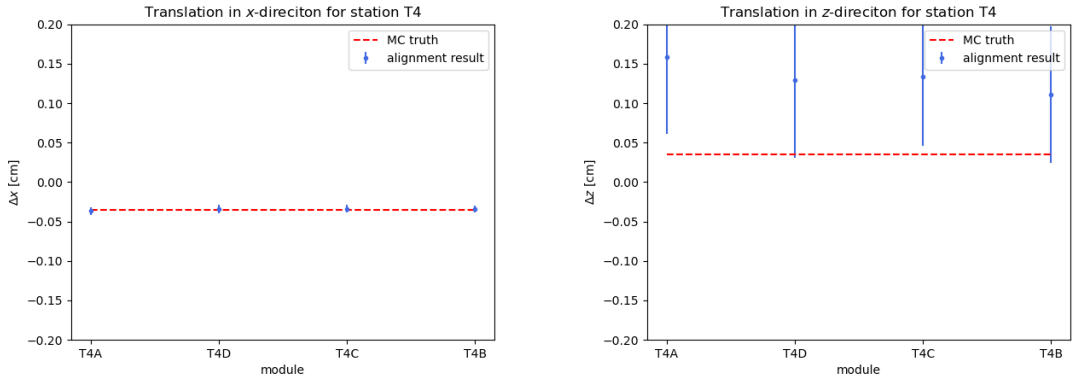

(a) translation along x

(b) translation along z

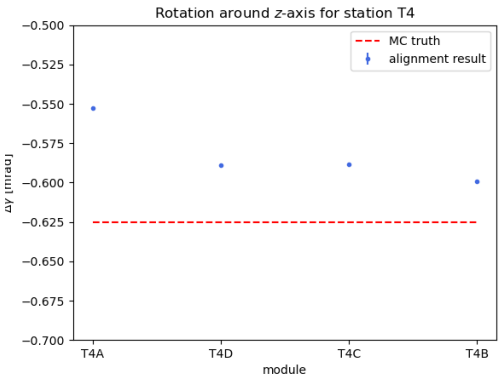

(c) rotation around z

Figure 8.21: Alignment corrections for station T4 computed with the resampled set of forward boosted tracks. Other than for the full set of tracks, with the reshaped distribution, all coordinates can be corrected. Just like for the uniformly distributed tracks for the non-boosted setup, the rotation angle γ needs to be corrected in an iterative process. For this most downstream station, the corrections in this initial alignment step for a translation along the z-direction, the MC truth, with the exception of one single module, lies outside of the 1σ error region, but close enough to be corrected in more iterations.

9 Refit and Alignment of Real Data

When the process of refitting real data from the experiment using GBL and aligning the detector using *pede* is compared to the MC (see chapter 8), several new challenges arise. The MC described before makes a number of simplifications which do not hold true anymore when applied for real data. Effects that are present for real data and not for MC are for example:

1. events with more than one track in the muon spectrometer
2. multiple scattering of muons in detector material
3. systematic errors such as incorrect rt-relations
4. non-uniform efficiency of drift tubes
5. non-uniform spatial resolution of drift tubes
6. noise that can lead to incorrect drift time measurements in a single tube or even result in drift time measurements for tubes that were not hit by a muon

By carefully selecting tracks that are used for the alignment process these errors cannot be countered but reduced. The criteria for track selection and the following refit and alignment with real data are described in the following.

9.1 Seed Tracks

The seed tracks used for a refit with the GBL fit are themselves fitted tracks. The seeds are first fitted using genfit and then passed for a GBL refit. Prior to the initial track fit using genfit, some necessary steps are performed. This includes the computation of a rt-relation and converting the measured drift times to radii of the corresponding drift circle. These radii are then used by the fitting algorithms[1] as measurement info. In this work, the drift distance $r(t)$ is provided by the seed tracks fitted from genfit. Hence, the same drift time to radius conversion is used as for the genfit tracks, which is described in [85]. Additionally, for the GBL fit no additional pattern recognition is performed[2]. Therefore, the same hits used for fitting the seed track are used for the GBL refit as well.

[1] Both genfit and GBL

[2] Such as *all* channels with hits for a particular event, drift time, time over threshold ...

9.1.1 Event Selection

First, for simplicity, events with more than one reconstructed track are rejected. As the angular deviation from the original track direction due to multiple scattering is smaller for higher energy muons, low energy muons should be rejected. As the alignment requires straight tracks, thus without a magnetic field on the muon tracks, a momentum reconstruction is not possible. Therefore, the tracks are required to be *muon tagged* by the RPC detector. This means that the RPC detector is required to have a track reconstructed both in x and y projections and this track, when extrapolated to the drift tube spectrometer, needs to match its fitted track. This implies a momentum cut below $\sim 3\,\mathrm{GeV}$[3][115], which reduces the error due to multiple scattering, which is larger for low energy muons. To counter noise, and track fits with too few degrees of freedom, events are selected with a few criteria on the number of hits. These are in particular the presence of at least two and a maximum of six hits per tracking station.

Another cut that can be made in order to reduce noise, is to introduce a lower limit on the *time over threshold*. The electric signal produces by a cluster of primary electrons and ions drifting within the tube's electric field and producing an avalanche typically has a width of several tens to several hundreds of nanoseconds. For real hits, charge is transported. Noise or crosstalk[4], on the other hand, does not transport charge, hence for electromagnetic noise, the time over threshold is expected to be short, since the charge transported is proportional to the time integral of the voltage signal and is expected to be (close to) zero. A cut has already been performed on the data set used within this thesis, where only hits are accepted with a time over threshold of more than $\sim 10\,\mathrm{ns}$[5]. A plot of the time over threshold as a function of the distance to the reconstructed track as well as versus the residuals of the remaining hits is shown in figure 9.1. This shows that the hits remaining after the pre-existing event-selection and noise cuts are sufficient. No particular threshold in the time over threshold can be seen at which the residuals are randomly distributed, hinting towards remaining noise. In order to save further computation time, the distribution shown in figure 9.1 is considered sufficient and no further rejection is done.

9.1.2 Resolution Function

Both the GBL fit as well as the alignment using *pede* weigh the fit at every hit with a precision $\delta = \frac{1}{\sigma^2}$. The resolution σ can be obtained from the residual distribution. When all residuals, regardless of where a track passes a tube, are used to compute the

[3] For 2.8 m of iron as muon filter around the RPC planes

[4] The L3 amplifier chips used here provide 4 amplifier channels on the same chip. If one channel is amplifying a *real* signal, it is possible that some of the other channels on the same chip can produce short voltage pulses. These are referred to as *crosstalk*.

[5] The waveform of a drift tube signal for a drift tube hit by a muon can contain several pulses individually surpassing the threshold. Here, the cut is applied if the *first* single pulse of the whole tube waveform is shorter than 10 ns.

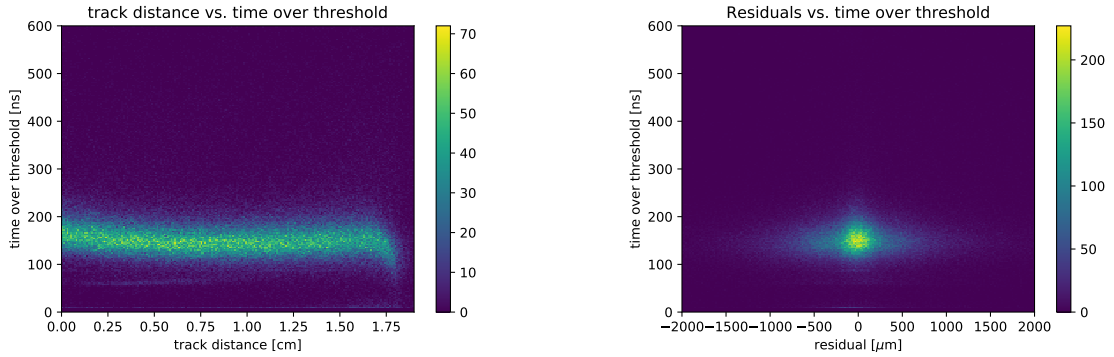

(a) Time over threshold vs. track distance from wire

(b) Time over threshold vs. residual

Figure 9.1: Time over threshold plotted versus the track distance (a) and the residuals (b). These plots were computed using all hits remaining after the event selection for one random proton spill of RUN 2200. The plot (a) shows a constant time over threshold distribution along the drift radii, which shows that the hits are dominated by real hits. Noise, for example due to the electronic amplifiers would result in the presence in very small times over threshold for all drift radii. This observation is supported in figure (b). Here, noise would result in a band at low time over thresholds with randomly distributed residuals, which cannot be seen. Even though noise is present in the raw measurement, the pre-existing noise cuts and event selection is therefore considered sufficient and no further cuts are introduced.

residual distribution, it represents an average resolution of the detector. To compute the *resolution function*, which describes the resolution of a drift tube as a function of the radius, at which a track passes the tube, a two dimensional histogram is calculated, which plots the residuals versus the track distance, at which it passes the tube. This plot is shown in figure 9.2. It shows a less densely populated band at track radii around $\sim 0.5\,\text{cm}$. This can be explained by systematic errors in the process of computing the rt-relation, which is examined in section 9.1.3. In the context of this thesis, the rt-relation provided by the pre-existing genfit track used as seed is used without further corrections.

To compute the resolution function, the histogram shown in figure 9.2 is divided into vertical slices by dividing the distance axes into 150 bins. For each of these bins, the corresponding *residual profile* is fitted with a Gaussian profile. An example of these fits is shown in figure 9.3. The width σ of the resulting fit is defined as resolution for that specific distance bin. Its error is the uncertainty of the fitted parameter σ. When the widths are plotted for all distance bins along with their errors, the resolution function shown in figure 9.4 is obtained. For the GBL fit, this is used as a lookup table, when not using MC, to compute the precision for each hit, which the GBL fit uses and also the alignment process using *pede* weighs the entries with.

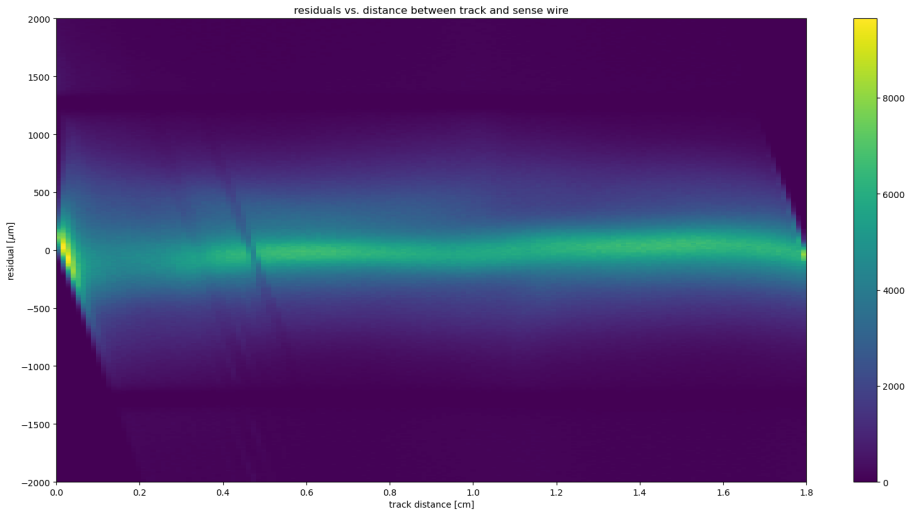

Figure 9.2: Histogram of the residuals for the seed track plotted versus the shortest distance between seed track and wire. It shows that most residuals follow a distribution around zero for tracks passing a tube at any radius around the sense wire. Very close to the sense wire ($r = 0\,\text{cm}$) and at near the tube's cathode wall ($r \approx 1.815\,\text{cm}$), deviations can be seen. The diagonal bounds at these distances originate in the computation of the residual σ as $\sigma = r(t) - d$, where $r(t)$ is the drift radius from the rt-relation and d is the distance between track and wire. Here, d is not directly constrained, while $r(t) \in [0, 1.815)$.

9.1.3 Drift Distance Distribution

Since the seed tracks are selected requiring them to be muon tagged, hence with hits in several layers of the RPC detector, they must, due to the detectors acceptance, be homogeneously distributed in the drift tubes. Thus, the distribution of measured drift distances would be expected to be a uniform one. However, the drift distance obtained from the seed tracks is distributed as shown in figure 9.5. It shows a distribution with peaks at $r = 0\,\text{cm}$ and $r = R_{\text{tube}} = 1.815\,\text{cm}$, as well two dips below $\sim 0.5\,\text{cm}$ and which is, in comparison with the expected uniform distribution, slightly skewed towards smaller drift distances. The peak at $r = 0\,\text{cm}$ can be explained with the time resolution for the drift time measurement, from which the drift distance is calculated. At small tube radii, the drift velocity is maximal, resulting in an overpopulation of the smallest drift time bins. The peak at the tubes' inner radius, on the other hand, can be explained with a drift tube's limited detection efficiency close to the cathode wall, which is described in section 9.1.4. When the lower efficiency close to R_{tube} is not considered, when correcting the rt-relation using an initial track fit[6], tracks that pass close to the cathode wall and that are, despite the lower probability, detected by the tube, overpopulate the maximum radius bin. The tubes' efficiency as a function of the radius can also explain the skewing

[6]See section 4.3 for details.

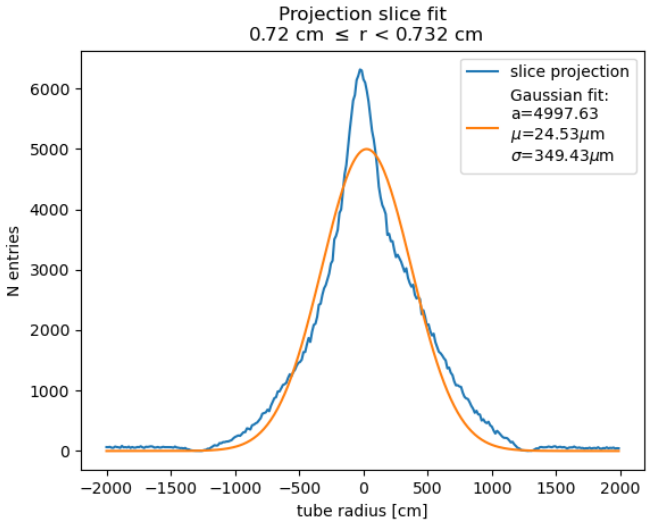

Figure 9.3: Residual projection for a slice along the distance between seed track and sense wire. Here, a slice at 40 % of the tube's radius of 1.1815 cm is shown as an example. The residual projection at a specific tube radius is fitted with a Gaussian distribution. The width σ of the fitted function is used the resolution at that radius, the error is the error of the fitted parameter σ. Even though the Gaussian fit, does not fit the distribution of the projected residuals, its parameters are used as an estimate of the resolution.

towards smaller drift distances. The two dips, however, hint towards systematic errors in either initial track fit using genfit, the calculation of the rt-relation or their correction using the initial genfit tracks. A reworked computation and correction of the rt-relations, whose application is expected to result in a more uniform distribution of drift distance measurements is being worked on, but is not part of this thesis.

9.1.4 Detection Efficiency

The drift tubes' detection efficiency depends on the radius of the tube, at which a track passes it. Close to the cathode wall, the electric field is smallest, hence electrons and ion pairs are more likely to recombine, which renders them impossible to detect. In addition, the tracks pass a shorter distance in the tube close to the cathode, decreasing the chance to ionize the drift gas, assuming a homogeneous ionization density. To compute the efficiency $\eta = \eta(r)$ as a function of the tube radius r at which the tube is hit, the seed tracks from genfit are used. For this reconstructed track, the closest approach between the track and all sense wires of the whole drift tube spectrometer are calculated. If this closest approach d is smaller than 1.85 cm[7], it is checked if for that particular tube, an electronic hit was recorded.

By dividing the tubes' radius into 500 bins, for each bin both the number N_0 of reconstructed tracks passing inside the tube's inner radius and the number of recorded hits N_h

[7]Tube radius of 1.815 cm plus a small margin to account for incorrectly reconstructed tracks

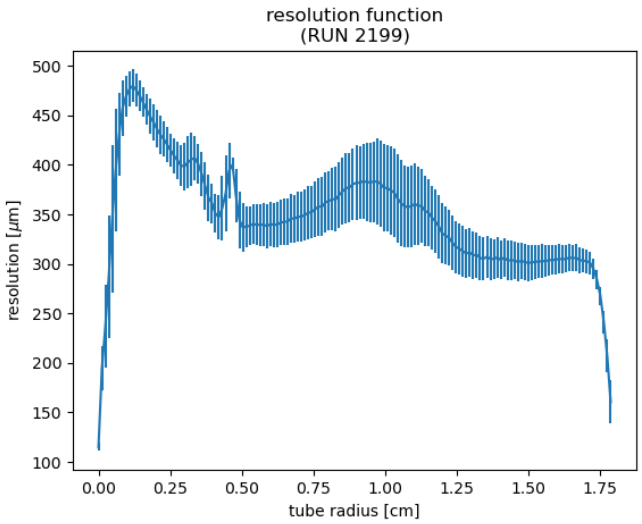

Figure 9.4: Resolution as a function of the radius, at which a track passed the drift tube. This function is summed for all tubes and all tracks of RUN 2199. The resolution was calculated by fitting the residuals for a total of 150 slices along the track distances in figure 9.2 with Gaussian distributions. An example of these slices is shown in figure 9.3. Note that at $r = 0$, the resolution is close to zero, meaning a vanishing uncertainty on radius measurements. This is a numeric artifact, it is expected that the rise of the resolution function towards smaller tube radii continues up to the sense wire at $r = 0$. For small radii, the rise can be explained with the electric field, which is strongest at small radii. Here, the drifting electrons' velocity is maximal and the error on the drift time measurement is dominated by time resolution of the TDCs, recording the drift time.

can be counted. Then, for each bin, the efficiency η can be defined as

$$\eta = \frac{N_h}{N_0}. \tag{9.1}$$

The corresponding error σ_η, assuming a Poissonian distributed number of hits per bin, is defined as

$$\sigma_\eta = \sqrt{\frac{\eta(1-\eta)}{N_0}}. \tag{9.2}$$

For a random selection of 40 proton spills recorded in RUN 2199, the reconstructed genfit tracks were used to compute the detection efficiency. The hits at certain radii were summed for all tubes for this analysis. A plot showing the detection efficiency as a function of the radius, at which a tube is hit, is shown in figure 9.6. The efficiency is roughly constant for a large fraction of the tube's radius with a level of $\sim 95\%$. The closes to the cathode a tube is hit, the higher the probability for a recombination and the lower the probability for an ionization is, hence the detection efficiency drops. This can be seen for radii $> 1.7\,\text{cm}$. A detailed view of the region close to the cathode wall in figure 9.6 is

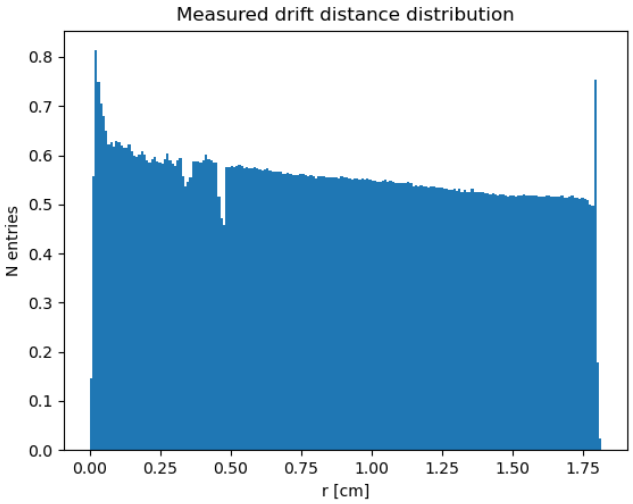

Figure 9.5: Distribution of measured drift distances. The drift distances are converted from measured drift times using the rt-relation. For the muon tagged tracks, a homogeneous distribution flux of muons through the drift tubes can assumed. This would result in a uniform distribution of drift distances. The measured distribution, shows two dips below $\sim 0.5\,\text{cm}$, as well as peaks at $r = 0\,\text{cm}$ and $r = 1.815\,\text{cm}$, the inner radius of the drift tube. The peak at zero can be explained with the time resolution of the drift time measurement, limiting the spatial resolution close to the sense wire. The peak at $r \approx 1.815\,\text{cm}$ is due to a non-uniform detection efficiency of the tube, which is lower close to the cathode wall but not accounted for when creating the rt-relation. This also explains the general falling slope of the distribution since, by neglecting the efficiency as function of the radius for the drift tubes, rt-conversions are biased towards smaller radii. The two dips hint towards systematic errors in either the pattern recognition, or the computation of the rt-relation. The distribution is normalized to $\frac{1}{binwidth} \approx 169$.

shown in figure 9.7. The efficiency σ_c close to the sense wire[8] is

$$\sigma_\text{c} = (97.4 \pm 0.2)\,\%,$$

while at the cathode walls' inner radius[9] $R_t = 1.815\,\text{cm}$, the efficiency σ_o is:

$$\sigma_\text{o} = (54.1 \pm 0.6)\,\%.$$

9.2 GBL Fit Performance

The refit of the existing tracks using GBL is the first step of an alignment process. To ensure, it is working as demonstrated for the simulated tracks in chapter 8, it needs to

[8] Computed at bin number 10, corresponding to $370\,\mu\text{m} \leq r < 407\,\mu\text{m}$.
[9] Bin number 490

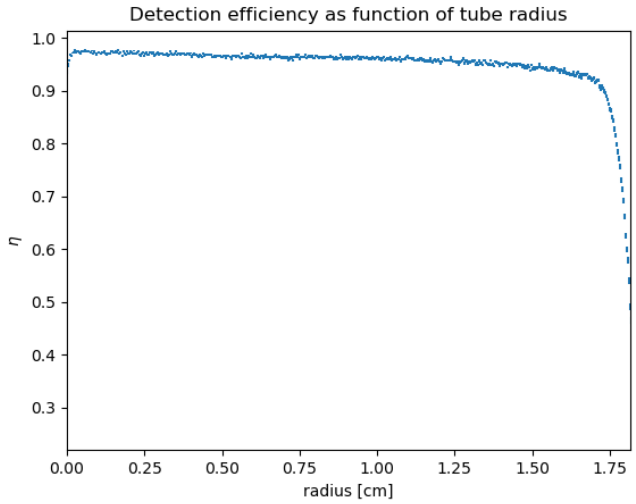

Figure 9.6: Detection efficiency η as a function of the radius at which a track passes a tube. For a large fraction of the tube, the detection is roughly constant at $\sim$ 95 percent. For radii $>$ 1.7 cm the efficiency begins to drop. This can be explained with the electric field inside the tube, introduced in equation (4.10), which is minimal at the tube's cathode wall, where electron and ion pairs might recombine before being separated by drifting along electric field and finally detected. The efficiency and its error are calculated using equations (9.1) and (9.2).

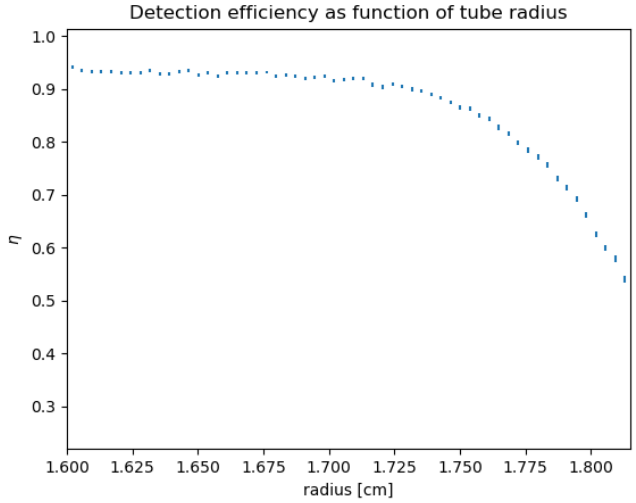

Figure 9.7: Detection efficiency η as a function of the radius at which a track passes a tube. This shows a zoom to the region close to the cathode wall of the plot shown in figure 9.6.

be checked if the GBL tracks show a result which is consistent with the pre existing seed track.

9.2.1 Deviation from Seed Track

As a consistency check, the slopes of the tracks are again compared with the slopes of the seed tracks, the same way as it was performed for MC tracks in section 8.2.1. The slope deviations $\Delta x'$ and $\Delta y'$ between seed and GBL fitted track are calculated using equations (9.3) and (9.4).

$$\Delta x' = \left(\frac{dx}{dz}\right)_{\text{GBL}} - \left(\frac{dx}{dz}\right)_{\text{seed}} \tag{9.3}$$

$$\Delta y' = \left(\frac{dy}{dz}\right)_{\text{GBL}} - \left(\frac{dy}{dz}\right)_{\text{seed}} \tag{9.4}$$

The deviation of slopes both in the x- and y-directions is shown in figure 9.8. Both

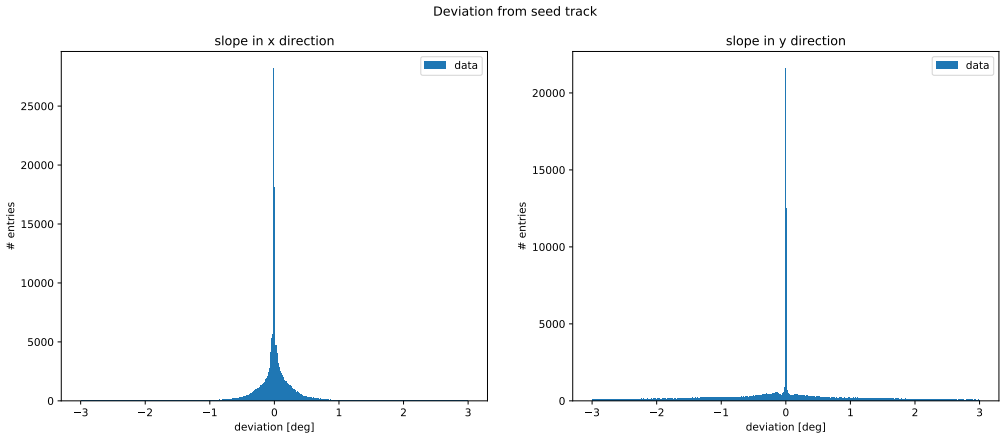

Figure 9.8: Deviation between slope of refitted GBL tracks and slope of seed tracks fitted by genfit. These distributions were calculated for a set of 40 spills of RUN 2199 with the above mentioned track selection criteria applied. The sharp peaks at zero for both distributions represent tracks where the GBL fit exactly reproduces the seed track. This would be expected for all tracks. However, for the GBL fit, hits were rejected with a distance between hit sense wire and seed track of more than 2 cm, which can explain the differences. Only the drift tube modules with a stereo angle contribute the y-direction measurement. Since here, less hits are present in total, the rejection of one of those hits has a larger effect then for the x-direction, hence this distribution is wider. The shown distributions are calculated using equations (9.3) and (9.4) converted to degrees.

distributions are dominated by sharp peaks around zero. These sharp peaks represent tracks, where the GBL fit exactly reproduced the seed track from genfit. When compared to the MC, where a certain width of the distribution would be expected due to the hit smearing, here a sharp peak is expected at zero, since the seed track is already a fitted one, hence the residuals are already minimal. However, there are differences between seed track and GBL track, which is due to the rejection of hits with distance between seed track and wire of more than 2 cm, which was added for the GBL fit. The rejection of a

hit in one of the drift tube modules with a stereo angle leads to larger deviations in the y-direction than it does for the x-direction since there are fewer hits in total contributing to the y-measurement than to the x-measurement.

The presence of hits, where the seed track is more than 2 cm away from the sense wire hints towards flaws in the pre-existing pattern recognition used before fitting. Work towards a new pattern recognition has already begun and might improve the results in the future. However, it is not part of this thesis.

9.3 Alignment

After testing the performance of the GBL fit applied to real data, the global derivatives extracted during the fit are used for a track-based alignment of the detector. This first requires an analysis of the angular distribution of the tracks.

9.3.1 Resampling

The angular distribution of the tracks reconstructed from real data is first analyzed. When compared to the forward boosted track generation of simulated tracks, the width of the slope distribution is roughly an order of magnitude smaller.

This shows a challenging situation for the track based alignment with sufficient tracks. The number of tracks directly impacts the precision of the alignment process. When sampling the tracks with the method described in section 8.3.7.1 with the parameter $N_{\max}$ for equation (8.6) set to 5% of the number of entries in the bin containing the maximum of the slope distribution, the resulting, normalized spectrum is shown in figure 9.9. An alignment using the sampled distribution shows unrealistic large corrections in the order of several centimeters, just as demonstrated for the forward boosted MC track set (without sampling). Sampling with smaller values of $N_{\max}$ results in too few tracks remaining to perform an alignment. Even though all drift tube modules contain hits, the slope distribution is so narrow that, in order to reshape it sufficiently, the number of tracks rejected is too large to perform an alignment with the remaining tracks.

Dropping the requirements for tracks to be muon tagged and to have hits in the most downstream station T4 can increase the width of the accepted tracks' slope distribution. However, a test using data from RUN 2201 showed no widening of the according distribution through dropping these requirements.

9.3.2 Constraints

Since sampling the tracks does not enable an alignment using the events selected for alignment tests, another effort can be undertaken by using an unsampled set of tracks and introducing constraints to the alignment process. To understand the effects of constraints,

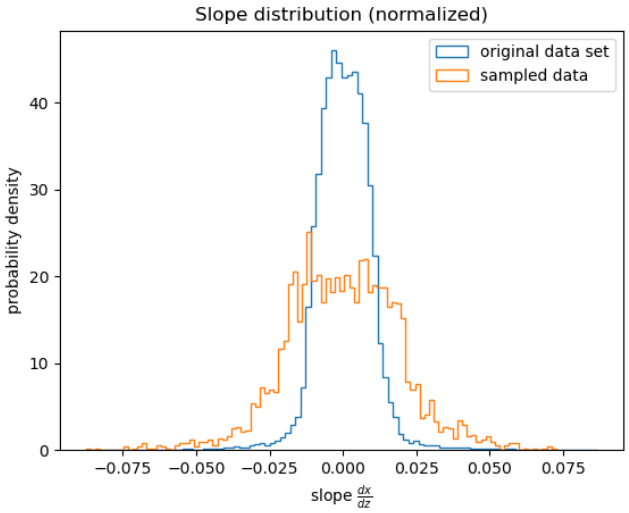

Figure 9.9: Normalized spectrum after sampling (orange) in comparison to the spectrum before sampling (blue). This distribution was calculated for RUN 2200, which is in comparable to the other RUNs with the spectrometer magnet switched off. Note that the range in which slopes are plotted represent the whole spectrum found in the tracks reconstructed with the above mentioned event selection. The resulting, sampled distribution is an order of magnitude narrower than the distribution used in the MC simulation.

first the alignment process is performed with the full set of data for RUN 2199 without any additional constraints. The results of the alignment process are shown in figures 9.10 for station T2, 9.11 for station T3 and 9.12 for T4.

The alignment results are not within a range which is compatible with the optical survey alignment's resolution of 500 µm. The alignment parameters for all drift tube modules of station T3, and likewise for T4, should be compatible with each other because all the drift tube modules of each of the downstream stations are mounted on the same, stiff frame. In addition, the corrections calculated for station T3 and T4 would be expected to be roughly the same, since the mounting frames of these stations are attached to each other via stiff aluminum profiles. These criteria are not fulfilled by the calculated alignment parameters, hence they are considered not reasonable. If these alignment parameters, however are applied and a refit is performed with the altered detector geometry, the residual distribution becomes wider and more deviated from a Gaussian distribution. Also, the efficiency of the fit is reduced and more tracks can not be fitted since too many hits are rejected because the distance between seed track and sense wire is too large.

Tested constraints affected the movement of detector parts along the z-direction. Two setups were tested. First the fixation of all downstream drift tube modules to their nominal z-coordinate and second the requirement that the average movement of all downstream modules along the z-direction is negligible. Neither of these methods could improve the spectrometers alignment as well. The introduction of any kinds of constraints concern-

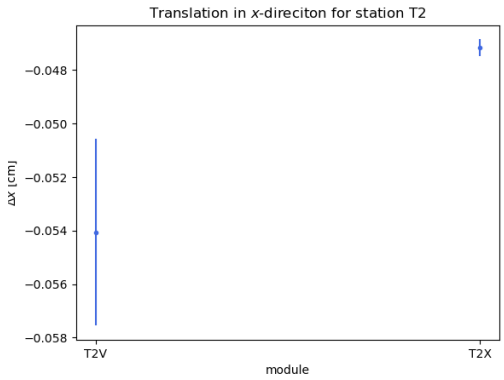

(a) translation in x-direction

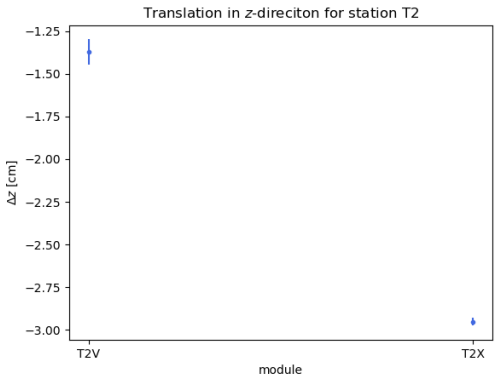

(b) translation in z-direction

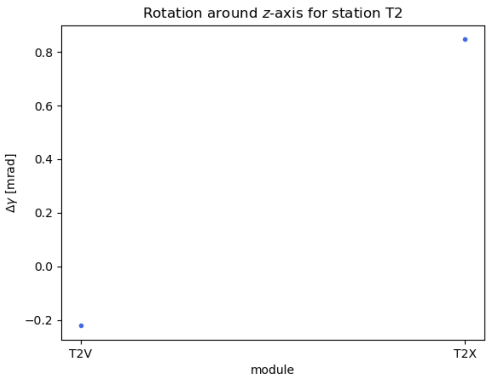

(c) rotation angle γ

Figure 9.10: Alignment corrections calculated for station T2 using the the full RUN 2199 data sample. The same set of parameters was chosen for alignment as for the alignment using MC tracks. Since the initial alignment using the optical survey measurement is used for the underlying fit, the alignment corrections in the z-direction are beyond a reasonable scale, as the survey measurement was performed with an accuracy of $\sim 500\,\mu\text{m}$.

ing movement along the z-axis led to random appearing alignment parameters in the remaining directions and rotations in the order of several centimeters or tens of degrees of rotation respectively.Provided the available data set, the alignment cannot be improved, using the methods described in this thesis, by introducing constraints as well.

9.3.3 Iterations

In iterative steps, the presumably wrong alignment results applied from the previous iteration could not have been corrected again. Due to the application of wrong corrections, the next iteration's fit using GBL fails in many cases. Then, too many hits are rejected in the fitting process because the *aligned* sense wires are too far away from the seed track. Using the available data, no statement can be given about the possible improvements of the alignment through iterative steps. However, it is likely to provide improvements if a

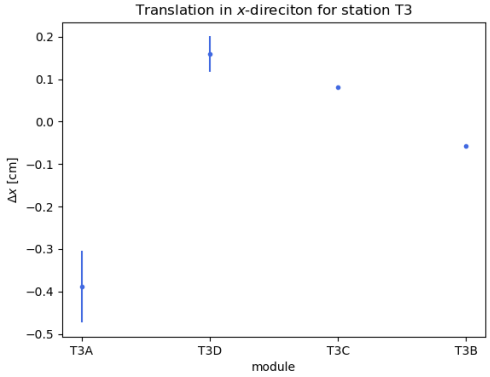

(a) translation in x-direction

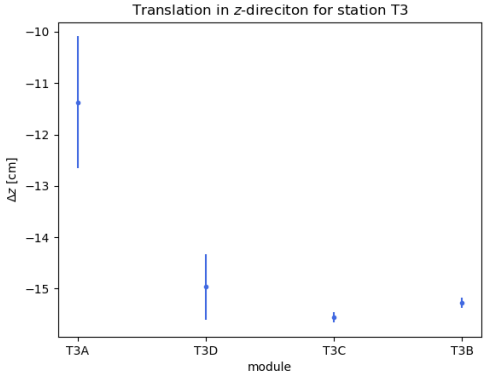

(b) translation in z-direction

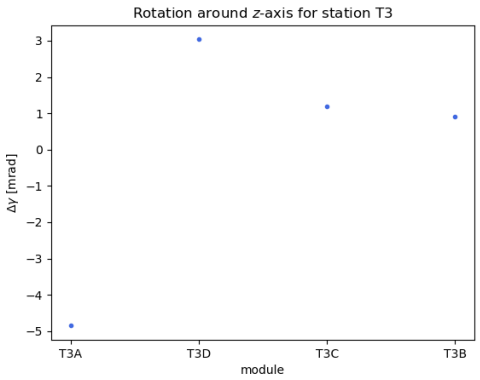

(c) rotation angle γ

Figure 9.11: Alignment corrections calculated for station T3 using the the full RUN 2199 data sample. The same set of parameters was chosen for alignment as for the alignment using MC tracks. Since the initial alignment using the optical survey measurement is used for the underlying fit, the alignment corrections are beyond a reasonable scale, as the survey measurement was performed with an accuracy of $\sim 500\,\mu\text{m}$. Additionally, since all modules of station T3 are mounted on the same frame, corrections for the individual modules are expected to match with each other. Here, the module T3A has calculated corrections incompatible with the other ones. This is the module with the fewest hits.

track sample is available which enables a rough alignment in the initial alignment step.

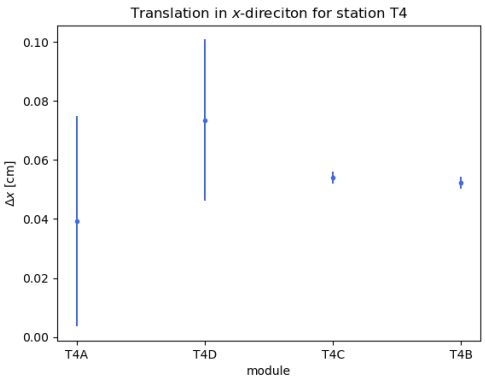

(a) translation in x-direction

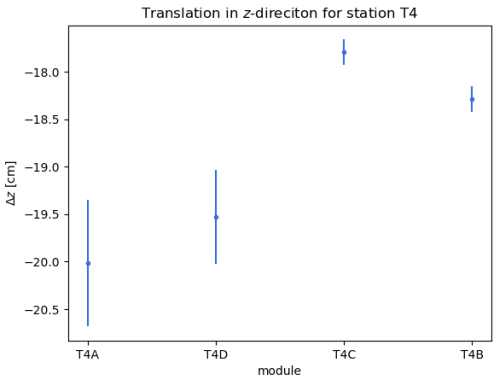

(b) translation in z-direction

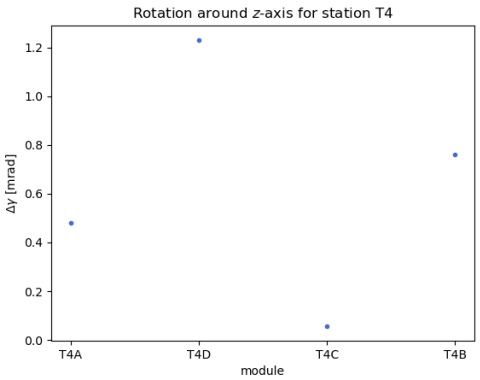

(c) rotation angle γ

Figure 9.12: Alignment corrections calculated for station T4 using the the full RUN 2199 data sample. The same set of parameters was chosen for alignment as for the alignment using MC tracks. Since the initial alignment using the optical survey measurement is used for the underlying fit, the alignment corrections are beyond a reasonable scale, as the survey measurement was performed with an accuracy of $\sim 500\,\mu\text{m}$. Like for station T3, the modules of station T4 are also mounted on the same frame. In this case, the corrections for all modules of this stations agree with each other. However, since the stations T3 and T4 are connected to each other with stiff aluminum profiles, the alignment corrections in the z direction are also expected to agree, which again, they do not.

Part IV

Conclusion

10 Conclusion

In the context of this thesis, a drift tube spectrometer, consisting of 12 modules of 48 drift tubes each, was assembled, commissioned, operated in experiment conditions, as well as decommissioned. The muon tracks measured with this spectrometer were used to analyze the tracking capabilities of the spectrometer and to implement a new tracking algorithm into the SHiP software framework. This algorithm is able to reconstruct straight tracks and thereby extract data that can be used for an offline, track based alignment.

The process of fitting and aligning has been tested using simulated, straight tracks. Using the simulated tracks, the performance of the track based alignment process was demonstrated. Misalignment, introduced artificially to the simulation can be corrected. Using simulated tracks, the performance of the alignment process was examined for different angular distributions of the tracks. For fixed target experiments, forward boosted angular distributions are typical, for which the alignment offers difficulties. A track selection method was presented to overcome this and was able to perform a track-based alignment using forward boosted tracks as well.

When applied to real data, the newly implemented track fit was compared to the pre-existing fit and it was demonstrated that it finds the same track, with the additional benefit of providing data usable for alignment. The alignment of the detector using the data generated during the fit, however, did not improve the spatial resolution of the spectrometer, as the required sampling of the forward boosted set of tracks leaves too few tracks remaining the usable sample.

Overall, using empirical corrections [85] to the optical survey alignment of the spectrometer, as well as calibration of the rt-relation, a spatial resolution of 373 µm was achieved. When compared to the software-aligned resolution of 270 µm, which was achieved with drift tube modules of the same type at the OPERA experiment, this seems to be a reasonable result.

The same muon tracks measured with this drift tube spectrometer have been used by the collaboration to determine the spectrum of muons emerging from a replica of the SHiP proton target. This measurement provided an important validation and improvement of the physics simulation, which is used to determine the background for the SHiP experiment. Since SHiP depends on precise background knowledge, this was an important milestone for the project.

11 Outlook

During chapter 8 it was shown that an alignment of the detector geometry is possible with Monte Carlo tracks, even when the tracks used for alignment are forward-boosted. However, considering the sampling of tracks required before alignment, the amount of data taken is not sufficient. A new pattern recognition that is currently being developed can potentially increase the amount of usable tracks for the alignment using magnet-off data. In addition to the pattern recognition, a new calibration method for the rt-relations is being worked on. This has the potential to increase the drift tube spectrometer's spatial resolution on its own, but can also be beneficial for a track-based alignment, which will provide more precise seed track measurements. By loosening the requirements on the number of hits or tracks being muon tagged, events with two or more muons in the final state can be beneficial, as they can have larger slopes. This requires a pattern recognition, which can reliably separate two tracks, even if they produce hits close to each other in any tracking station. Utilizing all these options, the same spatial resolution for the drift tube spectrometer as in the OPERA experiment of $\sim 270\,\mu\text{m}$ is probably reachable. With an improved spatial resolution, the momentum resolution for the muon spectrum is increased as well.

On the other hand, the alignment process using the GBL fit and pede alignment can handle curved tracks as well. For these tracks, not only the amount of available data is larger but they also hit the downstream drift tubes in a wide angular distribution. A future extension of the algorithm for fitting and aligning to using curved muon tracks potentially enables the alignment of the drift tube spectrometer for the muon flux measurement.

The SHiP experiment's Spectrometer Straw Tracker (SST) can also benefit from track based alignment. Especially, when the GBL fit is implemented for curved tracks, an alignment of the straw tracker is possible without the need for additional runs without a magnetic field. Potentially, external tracking detectors might be used as well, which enables atmospheric muons to be used for an alignment of the straw tracker and largely increases the angular acceptance.

Some of the drift tube modules used within this thesis are currently being used to provide reference tracks to examine the tracking ability of a prototype for the SHiP SST. In the near future, efforts are being planned, to enable this drift tube tracker to reconstruct three dimensional tracks using atmospheric muons. Here, the implemented three dimensional track fit as well as the alignment can provide precisely measured reference tracks for the SST prototypes, that are currently being developed.

Acknowledgments

When these lines are written, the world faces a very challenging time. Completing a thesis in such a time is particularly challenging and it is absolutely necessary to thank some people for help in the last few years, not only in the time we face a global health crisis. First and foremost I want to thank Prof. Dr. Caren Hagner for accepting me as a doctoral student in her fantastic working group. She enabled me to visit some of the most exciting places a physicist can dream of, meet scientists from all around the world and to work in an international collaboration. This did not only render the work presented in this thesis possible but also changed me as an individual.

Of course, Dr. Daniel Bick deserves just as much acknowledgment. We worked very closely together, faced and resolved a few very interesting tasks and last, but not least were able to have a good time after hard days of work.
I need to thank both of you for the tremendous amount of confidence you placed in me.

Furthermore I want to thank all the people who are part of the *muflux- and charm* teams at CERN and all the other institutions who participated in the measurements. I need to particularly mention Dr. Eric van Herwijnen for always asking me the right questions that pushed me towards solving some of my most intriguing puzzles. Also Dr. Thomas Ruf helped a lot in understanding the SHiP software framework, which was of course a requirement for extending it.

Thank you, Dr. Daniel Bick, Dr. Björn Opitz, *Hajo* Ohmacht and Benedict Kaiser for the exhausting but very fun weeks at CERN when assembling the detector and shifting at operation. I also want to thank Prof. Dr. Walter Schmidt-Parzefall for always being available for questions and always having hints that typically lead in the right direction.

The experiment itself is only part of this thesis. When working with the data, I also had a huge amount of help for applying the GBL fit to our setup by Dr. Claus Kleinwort and understanding the alignment procedure. Dr. Björn Wonsak kindly shared his experiences on this topic as well he made with a similar detector type. It helped a lot.

Of course, a thesis such as this one also needs to be edited before publication. I want to thank everyone, who carefully read drafts of this thesis. Dr. Björn Opitz, Dr. Henning Rebber, David Meyhöfer, Morten Henken and Hauke Schmidt in particular.

I need to thank everyone else, actively or formerly working in the research group in Hamburg. You all provide an atmosphere that is fantastic to work in.

Contradictory to common assumptions, doctoral students have a bit of spare time. In this spare time, I had a lot of support as well. First of course, my wife Julia deserves my

most profound thanks. I guess you had just as hard times with me as I did myself. Thank you for always being with me! Of course, my parents supported me all throughout my studies and I cannot thank you enough for enabling me to start an academic career. In particular I tank my mother Doris with Ernst-Wilhelm, my father Michael and Patricia. I thank my sister Kathi and her husband Ricardo. We also had a great time. A tremendous amount of support also came from my parents-in-law Margot and Ralph, as well as Marion and Arnfrid. Thank you, Kerstin, Karsten, Julia and Mert, Sybille and Reinhard. Thank you all.

Good friends can divert your attention and thereby provide tremendous relief. Here I need to thank Sarah for everything. Thank you Kimmi and Erk. You placed a VERY special confidence in me and I will be available for you, Annetin, whenever you need me. The same of course holds true for you, Norwin. Thank you Padda, Anna, Tini, David, Marc, Michi, Tobi, Chris, Jana, Nils, Katta, Mirco, Janina and Sascha.

It is probably impossible to mention everyone here who deserves to be mentioned. Please be sure that I am grateful.

Thank you.

Bibliography

[1] G. Aad et al. Observation of a new particle in the search for the standard model higgs boson with the atlas detector at the lhc. *Physics Letters B*, 716(1):129, 2012. ISSN 0370-2693. doi:10.1016/j.physletb.2012.08.020. URL http://www.sciencedirect.com/science/article/pii/S037026931200857X.

[2] S. Chatrchyan et al. Observation of a new boson at a mass of 125 gev with the cms experiment at the lhc. *Physics Letters B*, 716(1):3061, 2012. ISSN 0370-2693. doi:10.1016/j.physletb.2012.08.021. URL http://www.sciencedirect.com/science/article/pii/S0370269312008581.

[3] J. J. Thomson M.A. F.R.S. Xl. cathode rays. *The London, Edinburgh, and Dublin Philosophical Magazine and Journal of Science*, 44(269): 293316, 1897. doi:10.1080/14786449708621070. URL https://doi.org/10.1080/14786449708621070.

[4] E. Rutherford. The scattering of alpha and beta particles by matter and the structure of the atom. *Phil. Mag. Ser. 6*, 21:669688, 1911. doi:10.1080/14786440508637080.

[5] Professor Sir E. Rutherford F.R.S. Liv. collision of particles with light atoms. iv. an anomalous effect in nitrogen. *The London, Edinburgh, and Dublin Philosophical Magazine and Journal of Science*, 37(222):581587, 1919. doi:10.1080/14786440608635919. URL https://doi.org/10.1080/14786440608635919.

[6] J. Chadwick. Possible existence of a neutron. *Nature*, 129(3252):312312, 1932. ISSN 1476-4687. doi:10.1038/129312a0. URL https://doi.org/10.1038/129312a0.

[7] Wolfgang Pauli. Liebe radioaktive damen und herren - offener brief an die gruppe der radioaktiven bei der gauvereins-tagung zu tübingen. *https://cds.cern.ch/record/83282/files/meitner_0393.pdf*, Dezember 1930.

[8] C. L. Cowan, F. Reines, F. B. Harrison, H. W. Kruse, and A. D. McGuire. Detection of the free neutrino: a confirmation. *Science*, 124(3212):103104, 1956. ISSN 0036-8075. doi:10.1126/science.124.3212.103. URL https://science.sciencemag.org/content/124/3212/103.

[9] Andrei D Sakharov. Violation of CP in variance, c asymmetry, and baryon asymmetry of the universe. *Soviet Physics Uspekhi*, 34(5):392393, may 1991. doi:10.1070/pu1991v034n05abeh002497. URL `https://doi.org/10.1070%2Fpu1991v034n05abeh002497`.

[10] Hermann Weyl. Elektron und gravitation. i. *Zeitschrift für Physik*, 56(5):330352, 1929. ISSN 0044-3328. doi:10.1007/BF01339504.

[11] K.S. Babu et al. Working group report: Baryon number violation. In *Community Summer Study 2013: Snowmass on the Mississippi*, 11 2013.

[12] K. Abe et al. Hyper-kamiokande design report. 5 2018.

[13] K. Abe, Y. Haga, Y. Hayato, M. Ikeda, K. Iyogi, J. Kameda, Y. Kishimoto, M. Miura, S. Moriyama, M. Nakahata, T. Nakajima, Y. Nakano, S. Nakayama, A. Orii, H. Sekiya, M. Shiozawa, A. Takeda, H. Tanaka, T. Tomura, R. A. Wendell, R. Akutsu, T. Irvine, T. Kajita, K. Kaneyuki, Y. Nishimura, E. Richard, K. Okumura, L. Labarga, P. Fernandez, J. Gustafson, C. Kachulis, E. Kearns, J. L. Raaf, J. L. Stone, L. R. Sulak, S. Berkman, C. M. Nantais, H. A. Tanaka, S. Tobayama, M. Goldhaber, W. R. Kropp, S. Mine, P. Weatherly, M. B. Smy, H. W. Sobel, V. Takhistov, K. S. Ganezer, B. L. Hartfiel, J. Hill, N. Hong, J. Y. Kim, I. T. Lim, R. G. Park, A. Himmel, Z. Li, E. O'Sullivan, K. Scholberg, C. W. Walter, T. Wongjirad, T. Ishizuka, S. Tasaka, J. S. Jang, J. G. Learned, S. Matsuno, S. N. Smith, M. Friend, T. Hasegawa, T. Ishida, T. Ishii, T. Kobayashi, T. Nakadaira, K. Nakamura, Y. Oyama, K. Sakashita, T. Sekiguchi, T. Tsukamoto, A. T. Suzuki, Y. Takeuchi, T. Yano, S. V. Cao, T. Hiraki, S. Hirota, K. Huang, T. Kikawa, A. Minamino, T. Nakaya, K. Suzuki, Y. Fukuda, K. Choi, Y. Itow, T. Suzuki, P. Mijakowski, K. Frankiewicz, J. Hignight, J. Imber, C. K. Jung, X. Li, J. L. Palomino, M. J. Wilking, C. Yanagisawa, D. Fukuda, H. Ishino, T. Kayano, A. Kibayashi, Y. Koshio, T. Mori, M. Sakuda, C. Xu, Y. Kuno, R. Tacik, S. B. Kim, H. Okazawa, Y. Choi, K. Nishijima, M. Koshiba, Y. Totsuka, Y. Suda, M. Yokoyama, C. Bronner, M. Hartz, K. Martens, Ll. Marti, Y. Suzuki, M. R. Vagins, J. F. Martin, A. Konaka, S. Chen, Y. Zhang, and R. J. Wilkes. Search for proton decay via $pe^+\pi^0$ and $p\mu^+\pi^0$ in 0.31 megaton $\cdot$ years exposure of the super-kamiokande water cherenkov detector. *Phys. Rev. D*, 95:012004, Jan 2017. doi:10.1103/PhysRevD.95.012004. URL `https://link.aps.org/doi/10.1103/PhysRevD.95.012004`.

[14] Mark Trodden and Sean M. Carroll. Tasi lectures: Introduction to cosmology. In *Theoretical Advanced Study Institute in Elementary Particle Physics (TASI 2002): Particle Physics and Cosmology: The Quest for Physics Beyond the Standard Model(s)*, page 703793, 1 2004.

[15] M. Fukugita and T. Yanagida. Barygenesis without grand unification. *Physics Letters B*, 174(1):4547, 1986. ISSN 0370-2693. doi:10.1016/0370-2693(86)91126-3. URL http://www.sciencedirect.com/science/article/pii/0370269386911263.

[16] M. Fukugita and T. Yanagida. Resurrection of grand unified theory baryogenesis. *Phys. Rev. Lett.*, 89:131602, Sep 2002. doi:10.1103/PhysRevLett.89.131602. URL https://link.aps.org/doi/10.1103/PhysRevLett.89.131602.

[17] B. Pontecorvo. Neutrino experiments and the problem of conservation of leptonic charge. *Sov. Phys. JETP*, 26:984988, 1968.

[18] Ziro Maki, Masami Nakagawa, and Shoichi Sakata. Remarks on the unified model of elementary particles. *Progress of Theoretical Physics*, 28(5):870880, 11 1962. ISSN 0033-068X. doi:10.1143/PTP.28.870. URL https://doi.org/10.1143/PTP.28.870.

[19] K C Freeman. On the disks of spiral and s0 galaxies. *Astrophys. J. 160: 811-30(Jun 1970).*, 1 1970. doi:10.1086/150474.

[20] D. N. Spergel, L. Verde, H. V. Peiris, E. Komatsu, M. R. Nolta, C. L. Bennett, M. Halpern, G. Hinshaw, N. Jarosik, A. Kogut, M. Limon, S. S. Meyer, L. Page, G. S. Tucker, J. L. Weiland, E. Wollack, and E. L. Wright. First-year wilkinson microwave anisotropy probe (WMAP) observations: Determination of cosmological parameters. *The Astrophysical Journal Supplement Series*, 148(1):175194, sep 2003. doi:10.1086/377226. URL https://doi.org/10.1086%2F377226.

[21] M. Tanabashi et al. Review of particle physics. *Phys. Rev. D*, 98:030001, Aug 2018. doi:10.1103/PhysRevD.98.030001. URL https://link.aps.org/doi/10.1103/PhysRevD.98.030001.

[22] Ofer Lahav and Andrew R Liddle. The cosmological parameters, 2004.

[23] Peter Schneider. *Extragalactic Astronomy and Cosmology.* Springer-Verlag Berlin Heidelberg, second edition, 2015. ISBN 978-3-642-54082-0.

[24] J. H. Christenson, J. W. Cronin, V. L. Fitch, and R. Turlay. Evidence for the 2π Decay of the K_2^0 Meson. *Phys. Rev. Lett.*, 13:138140, 1964. doi:10.1103/PhysRevLett.13.138.

[25] R. Aaij et al. Observation of CP Violation in Charm Decays. *Phys. Rev. Lett.*, 122:211803, May 2019. doi:10.1103/PhysRevLett.122.211803. URL https://link.aps.org/doi/10.1103/PhysRevLett.122.211803.

[26] C. A. Baker, D. D. Doyle, P. Geltenbort, K. Green, M. G. D. van der Grinten, P. G. Harris, P. Iaydjiev, S. N. Ivanov, D. J. R. May, J. M. Pendlebury, J. D.

Richardson, D. Shiers, and K. F. Smith. Improved Experimental Limit on the Electric Dipole Moment of the Neutron. *Phys. Rev. Lett.*, 97:131801, Sep 2006. doi:10.1103/PhysRevLett.97.131801. URL https://link.aps.org/doi/10.1103/PhysRevLett.97.131801.

[27] Gerard 't Hooft. Symmetry breaking through bell-jackiw anomalies. *Phys. Rev. Lett.*, 37:811, 1976. doi:10.1103/PhysRevLett.37.8. [,226(1976)].

[28] G. 't Hooft. Computation of the quantum effects due to a four-dimensional pseudoparticle. *Phys. Rev. D*, 14:34323450, Dec 1976. doi:10.1103/PhysRevD.14.3432. URL https://link.aps.org/doi/10.1103/PhysRevD.14.3432.

[29] R.D. Peccei and Helen Quinn. *CP* Conservation in the Presence of Pseudoparticles. *Physical Review Letters*, 38:14401443, 06 1977. doi:10.1103/PhysRevLett.38.1440.

[30] F. Wilczek. Problem of strong p and t invariance in the presence of instantons. *Phys. Rev. Lett.*, 40:279282, Jan 1978. doi:10.1103/PhysRevLett.40.279. URL https://link.aps.org/doi/10.1103/PhysRevLett.40.279.

[31] Steven Weinberg. A new light boson? *Phys. Rev. Lett.*, 40:223226, Jan 1978. doi:10.1103/PhysRevLett.40.223. URL https://link.aps.org/doi/10.1103/PhysRevLett.40.223.

[32] Roberto D. Peccei. *The Strong CP Problem and Axions*, page 317. Number 741 in Lecture Notes in Physics. Springer Berlin Heidelberg, Berlin, Heidelberg, 2008. ISBN 978-3-540-73518-2. doi:10.1007/978-3-540-73518-2_1. URL https://doi.org/10.1007/978-3-540-73518-2_1.

[33] Joerg Jaeckel and Andreas Ringwald. The low-energy frontier of particle physics. *Annual Review of Nuclear and Particle Science*, 60(1):405437, 2010. doi:10.1146/annurev.nucl.012809.104433. URL https://doi.org/10.1146/annurev.nucl.012809.104433.

[34] J. Beacham, C. Burrage, D. Curtin, A. De Roeck, J. Evans, J. L. Feng, C. Gatto, S. Gninenko, A. Hartin, I. Irastorza, J. Jaeckel, K. Jungmann, K. Kirch, F. Kling, S. Knapen, M. Lamont, G. Lanfranchi, C. Lazzeroni, A. Lindner, F. Martinez-Vidal, M. Moulson, N. Neri, M. Papucci, I. Pedraza, K. Petridis, M. Pospelov, A. Rozanov, G. Ruoso, P. Schuster, Y. Semertzidis, T. Spadaro, C. Vallee, and G. Wilkinson. Physics beyond colliders at CERN: Beyond the standard model working group report. *arXiv:1901.09966*, 2019.

[35] Kyu Jung Bae, Ji-Haeng Huh, and Jihn E Kim. Updating the axion cold dark matter energy density. *Journal of Cosmology and Astroparticle Physics*, 2008(09): 005, sep 2008. doi:10.1088/1475-7516/2008/09/005. URL https://doi.org/10.1088%2F1475-7516%2F2008%2F09%2F005.

[36] Luca Visinelli. Axions in cold dark matter and inflation models, 2011.

[37] A. Halprin, C. M. Andersen, and H. Primakoff. Photonic decay rates and nuclear-coulomb-field coherent production processes. *Phys. Rev.*, 152:12951303, Dec 1966. doi:10.1103/PhysRev.152.1295. URL https://link.aps.org/doi/10.1103/PhysRev.152.1295.

[38] H. Schlattl, A. Weiss, and G. Raffelt. Helioseismological constraint on solar axion emission. *Astroparticle Physics*, 10(4):353359, 1999. ISSN 0927-6505. doi:10.1016/S0927-6505(98)00063-2. URL http://www.sciencedirect.com/science/article/pii/S0927650598000632.

[39] K. Zioutas, C.E. Aalseth, D. Abriola, III F.T.Avignone, R.L. Brodzinski, J.I. Collar, R. Creswick, D.E.Di Gregorio, H. Farach, A.O. Gattone, C.K. Guérard, F. Hasenbalg, M. Hasinoff, H. Huck, A. Liolios, H.S. Miley, A. Morales, J. Morales, D. Nikas, S. Nussinov, A. Ortiz, E. Savvidis, S. Scopel, P. Sievers, J.A. Villar, and L. Walckiers. A decommissioned LHC model magnet as an axion telescope. *Nuclear Instruments and Methods in Physics Research Section A: Accelerators, Spectrometers, Detectors and Associated Equipment*, 425(3):480487, 1999. ISSN 0168-9002. doi:10.1016/S0168-9002(98)01442-9. URL http://www.sciencedirect.com/science/article/pii/S0168900298014429.

[40] V. Anastassopoulos, S. Aune, K. Barth, A. Belov, H. Bräuninger, G. Cantatore, J. M. Carmona, J. F. Castel, S. A. Cetin, F. Christensen, J. I. Collar, T. Dafni, M. Davenport, T. A. Decker, A. Dermenev, K. Desch, C. Eleftheriadis, G. Fanourakis, E. Ferrer-Ribas, H. Fischer, J. A. García, A. Gardikiotis, J. G. Garza, E. N. Gazis, T. Geralis, I. Giomataris, S. Gninenko, C. J. Hailey, M. D. Hasinoff, D. H. H. Hoffmann, F. J. Iguaz, I. G. Irastorza, A. Jakobsen, J. Jacoby, K. Jakovi, J. Kaminski, M. Karuza, N. Kralj, M. Krmar, S. Kostoglou, Ch. Krieger, B. Laki, J. M. Laurent, A. Liolios, A. Ljubii, G. Luzón, M. Maroudas, L. Miceli, S. Neff, I. Ortega, T. Papaevangelou, K. Paraschou, M. J. Pivovaroff, G. Raffelt, M. Rosu, J. Ruz, E. Ruiz Chóliz, I. Savvidis, S. Schmidt, Y. K. Semertzidis, S. K. Solanki, L. Stewart, T. Vafeiadis, J. K. Vogel, S. C. Yildiz, K. Zioutas, and CAST Collaboration. New CAST limit on the axionphoton interaction. *Nature Physics*, 13(6):584590, 2017. ISSN 1745-2481. doi:10.1038/nphys4109.

[41] E Armengaud et al. Conceptual design of the international axion observatory (IAXO). *Journal of Instrumentation*, 9(05):T05002T05002, may 2014. doi:10.1088/1748-0221/9/05/t05002. URL https://doi.org/10.1088%2F1748-0221%2F9%2F05%2Ft05002.

[42] Babette Döbrich, Joerg Jaeckel, Felix Kahlhoefer, Andreas Ringwald, and Kai Schmidt-Hoberg. ALPtraum: ALP production in proton beam dump experi-

ments. *Journal of High Energy Physics*, 2016(2):18, 2016. ISSN 1029-8479. doi:10.1007/JHEP02(2016)018.

[43] John N. Bahcall and Raymond Davis. Solar neutrinos: A scientific puzzle. *Science*, 191(4224):264267, 1976. ISSN 0036-8075. doi:10.1126/science.191.4224.264. URL `https://science.sciencemag.org/content/191/4224/264`.

[44] Kai Zuber. *Neutrino Physics*. CRC Press, Taylor and Francis Group, 2 edition, 2012.

[45] Tsutomu Yanagida. Horizontal symmetry and masses of neutrinos. *Progress of Theoretical Physics*, 64(3):11031105, 09 1980. ISSN 0033-068X. doi:10.1143/PTP.64.1103. URL `https://doi.org/10.1143/PTP.64.1103`.

[46] Peter Minkowski. $\mu \to e\gamma$ at a rate of one out of 10^9 muon decays? *Phys. Lett.*, B67:421428, 1977. doi:10.1016/0370-2693(77)90435-X.

[47] Rabindra N. Mohapatra and Goran Senjanovic. Neutrino mass and spontaneous parity violation. *Phys. Rev. Lett.*, 44:912, 1980. doi:10.1103/PhysRevLett.44.912.

[48] Pierre Ramond. The family group in grand unified theories. In *International Symposium on Fundamentals of Quantum Theory and Quantum Field Theory Palm Coast, Florida, February 25-March 2, 1979*, page 265280, 1979.

[49] J. Orloff, S. Lavignac, and M. Cribier, editors. *Seesaw mechanism. Proceedings, International Conference, SEESAW25, Paris, France, June 10-11, 2004*, 2005.

[50] Sergey Alekhin et al. A facility to search for hidden particles at the CERN SPS: the SHiP physics case. *Reports on Progress in Physics*, 79(12):124201, Dec 2016. doi:10.1088/0034-4885/79/12/124201.

[51] Takehiko Asaka, Steve Blanchet, and Mikhail Shaposhnikov. The νMSM, dark matter and neutrino masses. *Physics Letters B*, 631(4):151156, 2005. ISSN 0370-2693. doi:10.1016/j.physletb.2005.09.070. URL `http://www.sciencedirect.com/science/article/pii/S0370269305013675`.

[52] Takehiko Asaka and Mikhail Shaposhnikov. The νMSM, dark matter and baryon asymmetry of the universe. *Physics Letters B*, 620(1):1726, 2005. ISSN 0370-2693. doi:10.1016/j.physletb.2005.06.020. URL `http://www.sciencedirect.com/science/article/pii/S0370269305008087`.

[53] D. Banerjee et al. Search for a hypothetical 16.7 mev gauge boson and dark photons in the na64 experiment at cern. *Phys. Rev. Lett.*, 120:231802, Jun 2018. doi:10.1103/PhysRevLett.120.231802. URL `https://link.aps.org/doi/10.1103/PhysRevLett.120.231802`.

[54] L.B. Okun. Limits of electrodynamics: Paraphotons? *Sov. Phys. JETP*, 56:502, 1982.

[55] SHiP Collaboration. A facility to search for hidden particles (SHiP) at the CERN SPS. *arXiv e-prints*, art. arXiv:1504.04956, Apr 2015.

[56] C Ahdida et al. SHiP Experiment - Progress Report. Technical Report CERN-SPSC-2019-010. SPSC-SR-248, CERN, Geneva, Jan 2019. URL `https://cds.cern.ch/record/2654870`.

[57] C Ahdida et al. SHiP experiment - comprehensive design study report. Technical Report CERN-SPSC-2019-049. SPSC-SR-263, CERN, Geneva, Dec 2019. URL `https://cds.cern.ch/record/2704147`.

[58] G. Bernardi, G. Carugno, J. Chauveau, F. Dicarlo, M. Dris, J. Dumarchez, M. Ferro-Luzzi, J.-M. Levy, D. Lukas, J.-M. Perreau, Y. Pons, A.-M. Touchard, and F. Vannucci. Search for neutrino decay. *Physics Letters B*, 166(4):479483, 1986. ISSN 0370-2693. doi:10.1016/0370-2693(86)91602-3. URL `http://www.sciencedirect.com/science/article/pii/0370269386916023`.

[59] G. Bernardi et al. Further limits on heavy neutrino couplings. *Phys. Lett.*, B203: 332334, 1988. doi:10.1016/0370-2693(88)90563-1.

[60] F Vannucci. Sterile neutrinos: From cosmology to the lhc. *Journal of Physics: Conference Series*, 136(2):022030, 2008. URL `http://stacks.iop.org/1742-6596/136/i=2/a=022030`.

[61] J. Dorenbosch, J.V. Allaby, U. Amaldi, G. Barbiellini, C. Berger, F. Bergsma, A. Capone, W. Flegel, L. Lanceri, M. Metcalf, C. Nieuwenhuis, J. Panman, K. Winter, I. Abt, J. Aspiazu, F.W. Büsser, H. Daumann, P.D. Gall, T. Hebbeker, F. Niebergall, P. Schütt, P. Stähelin, P. Gorbunov, E. Grigoriev, V. Kaftanov, V. Khovansky, A. Rosanov, A. Baroncelli, L. Barone, B. Borgia, C. Bosio, M. Diemoz, U. Dore, F. Ferroni, E. Longo, L. Luminari, P. Monacelli, F. De Notaristefani, P. Pistilli, R. Santacesaria, C. Santoni, L. Tortora, and V. Valente. A search for decays of heavy neutrinos in the mass range 0.52.8 GeV. *Physics Letters B*, 166(4):473478, 1986. ISSN 0370-2693. doi:10.1016/0370-2693(86)91601-1. URL `http://www.sciencedirect.com/science/article/pii/0370269386916011`.

[62] A. Vaitaitis et al. Search for neutral heavy leptons in a high-energy neutrino beam. *Phys. Rev. Lett.*, 83:49434946, 1999. doi:10.1103/PhysRevLett.83.4943.

[63] C.H. Albright and C. Jarlskog. Neutrino production of m+ and e+ heavy leptons (i). *Nuclear Physics B*, 84(2):467492, 1975. ISSN 0550-3213. doi:10.1016/0550-3213(75)90318-1. URL `http://www.sciencedirect.com/science/article/pii/0550321375903181`.

[64] E. Lopez Sola, M. Calviani, P. Avigni, M. Battistin, J. Busom Descarrega, J. Canhoto Espadanal, M. A. Fraser, S. Gilardoni, B. Goddard, D. Grenier, R. Jacobsson, K. Kershaw, M. Lamont, A. Perillo-Marcone, M. Pandey, B. Riffaud, S. Sgobba, V. Vlachoudis, and L. Zuccalli. Design of a high power production target for the beam dump facility at cern. *Phys. Rev. Accel. Beams*, 22:113001, Nov 2019. doi:10.1103/PhysRevAccelBeams.22.113001. URL `https://link.aps.org/doi/10.1103/PhysRevAccelBeams.22.113001`.

[65] Alfredo Ferrari, Paola R. Sala, Alberto Fasso, and Johannes Ranft. FLUKA: A multi-particle transport code (program version 2005). 2005. doi:10.2172/877507.

[66] T.T. Böhlen, F. Cerutti, M.P.W. Chin, A. Fassò, A. Ferrari, P.G. Ortega, A. Mairani, P.R. Sala, G. Smirnov, and V. Vlachoudis. The FLUKA Code: Developments and Challenges for High Energy and Medical Applications. *Nuclear Data Sheets*, 120:211214, 2014. ISSN 0090-3752. doi:10.1016/j.nds.2014.07.049. URL `http://www.sciencedirect.com/science/article/pii/S0090375214005018`.

[67] A. Akmete et al. The active muon shield in the SHiP experiment. *Journal of Instrumentation*, 12(05):P05011P05011, may 2017. doi:10.1088/1748-0221/12/05/p05011. URL `https://doi.org/10.1088%2F1748-0221%2F12%2F05%2Fp05011`.

[68] Torbjörn Sjöstrand, Stephen Mrenna, and Peter Skands. A brief introduction to pythia 8.1. *Computer Physics Communications*, 178(11):852867, 2008. ISSN 0010-4655. doi:10.1016/j.cpc.2008.01.036. URL `http://www.sciencedirect.com/science/article/pii/S0010465508000441`.

[69] Torbjörn Sjöstrand, Stephen Mrenna, and Peter Skands. PYTHIA 6.4 physics and manual. *Journal of High Energy Physics*, 2006(05):026026, may 2006. doi:10.1088/1126-6708/2006/05/026. URL `https://doi.org/10.1088%2F1126-6708%2F2006%2F05%2F026`.

[70] OPERA Collaboration, N. Agafonova, et al. Final results of the opera experiment on appearance in the cngs neutrino beam. *Phys. Rev. Lett.*, 120:211801, May 2018. doi:10.1103/PhysRevLett.120.211801. URL `https://link.aps.org/doi/10.1103/PhysRevLett.120.211801`.

[71] OPERA Collaboration, N. Agafonova, et al. Procedure for short-lived particle detection in the opera experiment and its application to charm decays. *The European Physical Journal C*, 74, 04 2014. doi:10.1140/epjc/s10052-014-2986-0.

[72] G. Bencivenni, R. De Oliveira, G. Morello, and M. Poli Lener. The micro-resistive well detector: a compact spark-protected single amplification-stage mpgd. *Journal of Instrumentation*, 10(02):P02008P02008, Feb 2015. ISSN

1748-0221. doi:10.1088/1748-0221/10/02/p02008. URL http://dx.doi.org/10.1088/1748-0221/10/02/P02008.

[73] Piet Wertelaers and Alexandre Perez. Expanding piano frame for straw tracker. Dec 2019. URL https://cds.cern.ch/record/2703481.

[74] Daniel Bick, Stefan Bieschke, Caren Hagner, Benedict Kaiser, and Walter Schmidt-Parzefall. The suspended bridge design concept for the SHiP spectrometer straw tracker. Dec 2019. URL https://cds.cern.ch/record/2702653.

[75] P. Gianotti, V. Lucherini, E. Pace, G. Boca, Susanna Costanza, P. Genova, Lia Lavezzi, P. Montanga, Alberto Rotondi, M. Bragadireanu, M. Vasile, D. Pietreanu, Jacek Biernat, Sedigheh Jowzaee, Grzegorz Korcyl, M. Palka, Piotr Salabura, J. Smyrski, Tomasz Fiutowski, and S. Spataro. The straw tube trackers of the panda experiment. 07 2013. doi:10.1109/ANIMMA.2013.6728039.

[76] Walter M. Bonivento. Studies for the electro-magnetic calorimeter SplitCal for the SHiP experiment at CERN with shower direction reconstruction capability. *Journal of Instrumentation*, 13(02):C02041C02041, feb 2018. doi:10.1088/1748-0221/13/02/c02041. URL https://doi.org/10.1088%2F1748-0221%2F13%2F02%2Fc02041.

[77] T. Alexopoulos et al. Development of large size micromegas detector for the upgrade of the atlas muon system. *Nucl. Instrum. Meth. A*, 617:161165, 2010. doi:10.1016/j.nima.2009.06.113.

[78] Kyrylo Bondarenko, Alexey Boyarsky, Dmitry Gorbunov, and Oleg Ruchayskiy. Phenomenology of gev-scale heavy neutral leptons. *Journal of High Energy Physics*, 2018(11), Nov 2018. ISSN 1029-8479. doi:10.1007/jhep11(2018)032. URL http://dx.doi.org/10.1007/JHEP11(2018)032.

[79] H. Bethe. Zur theorie des durchgangs schneller korpuskularstrahlen durch materie. *Annalen der Physik*, 397(3):325400, 1930. ISSN 1521-3889. doi:10.1002/andp.19303970303. URL http://dx.doi.org/10.1002/andp.19303970303.

[80] H. Bethe. Bremsformel für elektronen relativistischer geschwindigkeit. *Zeitschrift für Physik*, 76(5-6):293299, 1932. ISSN 0044-3328. doi:10.1007/BF01342532. URL http://dx.doi.org/10.1007/BF01342532.

[81] F. Sauli. Principles of operation of multiwire proportional and drift chambers. *Lectures given in the academic training programme of CERN*, 1977.

[82] Hermann Kolanoski. Detektoren in der elementarteilchenphysik, 2007.

[83] Torben Ferber. Messung der gaseigenschaften unter einfluss von molekularem sauerstoff und aufbau eines gassystems für das driftröhren-myon-spektrometer des operadetektors. Diplomarbeit, Universität Hamburg, July 2006.

[84] W. Diethorn. *A METHANE PROPORTIONAL COUNTER SYSTEM FOR NATURAL RADIOCARBON MEASUREMENTS (thesis)*. Mar 1956.

[85] C. Ahdida et al. Measurement of the muon flux for the SHiP experiment. *CERN-SHiP-NOTE-2019-003*, Dec 2019. URL `https://cds.cern.ch/record/2703227`.

[86] S. Agostinelli et al. Geant4 a simulation toolkit. *Nuclear Instruments and Methods in Physics Research Section A: Accelerators, Spectrometers, Detectors and Associated Equipment*, 506(3):250303, 2003. ISSN 0168-9002. doi:10.1016/S0168-9002(03)01368-8. URL `http://www.sciencedirect.com/science/article/pii/S0168900203013688`.

[87] J. Allison et al. Recent developments in Geant4. *Nuclear Instruments and Methods in Physics Research Section A: Accelerators, Spectrometers, Detectors and Associated Equipment*, 835:186225, 2016. ISSN 0168-9002. doi:10.1016/j.nima.2016.06.125. URL `http://www.sciencedirect.com/science/article/pii/S0168900216306957`.

[88] Claudia Christina Ahdida, Mirkoantonio Casolino, Hans Dijkstra, Robert Froeschl, Eric Van Herwijnen, and Thomas Ruf. Fluka-geant4 comparison for the muon flux experiment in the h4 beamline. Dec 2019. URL `https://cds.cern.ch/record/2705389`.

[89] SHiP Collaboration. Measurement of the muon flux for the SHiP experiment. *arXiv 2001.04784*, 2020.

[90] Hans Dijkstra. Normalisation of proton flux during muon flux beam test. *CERN-SHiP-INT-2019-001*, Apr 2019. URL `https://cds.cern.ch/record/2672141`.

[91] Goliath magnet. *http://te-dep-epc-hpc-section.web.cern.ch/te-dep-epc-hpc-section/spectrometers/Goliath/general.stm*, March 2020.

[92] Marcel Rosenthal, Nikolaos Charitonidis, Panagiota Chatzidaki, Rachel Margraf, Henric Wilkens, Felix Bergsma, and Pierre-Ange Giudici. Magnetic field measurements of the GOLIATH Magnet in EHN1. *CERN-ACC-NOTE-2018-0028*, Mar 2018. URL `http://cds.cern.ch/record/2310483`.

[93] C. Höppner, S. Neubert, B. Ketzer, and S. Paul. A novel generic framework for track fitting in complex detector systems. *Nuclear Instruments and Methods in Physics*

Research Section A: Accelerators, Spectrometers, Detectors and Associated Equipment, 620(2):518525, 2010. ISSN 0168-9002. doi:10.1016/j.nima.2010.03.136. URL http://www.sciencedirect.com/science/article/pii/S0168900210007473.

[94] R. Zimmermann, J. Ebert, C. Hagner, B. Koppitz, V. Saveliev, W. Schmidt-Parzefall, J. Sewing, and Y. Zaitsev. The precision tracker of the OPERA detector. *Nuclear Instruments and Methods in Physics Research Section A: Accelerators, Spectrometers, Detectors and Associated Equipment*, 555(1):435450, 2005. ISSN 0168-9002. doi:10.1016/j.nima.2005.09.003. URL http://www.sciencedirect.com/science/article/pii/S0168900205018061.

[95] SHiP Collaboration. Heavy flavour cascade production in a beam dump. *CERN-SHiP-NOTE-2015-009*, Dec 2015. URL http://cds.cern.ch/record/2115534.

[96] C. Lourenço and H.K. Wöhri. Heavy-flavour hadro-production from fixed-target to collider energies. *Physics Reports*, 433(3):127180, 2006. ISSN 0370-1573. doi:10.1016/j.physrep.2006.05.005. URL http://www.sciencedirect.com/science/article/pii/S0370157306001815.

[97] A Akmete et al. Measurement of associated charm production induced by 400 GeV/c protons. Technical Report CERN-SPSC-2017-033. SPSC-EOI-017, CERN, Geneva, Oct 2017. URL https://cds.cern.ch/record/2286844.

[98] R. Acquafredda et al. The OPERA experiment in the CERN to Gran Sasso neutrino beam. *JINST*, 4:P04018, 2009. doi:10.1088/1748-0221/4/04/P04018.

[99] Daniel Bick, Antonio Crupano, Onur Durhan, Oliver Lantwin, Alessandra Pastore, Eric van Herwijnen, and Thomas Ruf. Alignment of the muon-flux spectrometer in FairShip using the survey measurements. *CERN-SHiP-NOTE-2019-001*, Feb 2019. URL https://cds.cern.ch/record/2658044.

[100] Texas Instruments Incorporated. *LVDS Application and Data Handbook*. Post Office Box 655303, Dallas, Texas 75265, November 2002. URL https://www.ti.com/lit/ug/slld009/slld009.pdf.

[101] M. M. White. Recent results from l3. In *New and exotic phenomena '90. Proceedings, 25th Rencontres de Moriond, 10th Moriond Workshop, Les Arcs, France, January 20-27, 1990*, page 8193, 1990. URL https://inspirehep.net/record/309783/files/C90-01-20_81-93.pdf.

[102] J. Schütt and R. van Staa. *OSUB OPERA Support Board manual*. Universität Hamburg, February 2006.

[103] CAEN S.p.A. CAEN v1190A description webpage. *https://www.caen.it/products/v1190a-2esst/*, March 2020.

[104] CAEN S.p.A. CAEN v2718 product webpage. *https://www.caen.it/products/v2718/*, March 2020.

[105] CAEN S.p.A. CAEN VMElib description webpage. *https://www.caen.it/products/caenvmelib-library/*, March 2020.

[106] Benoit Cumer. H4 test measurement of the muon flux setup on h4 beam line measurement of july 04th-06th, 2018. *CERN-EDMS-2001697v1*, July 2018.

[107] J. Schütt and R. van Staa. *OTB OPERA Trigger Board manual*. Universität Hamburg, March 2006.

[108] Ruten Gurin and Andrei Maslennikov. *ControlHost - Distributed Data Handling Package*, 1995.

[109] Volker Blobel. Millepede II Software. `http://www.desy.de/~kleinwrt/MP2/doc/html/index.html`.

[110] Volker Blobel. Millepede II Draft Manual. `http://www.desy.de/~kleinwrt/MP2/doc/html/draftman_page.html`, 2007.

[111] Claus Kleinwort. General broken lines as advanced track fitting method. *Nuclear Instruments and Methods in Physics Research Section A: Accelerators, Spectrometers, Detectors and Associated Equipment*, 673:107110, 2012. ISSN 0168-9002. doi:10.1016/j.nima.2012.01.024. URL `http://www.sciencedirect.com/science/article/pii/S0168900212000642`.

[112] Rene Brun and Fons Rademakers. ROOT an object oriented data analysis framework. *Nuclear Instruments and Methods in Physics Research Section A: Accelerators, Spectrometers, Detectors and Associated Equipment*, 389(1):8186, 1997. ISSN 0168-9002. doi:10.1016/S0168-9002(97)00048-X. URL `http://www.sciencedirect.com/science/article/pii/S016890029700048X`. New Computing Techniques in Physics Research V.

[113] Makoto Matsumoto and Takuji Nishimura. Mersenne twister: A 623-dimensionally equidistributed uniform pseudo-random number generator. *ACM Trans. Model. Comput. Simul.*, 8(1):330, January 1998. ISSN 1049-3301. doi:10.1145/272991.272995. URL `http://doi.acm.org/10.1145/272991.272995`.

[114] Pierre L'Ecuyer and Richard Simard. TestU01: A C Library for Empirical Testing of Random Number Generators. *ACM Trans. Math. Softw.*, 33(4):22:122:40, August 2007. ISSN 0098-3500. doi:10.1145/1268776.1268777. URL `http://doi.acm.org/10.1145/1268776.1268777`.

[115] Particle Data Group. Muons in iron. *http://pdg.lbl.gov/2019/AtomicNuclearProperties/MUE/muE_iron_Fe.pdf*, 2019.

A Trigger

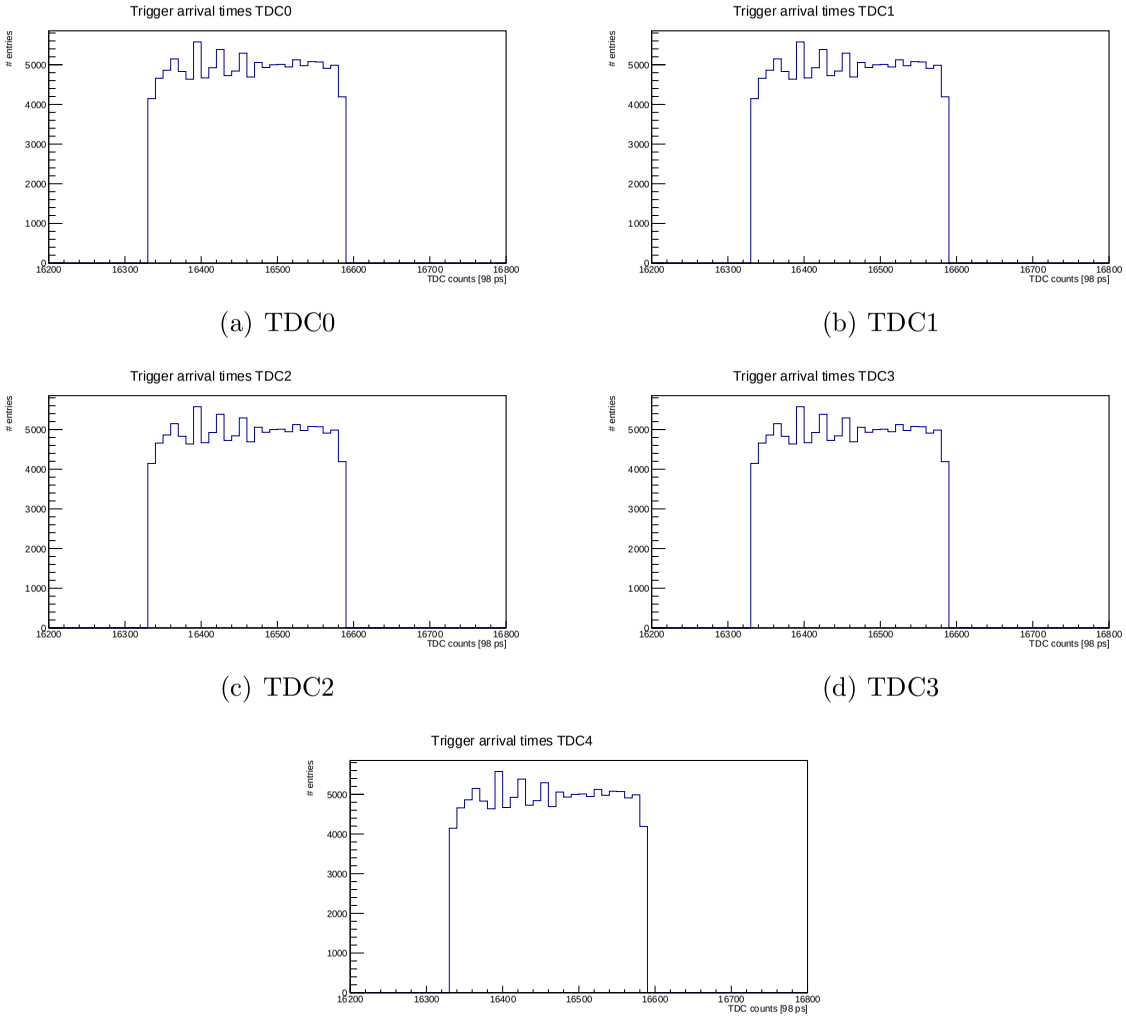

(a) TDC0

(b) TDC1

(c) TDC2

(d) TDC3

(e) TDC4

Figure A.1: Times, at which the trigger signal is recorded on each TDC board for one example spill. These are distributed in a $\sim 25\,\text{ns}$ wide window, showing the jitter introduced by the 40 MHz clocks of the TDC boards. This jitter can be removed by using the high precision measurement of the trigger signal arrival time and subtracting it from each drift time measurement for a particular TDC board.

B Alignment Results

B.1 Drift Tube Module Naming Convention

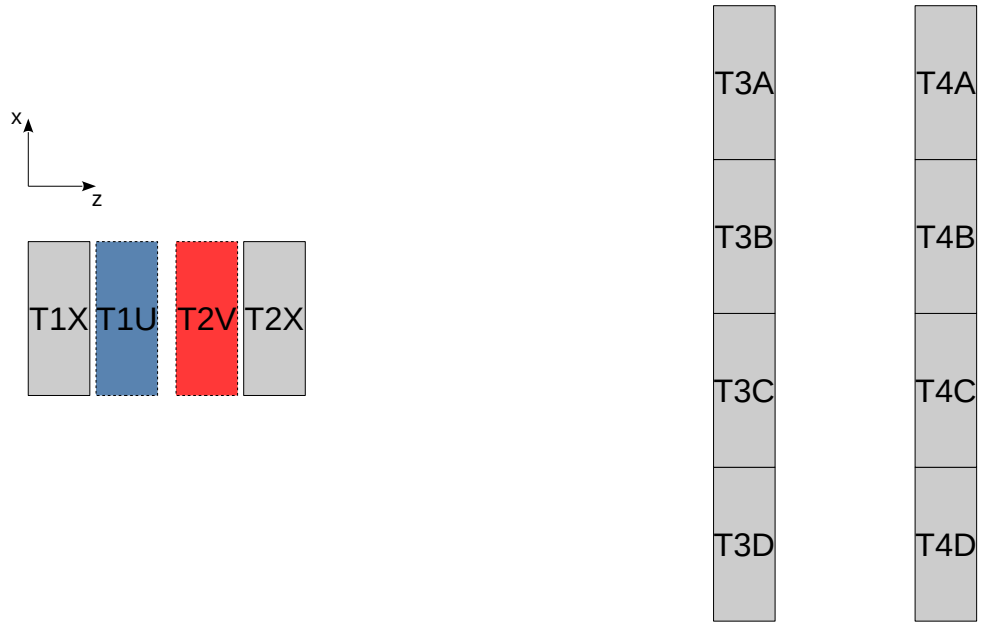

Figure B.1: Naming of the drift tube modules used throughout this thesis. Note that the sketch is not to scale. The blue and red filled drift tube modules are the modules oriented with a stereo angle of $\pm 60°$ w.r.t the x-axis for three dimensional track resolution. The Goliath magnet is between the drift tube modules T2X and the four modules of station T3.

B.2 Label Decoding

Table B.1: Labels used for pede alignment decoded to drift tube module and global parameter for drift tube stations T1 and T2. All translations and rotations are with respect to the *local* alignment reference frame of a particular drift tube module. Hence the y axis is always parallel to the wires for each module.

Label	description
1001	translation of module T1X in x direction
1002	translation of module T1X in y direction
1003	translation of module T1X in z direction
1004	rotation of module T1X around x axis
1005	rotation of module T1X around y axis
1006	rotation of module T1X around z axis
1101	translation of module T1U in x direction
1102	translation of module T1U in y direction
1103	translation of module T1U in z direction
1104	rotation of module T1U around x axis
1105	rotation of module T1U around y axis
1106	rotation of module T1U around z axis
2001	translation of module T2V in x direction
2002	translation of module T2V in y direction
2003	translation of module T2V in z direction
2004	rotation of module T2V around x axis
2005	rotation of module T2V around y axis
2006	rotation of module T2V around z axis
2101	translation of module T2X in x direction
2102	translation of module T2X in y direction
2103	translation of module T2X in z direction
2104	rotation of module T2X around x axis
2105	rotation of module T2X around y axis
2106	rotation of module T2X around z axis

Table B.2: Labels used for pede alignment decoded to drift tube module and global parameter for drift tube station T3. All translations and rotations are with respect to the *local* alignment reference frame of a particular drift tube module. Hence the y axis is always parallel to the wires for each module.

Label	description
3001	translation of module T3A in x direction
3002	translation of module T3A in y direction
3003	translation of module T3A in z direction
3004	rotation of module T3A around x axis
3005	rotation of module T3A around y axis
3006	rotation of module T3A around z axis
3011	translation of module T3D in x direction
3012	translation of module T3D in y direction
3013	translation of module T3D in z direction
3014	rotation of module T3D around x axis
3015	rotation of module T3D around y axis
3016	rotation of module T3D around z axis
3021	translation of module T3C in x direction
3022	translation of module T3C in y direction
3023	translation of module T3C in z direction
3024	rotation of module T3C around x axis
3025	rotation of module T3C around y axis
3026	rotation of module T3C around z axis
3031	translation of module T3B in x direction
3032	translation of module T3B in y direction
3033	translation of module T3B in z direction
3034	rotation of module T3B around x axis
3035	rotation of module T3B around y axis
3036	rotation of module T3B around z axis

Table B.3: Labels used for pede alignment decoded to drift tube module and global parameter for drift tube station T4. All translations and rotations are with respect to the *local* alignment reference frame of a particular drift tube module. Hence the y axis is always parallel to the wires for each module.

Label	description
4001	translation of module T4A in x direction
4002	translation of module T4A in y direction
4003	translation of module T4A in z direction
4004	rotation of module T4A around x axis
4005	rotation of module T4A around y axis
4006	rotation of module T4A around z axis
4011	translation of module T4D in x direction
4012	translation of module T4D in y direction
4013	translation of module T4D in z direction
4014	rotation of module T4D around x axis
4015	rotation of module T4D around y axis
4016	rotation of module T4D around z axis
4021	translation of module T4C in x direction
4022	translation of module T4C in y direction
4023	translation of module T4C in z direction
4024	rotation of module T4C around x axis
4025	rotation of module T4C around y axis
4026	rotation of module T4C around z axis
4031	translation of module T4B in x direction
4032	translation of module T4B in y direction
4033	translation of module T4B in z direction
4034	rotation of module T4B around x axis
4035	rotation of module T4B around y axis
4036	rotation of module T4B around z axis